ADVANCED CONCEPTS IN NONLINEAR PIEZOELECTRIC ENERGY HARVESTING: INTENTIONALLY DESIGNED, INHERENTLY PRESENT, AND CIRCUIT NONLINEARITIES

A Dissertation
Presented to
The Academic Faculty

by

Stephen Leadenham

In Partial Fulfillment
of the Requirements for the Degree
Doctor of Philosophy in the
George W. Woodruff School of Mechanical Engineering

Georgia Institute of Technology
December 2015

Copyright © 2015 by Stephen Leadenham

ADVANCED CONCEPTS IN NONLINEAR PIEZOELECTRIC ENERGY HARVESTING: INTENTIONALLY DESIGNED, INHERENTLY PRESENT, AND CIRCUIT NONLINEARITIES

Approved by:

Dr. Alper Erturk, Advisor
Mechanical Engineering
Georgia Institute of Technology

Dr. Aldo Ferri
Mechanical Engineering
Georgia Institute of Technology

Dr. Laurence Jacobs
Civil Engineering
Mechanical Engineering
Georgia Institute of Technology

Dr. Massimo Ruzzene
Aerospace Engineering
Mechanical Engineering
Georgia Institute of Technology

Dr. Yang Wang
Civil Engineering
Georgia Institute of Technology

Date Approved: August 12, 2015

ACKNOWLEDGEMENTS

My utmost gratitude belongs to my advisor, Dr. Alper Erturk, for his tireless support during my time at Georgia Tech. Additional thanks belong to my committee members, Drs. Aldo Ferri, Laurence Jacobs, Massimo Ruzzene, and Yang Wang, for guidance on my studies and research. Financial support was provided in part by the National Science Foundation under Grant CMMI-1254262.

Contents

List of Tables

List of Figures

SUMMARY

This work is centered on the modeling, experimental identification, and dynamic interaction of inherently present and intentionally designed nonlinearities of piezoelectric structures focusing on applications to vibration energy harvesting. The following topics are explored in this theoretical and experimental research: (1) frequency bandwidth enhancement using a simple, intentionally designed, geometrically nonlinear M-shaped oscillator for low-intensity base accelerations; (2) multi-term harmonic balance analysis of this structure for primary and secondary resonance behaviors when coupled with piezoelectrics and an electrical load; (3) inherent electroelastic material softening and dissipative nonlinearities for various piezoelectric materials with a dynamical systems approach; and (4) development of a complete approximate analytical multiphysics electroelastic modeling framework accounting for material, dissipative, and strong circuit nonlinearities. The ramifications of this research go well beyond energy harvesting, since inherent nonlinearities of piezoelectric materials are pronounced in various applications ranging from sensing and actuation to their combined use for vibration control, while intentional bandwidth enhancement impacts not only on energy harvesting but also vibration damping. Over the past two decades, similar manifestations of softening nonlinearity in piezoelectric materials have been attributed to different phenomena, such as purely elastic nonlinear terms and coupling nonlinearity, by different research groups. In order to develop a unified nonlinear non-conservative framework with two-way coupling, the nonlinear dynamic behavior of bimorph piezoelectric cantilevers under low-to-moderate mechanical and electrical excitation levels are explored in energy harvesting, sensing, and actuation, well below the coercive field. The resulting nonlinear non-conservative distributed-parameter electroelastic modeling framework is analyzed extensively using the method of harmonic balance for model validation and nonlinear parameter identification. This multi-term harmonic balance framework is then combined with other nonlinear effects such as strong circuit nonlinearities due to AC-DC conversion,

and it can readily be extended to combining various nonlinear effects in other scenarios.

This dissertation is organized as follows: Chapter 1 provides an introduction into vibration-based piezoelectric energy harvesting and the nonlinear effects that are both inherently present and those that are intentionally designed for performance enhancement as well as essential circuit nonlinearities. Chapter 2 describes a platform for low-intensity broadband vibration energy harvesting designed to exhibit a pronounced geometric nonlinearity to increase the response bandwidth. Chapter 3 details the design, analysis, and experimental validation of a piezoelectric vibration energy harvester based on platform explained in the previous chapter. Chapter 4 deals with the derivation and validation of a unified modeling framework of the nonlinear constitutive behavior of soft piezoceramics commonly used for piezoelectric energy harvesters and sensors/actuators. In Chapter 5, this modeling framework is used to extract and identify nonlinear material parameters of soft piezoceramics, PZT-5A and PZT-5H. In Chapter 6, the given dynamical systems framework is extended to also handle the strong circuit nonlinearities caused by AC–DC rectification for practical energy harvesting applications and validated experimentally. Chapter 7 concludes this dissertation by summarizing the contributions made to the field of nonlinear piezoelectric structures with a focus on vibration energy harvesting and opportunities for further work. A derivation of a generalized Newton's method enabled harmonic balance solver and a MATLAB implementation used extensively in this research are included in Appendices A and B.

Chapter I

INTRODUCTION

1.1 Vibration Energy Harvesting Using Piezoelectric Transduction

Research on energy harvesting methods and technologies has received growing attention over the last decade to enable energy-autonomous systems [83, 34, 30]. The motivation for vibration-based energy harvesting is to power small electronic devices (such as wireless sensor networks used in passive and active monitoring applications) by using the vibrational energy available in their environments. Researchers have reported their work on modeling and applications of vibration-based energy harvesting using electromagnetic [37, 9, 29, 69], electrostatic [82, 66, 52], piezoelectric [81, 32, 25, 27, 3], and magnetostrictive [105, 4] transduction mechanisms, as well as electronic and ionic electroactive polymers [48, 11], polymer electrets[7], and even flexoelectricity for energy harvesting at submicron scales [26]. In particular, due to the high power density and ease of application of piezoelectric materials, piezoelectric energy harvesting has received the most attention [34, 88, 8, 77, 18].

The most commonly used piezoelectric energy harvester configuration is a cantilever with piezoceramic layers located on a vibrating host structure for electrical power generation from bending vibrations under resonance excitation. Such a design that operates effectively only at its linear resonance frequency is called a resonant energy harvester. Theoretical and experimental aspects of the linear cantilever design have been investigated extensively in the literature [81, 32, 80, 28, 27, 3].

Nonlinear effects in piezoelectric energy harvesting have been gaining dramatically increased attention. Due to distortion of the resonant peak by nonlinear effects, the frequency response bandwidth of a nonlinear energy harvester may be larger than that of a similar linear design. This has led to a number of efforts to create energy harvester configurations with intentionally designed nonlinearities. Additionally, the piezoelectric materials themselves display appreciable inherent nonlinear constitutive and dissipative behavior. Thirdly,

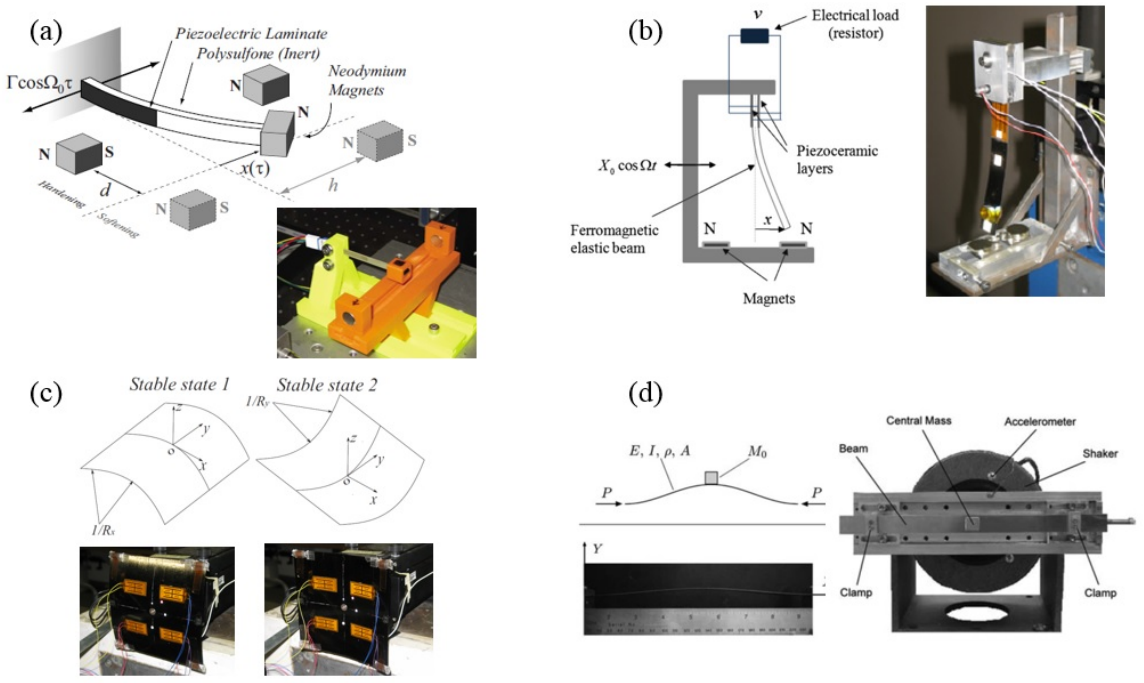

Figure 1: Example methods for generating nonlinear behavior in energy harvesting platforms. Monostable hardening/softening behavior caused by magnetic interaction (a) [92]. Bistablility due to magnetic attraction of external magenets to the ferromagnetic cantilever substrate (b) [31]. Bistability exhibited by a buckled asymmetric plate (c) [10]. Bistability due to buckling of an axially preloaded beam with clamped ends (d) [87].

to convert the alternating current produced to a vibrating piezoelectric energy harvesters to a form useful for powering electronic devices or charging electrical storage units, rectifiers and regulators must be used to produce a stable direct current output. These devices are inherently nonlinear in nature, employing elements such as diodes and switches. The effects of intentionally designed nonlinearities, inherently present piezoelectric constitutive, and strong harvesting circuit nonlinearities and their combination form the basis of this work.

1.2 Intentionally Designed Nonlinearities

A major limitation of the commonly employed linear/resonant energy harvester configuration is that the effective power generation performance of the device is limited to resonance excitation. If the excitation frequency deviates slightly from the fundamental resonance frequency of the energy harvester (due to changing excitation or environmental conditions or manufacturing imperfections of the harvester device), the electrical power output is reduced

by orders of magnitude especially in high-quality-factor devices intended for such resonant operation. In order to overcome the bandwidth issue of the conventional cantilever configuration, researchers [24] have recently considered exploiting nonlinear dynamic phenomena [71, 41]. Implementations of the hardening stiffness of the monostable Duffing oscillator for increasing the frequency bandwidth were discussed by Burrow et al. [16] and Mann and Sims [61] for electromagnetic energy harvesting. Ramlan et al. [79] discussed similar behavior along with snap-through motion in a bistable mass-spring-damper mechanism. Random excitation of monostable Duffing oscillators was theoretically investigated by Daqaq [22] and Green et al. [40]. Bidirectional increase of the frequency bandwidth was studied by combining the softening and the hardening stiffness effects in the device proposed by Stanton et al. [92] (Figure 1(a)). The bistable form of the Duffing oscillator was discussed by Cottone et al. [19] and Gammaitoni et al. [35] for noise excitation. Additionally, the concept of stochastic resonance in bistable systems was pointed out by McInnes et al. [64] for use in energy harvesting. Stanton et al. [93] theoretically investigated the bifurcations of a bistable configuration similar to the one tested by Cottone et al. [19] and also presented harmonic balance analysis using a single harmonic [94]. Another important aspect of the bistable Duffing oscillator has been pointed out by Erturk et al. [31] (Figure 1(b))for piezoelectric energy harvesting using a magnetoelastic structure [67]. Large-amplitude interwell oscillations [41] on high-energy orbits of the bistable configuration have been shown to increase the power output by an order of magnitude at several frequencies [31, 33]. Other than magnetoelastic interactions [92, 93, 94, 31, 33, 58], purely elastic buckling was also considered for bandwidth and performance enhancement in energy harvesting [87, 62, 10] (Figure 1(c,d)). A bistable electromagnetic energy harvester was theoretically and experimentally explored by Mann and Owens [60]. In electrostatic energy harvesting, MEMS bistable spring arrangements for bandwidth enhancement were presented by Nguyen et al. [74]. Random excitation of bistable energy harvesters have been studied by using analytical [23, 6, 50], numerical [57, 56, 108], and experimental [108] methods. Recent efforts also include the investigation of nonlinear damping for extending the dynamic range in energy

harvesters [36]. An extensive review on the use of nonlinearities in vibration energy harvesting can be found in a recent article by Daqaq et al. [24]. Other review articles on broadband energy harvesting methods are due to Tang et al. [97], Pellegrini et al. [76], Twiefel and Westermann [101], and Harne and Wang [44]. Most of the existing literature of energy harvesting at meso-scale exploits magnetoelastic interactions with discrete components (e.g. magnets) and buckled structures to create nonlinearities [92, 93, 94, 31, 33, 87, 62, 10, 60]. Examples are shown in Figure 1. Furthermore, energy harvesters employing purely elastic [87, 62, 10] or magnetoelastic [92, 93, 94, 31, 33] buckling often require significantly large excitation levels (on the order of $1g$) to fully exploit large-amplitude nonlinear dynamic phenomena. A particular challenge is to enable bandwidth enhancement with simple designs (i.e. without extra discrete components) and also have these nonlinearities pronounced even for low excitation levels. Additionally, the aforementioned literature dealing with intentionally designed nonlinearities typically overlooked inherently present nonlinearities, which are discussed next for the special case of piezoelectric energy harvesting.

1.3 Inherent Electroelastic Material and Dissipative Nonlinearities

Nonlinearities of piezoelectric materials are manifested in various engineering applications such as sensing, actuation, as well as their combined applications for vibration damping and control, and most recently, energy harvesting from dynamical systems. Literature dealing with the dynamics of electroelastic structures made of piezoelectric materials has explored such nonlinearities in a disconnected way for the separate problems of mechanical and electrical excitation such that nonlinear resonance trends have been assumed to be due to different additional terms in constitutive equations by different researchers[63, 99, 12, 1, 2, 5, 78, 107, 59, 45, 91, 90, 71, 89, 104, 38]. Similar patterns of softening nonlinearities have been attributed to purely elastic nonlinear terms, coupling nonlinearities, or both of these effects, by various authors. After early investigation by Maugin [63] and Tiersten [99] into nonlinear electromechanical effects of piezoelectric materials, the nonlinear analysis of actuated piezoelectric beams started to gain momentum. Aurelle et al. [12] studied the contribution of strain and electromechanical coupling to the nonlinear response of an

actuated beam under low electric field excitation with stress (T_1) modeled as,

$$T_1 = c_{11}S_1 - e_{31}E_3 + \alpha_{111}S_1^2 + \gamma_{311}S_1E_3,$$

where S_1 is the strain, E_3 is the electric field, c_{11} and e_{31} represent the linear elastic and piezoelectric constants in the standard form [63], while α_{111} and γ_{311} are the nonlinear constants. Experimentally shown attenuations in amplitude beyond linear damping was attributed to the electromechanical coupling term γ_{311}. Guyomar et al. [42] justified the approach used by Aurelle et al. [12] by showing that a term proportional to the square of electric field was negligible. Recently Abdelkefi et al. [1, 2] used the constitutive equations suggested by Aurelle et al. [12] for nonlinear piezoelectric energy harvester modeling and simulations. Studying both weak and high electric fields, Wang et al. [106] showed how deviating from weak electric fields increased the effect of electromechanical nonlinearities through third-order elasticity and second-order electric field with a cross S_1E_3 expression in the stress equation. This work also attributed high actuation level attenuation towards nonlinear damping dependent on the electric field. Albareda et al. [5] only considered higher-order elasticity nonlinearities in the formulation of the thermodynamic potential (free electric enthalpy density or the Gibbs free energy density). Priya et al. [78] analyzed high electric field nonlinear elastic and electromechanical nonlinearities but found that the electromechanical terms depended on the square of the strain amplitude. Wolf and Gottlieb [39] also attributed the nonlinear phenomenon of an actuated cantilever in both symmetric (bimorph) and asymmetric (unimorph) configurations to elasticity by considering an electric enthalpy density of

$$H = \frac{1}{2}c_{11}S_1^2 - e_{31}E_3S_1 - \frac{1}{2}\epsilon_{33}E_3^2 + \frac{1}{6}c_3S_1^3 + \frac{1}{24}c_4S_1^4,$$

which results in second- and third-order elastic dependence in the stress equation related to c_3 and c_4 (depending on the bimorph or unimorph arrangement, i.e. symmetry with respect to the reference surface) along with a linear dependence on electric field and electromechanical coupling. This model was experimentally applied by Usher et al. [102] Von Wagner and Hagedorn [104] derived an electric enthalpy density formula to take into account quadratic

and cubic nonlinearities of strain and coupling. The resulting electric enthalpy density expression was

$$H = \frac{1}{2}c_0 S_1^2 + \frac{1}{3}c_1 S_1^3 + \frac{1}{4}c_2 S_1^4 - \gamma_0 S_1 E_3 - \frac{1}{2}\gamma_1 S_1^2 E_3 - \frac{1}{3}\gamma_2 S_1^3 E_3 - \frac{1}{2}\nu_2 E_3^2,$$

where c_1, c_2, γ_1, and γ_2 represent the nonlinear parameters. Also taking a purely geometric nonlinearity approach, Mahmoodi et al. [59] analyzed a MEMS piezoelectrically coupled cantilever. This was validated by assuming low electric field and that material nonlinearities due to strain were an order of magnitude larger than coupling parameters. The analysis shows the importance of the backbone curve, which tracks peak amplitude for increasing voltage excitation levels, in the identification of nonlinear parameters.

Hu et al. [45] analyzed the nonlinear behavior of a shear vibration piezoelectric energy harvester by applying the cubic theory of the displacement gradient initially introduced by Maugin [63] and Tiersten [99]. Higher order electromechanical coupling and electric field terms were neglected due to the weak electric field assumption. Stanton et al. [90, 91] studied the results of higher order strain and electromechanical coupling and attributed experimentally shown peak attenuation at higher excitation levels to a nonlinear quadratic damping term [71]. Later, considering weak electric fields in energy harvesting, the same group [89] reanalyzed the energy harvesting problem by removing higher order electromechanical coupling and considering only elastic nonlinearities up to fifth-order,

$$T_1 = c_{11} S_1 - e_{31} E_3 + c_3 S_1^2 + c_4 S_1^3 + c_5 S_1^4 + c_6 S_1^5,$$

and this approach was suggested to be more consistent, since the electric field levels in energy harvesting are not as high as those in actuation. Finding the results using the models developed by von Wagner [104] and Stanton [90] unsatisfactory, Goldschmidtboeing et al.[38] recently explored the effect of ferroelastic (stress-strain) hysteresis on piezoelectric cantilever beams. This group chose to ignore higher order nonlinear elasticity and nonlinear coupling terms, and instead attribute observed nonlinear effects entirely to hysteresis. This resulted in a constitutive equation of the form,

$$T_1 = c_{11}\left(1 - \alpha|S_1|\right) S_1 - e_{31} E_3,$$

and per cycle energy density dissapation relation,

$$U_{dis} = \frac{4}{3}\gamma c_{11}|S_1|^3,$$

where $|S_1|$ is the strain amplitude, and α and γ are parameters quantifying the hysteretic softening and dissipation effects (not be confused with ferroelectric or dielectric hysteresis effects [46, 21, 86], since electric field levels in energy harvesting are well below the coercive field). The modeling of ferroelastic hysteresis [38] provided a single physical explanation for both the observed nonlinear stiffness and damping effects.

The discrepancy within and between the actuation and energy harvesting nonlinear analyses shows that a unified model of a piezoelectrically coupled beam that works for both problems of two-way coupling does not yet exist. A reliable nonlinear constitutive equation for a given piezoelectric material is expected to be rather unique and valid regardless of the application, e.g. actuation, sensing, or energy harvesting. A systematic approach focusing on the two-way coupling can result in a sound mathematical framework.

1.4 Electrical Circuit and Power Conditioning Nonlinearities

By the nature of vibrations, the electrical power produced by the transducers used in vibration energy harvesting is in the form of alternating current. Since the harvested energy levels are typically low, it is usually necessary to charge a storage component (e.g. a capacitor or a battery), requiring a direct current supply at a fixed voltage. Therefore circuitry is required to rectify the alternating current, filter the rectified signal, and regulate the resulting direct current to match the voltage requirements of the device to be powered. Beyond those requirements, there have been recent efforts by electronics engineers to design more complex circuits to increase the power generated by the harvester[17]. The simplest circuit topology to rectify and filter the harvester output consists of a diode bridge with a smoothing capacitor in parallel with the load. Circuit nonlinearities emerging from nonlinear circuit components are essential to obtaining a stable DC signal. A more advanced rectification and filtering circuit, known as synchronous switched harvesting on inductor (SSHI), has been shown to increase the power conversion efficiency of weakly coupled piezoelectric energy harvesters[43]. This design adds a switched inductor in parallel with the

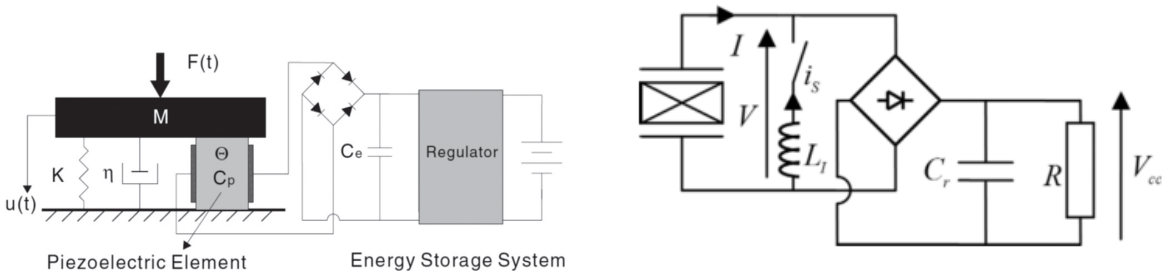

Figure 2: Equivalent circuit model for a piezoelectric energy harvester using the standard rectification and filtering circuit, i.e. the standard AC-DC conversion circuit (left) [85]. Energy harvester circuit schematic using the synchronous switched harvesting on inductor (SSHI) harvesting circuit (right) [43]

piezoelectric transducer before rectification. Both types of circuits are shown in Figure 2.

In the literature of energy harvesting from dynamical systems, mechanical and electrical nonlinear effects have so far predominantly been studied separately[30, 34]. Mechanically and electromechanically nonlinear frameworks[90] have employed linear electrical circuitry to formulate AC input–AC output problems, while the existing efforts on nonlinear circuits[43, 85] have assumed linear mechanical behavior and highly idealized rectifier models. However, even for the simplest case of a cantilever with piezoelectric laminates, nonlinearities in the mechanical domain are required in modeling for accurate prediction of the structural response at relatively high excitation levels, and likewise a stable DC (direct current) signal must be obtained to charge a storage component in realistic energy harvesting applications. Therefore, a complete representation of vibration-based energy harvesting requires simultaneously accounting for geometric, material, and dissipative nonlinearities as well as the nonlinear process of AC-DC conversion.

In 2010, Rupp et al. described a harmonic balance based approach to simulating the coupled behavior of a linear piezoelectric energy harvester connected to a nonlinear rectification circuit[84]. Their method involves a finite element formulation of the electromechanical dynamics of the energy harvester and a circuit-specific implementation of the method of harmonic balance. With the finite element description of the energy harvester structure, more complex design geometries and multiple vibration modes can be simulated at the expense of larger computation times. Nonlinearities can also be included in the finite element

formulation further increasing computational complexity.

For some classes of piezoelectric vibration energy harvesters, the nonlinear electromechanical behavior can be well modeled by a very small number of degrees of freedom. One second order nonlinear ordinary differential equation is typically sufficient to describe the mechanical behavior of energy harvesters excited near a resonant mode well separated from its neighbors. For some geometries, the lumped parameter governing equations may even be derived from first principles. For these types of problems, a finite element approach may not be efficient. If ordinary differential equations governing the nonlinear circuit behavior can also be obtained, then a general harmonic balance solver may be used, rather than a problem-specific implementation.

1.5 Dissertation Outline

Having reviewed the literature of nonlinear energy harvesting (which are specifically grouped into "intentionally designed" and "inherently present" nonlinearities in our context, in addition to the "essential circuit nonlinearities") in this introduction chapter, it is noted that inherent electroelastic material and dissipative nonlinearities in piezoelectric transduction have been overlooked in energy harvesters exploiting intentionally designed nonlinearities. Likewise modeling efforts that include AC-DC conversion or switching circuit nonlinearities oversimplify the mechanical domain. It is the main goal of this dissertation to explore these nonlinearities as well as their interactions through rigorous modeling and experiments within a complete, unified framework. Therefore, the following chapters are outlined as follows: Chapter 2 describes a platform for piezoelectric energy harvesting designed to exhibit a pronounced geometric nonlinearity to increase the response bandwidth. Chapter 3 details the design and analysis of a piezoelectric vibration energy harvester based on platform explained in the previous chapter. Chapter 4 deals with the derivation and validation of a unified modeling framework of the nonlinear constitutive behavior of soft piezoceramics commonly used for piezoelectric energy harvesters and actuators. In Chapter 5, this modeling framework is used to extract and identify nonlinear material parameters of soft piezoceramics. In Chapter 6, the given framework is extended to also handle the strong circuit nonlinearities

caused by AC–DC rectification for practical energy harvesting applications and validated experimentally. Chapter 7 concludes this dissertation by summarizing the contributions made to the field of piezoelectric vibration energy harvesting and opportunities for further work. A derivation of a general Newton's method enabled harmonic balance solver and a MATLAB implementation used extensively in this research are included in Appendices A and B.

Chapter II

AN M-SHAPED OSCILLATOR FOR ENHANCED BANDWIDTH

2.1 Introduction

Over the past few years, nonlinear oscillators have been given growing attention due to their ability to enhance the performance of energy harvesting devices by increasing the frequency bandwidth. Duffing oscillators are a type of nonlinear oscillator characterized by a symmetric hardening or softening cubic restoring force. In order to realize the cubic nonlinearity in a cantilever at reasonable excitation levels, often an external magnetic field or mechanical load is imposed, since the inherent geometric nonlinearity would otherwise require impractically high excitation levels to be pronounced. As an alternative to magnetoelastic structures and other complex forms of symmetric Duffing oscillators, an M-shaped nonlinear bent beam with clamped end conditions is presented and investigated for bandwidth enhancement under base excitation. The proposed M-shaped oscillator made of spring steel is very easy to fabricate as it does not require extra discrete components to assemble, and furthermore, its asymmetric nonlinear behavior can be pronounced yielding broadband behavior under low excitation levels. For a prototype configuration, linear and nonlinear system parameters extracted from experiments are used to develop a lumped-parameter mathematical model. Quadratic damping is included in the model to account for nonlinear dissipative effects. A multi-term harmonic balance solution is obtained to study the effects of higher harmonics and a constant term. A single-term closed-form frequency response equation is also extracted and compared with the multi-term harmonic balance solution. The M-shaped configuration can easily be exploited in piezoelectric and electromagnetic energy harvesting as well as their hybrid combinations due to the existence of both large strain and kinetic energy regions. A demonstrative case study is given for electromagnetic energy harvesting, revealing the importance of higher harmonics and the need for multi-term harmonic balance analysis for predicting the electrical power output

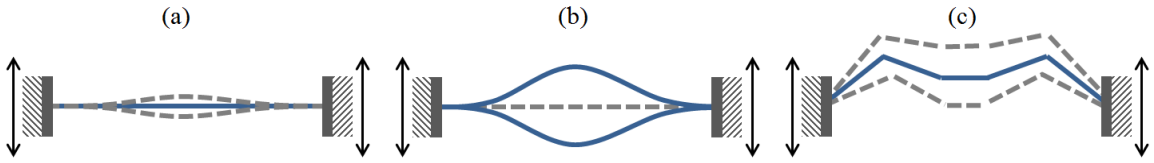

Figure 3: Clamped-clamped beams under base excitation: (a) Monostable configuration with no compressive preload (exhibits limited stretching capability); (b) bistable configuration due to compressive axial preloading (requires large excitation for interwell oscillations); and (3) pre-bent nonlinear M-shaped monostable configuration (exhibits large stretching capability) studied in this work. Solid blue lines indicate the static equilibrium configurations.

accurately.

Figure 3 summarizes the physical motivation for the M-shaped oscillator explored in this work and its advantages over the standard clamped-clamped monostable and bistable configurations. A clamped-clamped beam with no compressive preload, as shown in Figure 3(a), can exhibit hardening nonlinearity to increase response bandwidth as well as protect against dangerously large strains in attached piezoelectric laminates. However, since hardening is due to the relatively large axial stiffness opposing extensional deformation, maximum deflections will be small, severely limiting power generation capabilities. As depicted in Figure 3(b), introducing a compressive axial preload to induce buckling yields a structure that can snap between two large deflection configurations (as long as the potential wells [103] are overcome in response to dynamic excitation), greatly increasing power output while still maintaining upper limits on piezoelectric laminate deformation. Dynamic snap-through behavior [87, 62, 10] typically requires large excitation levels, limiting bistable energy harvesters to high excitation applications. A pre-bent monostable beam structure, the M-shaped configuration shown in Figure 3(c), can exhibit both limited maximum deflections to protect piezoelectric laminates and advantageous nonlinear dynamic behavior at low excitation levels due to large stretching capabilities. In the present work, the nonlinear dynamic behavior of the system is explored through experiments and multi-term harmonic balance modeling, in addition to presenting a simple platform for broadband piezoelectric and electromagnetic energy harvesting as well as their hybrid configurations.

In the following, first the M-shaped bent beam configuration with clamped end conditions is described for broadband vibration energy harvesting under base excitation. The focus is placed on the experimental system and identification of the linear and nonlinear system parameters for modeling and nonlinear analysis. The force-displacement relationship of the M-shaped beam with a central lumped mass attachment is experimentally obtained and asymmetric nonlinear behavior is verified. Linear and nonlinear system parameters extracted from experiments are used to develop a lumped-parameter mathematical model. A multi-term harmonic balance solution is obtained to study the effects of higher harmonics and a constant steady-state term resulting from asymmetry. A single-term closed-form frequency response equation is also extracted and compared with the multi-term harmonic balance solution. Finally, a case study is given for electromagnetic energy harvesting to further demonstrate the importance of higher terms in the harmonic balance analysis. The present work focuses on the meso-scale implementation, experimentally validated modeling, and analysis of a nonlinear spring architecture formerly used in MEMS-scale [73, 100] electrostatic energy harvesting.

2.2 M-shaped Nonlinear Oscillator and Energy Harvester Configurations

Top and isometric views of the M-shaped oscillator configuration along with its clamp and shaker mount are shown in Figure 4. Although this configuration can be fabricated at different geometric scales, the M-shaped oscillator analyzed in this work consists of a beam made from 25.4 mm wide by 0.254 mm thick AISI 1075 spring steel. The steel is cut and bent using common sheet metal tools. The bend angles used are small enough to allow near zero radius bends without first heating the metal. The lumped mass attachment consists of eight 12.7x12.7x3.18 mm^3 permanent magnets, half on each side of the spring. Magnets are chosen due to their ease of attachment to the steel spring, rather than to subject the system to any magnetic force effects, therefore the lumped mass does not have to be made of magnets, and likewise the M-shaped structure does not have to be ferromagnetic. The total lumped mass attachment is 30.4 grams. Both ends of the oscillator are clamped. The clamp and shaker mount are made from 6061 aluminum.

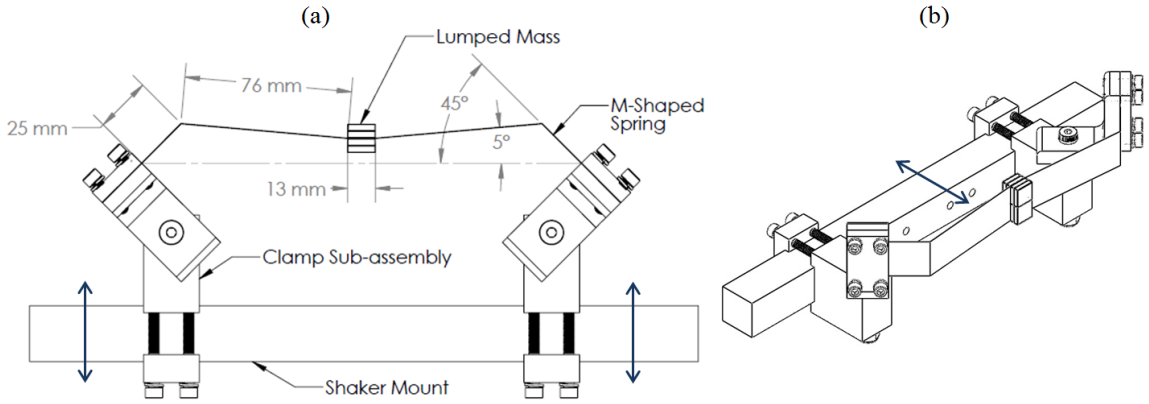

Figure 4: (a) Top and (b) isometric model views of M-shaped oscillator with its fixture. Vibration input is provided from the shaker mount (arrows indicating the direction of mechanical base excitation

While the present work is focused mainly on the nonlinear oscillator structure, electrical power generation can be achieved by adding proper electromechanical coupling interface elements to the elastic oscillator. Figure 5 (a) shows the M-shaped oscillator with four piezoelectric patches bonded near the clamps (resulting in two bimorphs). Dynamic bending of the spring causes tensile and compressive strains on the piezoelectric layers, yielding an alternating voltage via the direct piezoelectric effect, which is then connected to an electrical load for AC power generation or rectified and conditioned in an energy harvesting circuit to obtain a stable DC signal for charging a storage component [75, 85, 47, 17]. If a permanent magnet is used as the proof mass, power may be generated by attaching a coil to the base of the oscillator, as shown in Figure 5 (b). The motion of the permanent magnet relative to the coil creates a changing magnetic field inside the coil, which according to Faraday's law produces a current in the coil. The AC electrical output is then connected to the load or a proper electromagnetic energy harvesting circuit. Both of these electromechanical coupling methods can be employed simultaneously. The resulting hybrid piezoelectric-electromagnetic energy harvester is shown in Figure 5 (c). In the present effort, focus is predominantly placed on the purely mechanical nonlinear dynamics of the M-shaped structure.

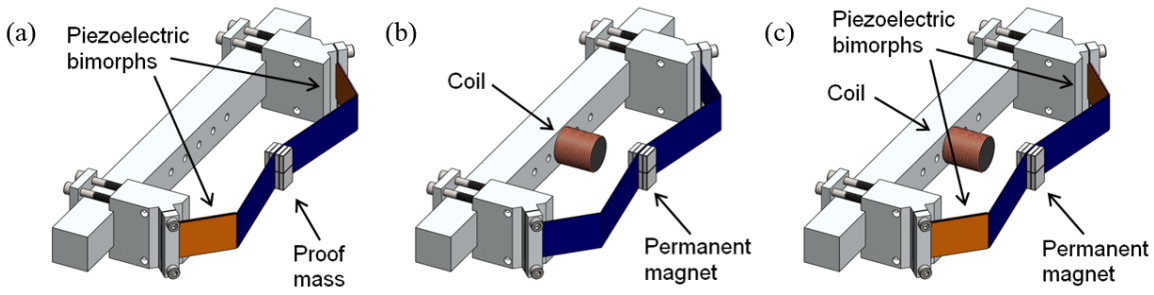

Figure 5: M-shaped piezoelectric and/or electromagnetic energy harvester configurations employing (a) piezoelectric patches attached to high strain energy regions, (b) a coil-magnet arrangement attached to high kinetic energy region, and (c) combination of the previous two to form a hybrid design. Terminals of the piezoelectric patches and/or coil are connected to electrical loads or a more complex energy harvesting circuit.

2.3 Experimental System, Mathematical Model, and Parameter Identification

This section introduces the experimental system used for testing and analyzing the M-shaped nonlinear oscillator prototype. The stiffness, mass, and damping properties of the M-shaped oscillator are identified and tabulated prior to nonlinear modeling and analyses in the next sections.

2.3.1 Experimental Setup

Experiments are conducted using an APS-113 seismic shaker driven by an APS-125 amplifier and controlled by a SPEKTRA VCS-201 controller. These devices allow for the sample to be subjected to harmonic base acceleration at specified amplitudes and frequencies. Tests consist of up and down frequency sweeps at a constant kinematic variable (in this case base acceleration amplitude) necessary for frequency response analysis of the nonlinear system. Base acceleration measured by a Kistler model 8636C50 ICP accelerometer is used for feedback to the VCS-201 controller. A Polytec PDV-100 Portable Digital Vibrometer is used to measure the base velocity. The velocity and displacement of the lumped mass (i.e. center of the M-shaped oscillator) are measured using a Polytec OFV-505 sensor head and OFV-5000 controller with a displacement decoder. Data is acquired using a National Instruments NI USB-4431 unit. Overview and detail views of the experimental setup are shown in Figure 6.

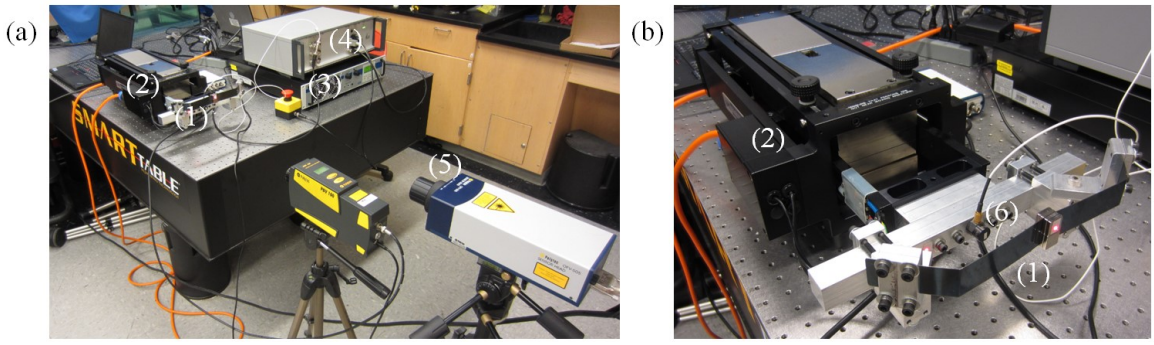

Figure 6: (a) Overview and (b) detail pictures of experimental setup: (1) M-shaped oscillator; (2) long-stroke shaker; (3) amplifier; (4) controller; (5) laser vibrometers; (6) accelerometer. The M-shaped oscillator is attached to the armature of the shaker through its fixture for horizontal base excitation.

2.3.2 Mathematical Model

The M-shaped oscillator is modeled as a single-degree-of-freedom system with linear viscous and quadratic damping terms along with a nonlinear elastic restoring force undergoing base excitation (Figure 3). The equation of motion of such a system is

$$m\ddot{z} + 2\zeta\omega_n m\dot{z}\left(1 + \gamma\left|\dot{z}\right|\right) + f(z) = -m'\ddot{y} \tag{1}$$

where m is the equivalent mass of the oscillator, m' is the effective mass that causes the forcing term due to base excitation ($m = m'$ if the spring mass is negligible as compared to the lumped mass attachment), ζ is the linear viscous damping ratio, γ is a constant that accounts for the quadratic damping, ω_n is the linear natural frequency, $f(z)$ is the nonlinear elastic restoring force, $y(t)$ is the base displacement measured in an inertial frame, $z(t)$ is the displacement of the oscillator relative to the moving base, and an $\dot{(\,)}$ represents differentiation with respect to time. Note that the displacement of the mass relative to the fixed reference frame is denoted by $x(t)$ in Figure 7, therefore the displacement relative to the base is $z(t) = x(t) - y(t)$.

2.3.3 Parameter Identification

In order to investigate the nonlinear system dynamics theoretically, it is necessary to identify the relevant parameters of the M-shaped oscillator. First the relationship between deflection

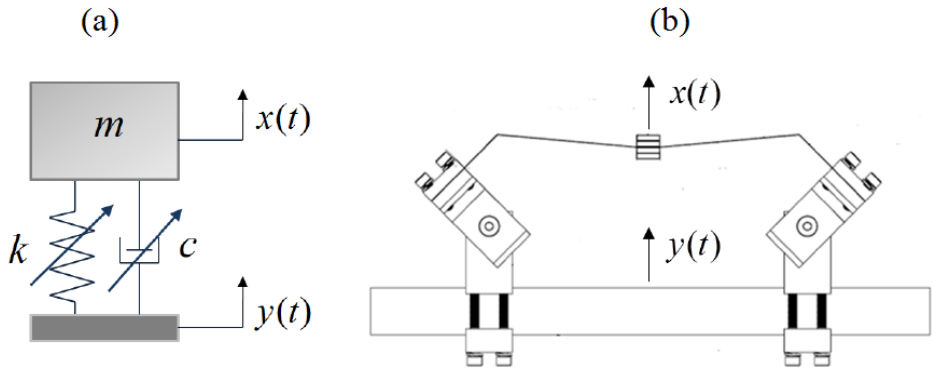

Figure 7: (a) Lumped-parameter model and (b) device schematics of the M-shaped nonlinear oscillator under base excitation (stiffness and damping components are nonlinear).

and restoring force, $f(z)$, is extracted. To this end, the oscillator is bolted to the rigid optical table vertically (to set $y = 0$ so that $x = z$). With the lumped mass attachment removed (to avoid any sag due to gravity), weights are suspended from the center of the spring. Deflection is measured using the OFV-5000 displacement decoder of the laser vibrometer. The sample is turned over and the process repeated. It is assumed that the weight of the spring itself is negligible compared to the suspended weights. Reasonably, it is also assumed the removal of the mass attachments does not change the stiffness characteristics of the spring. As shown in Figure 8, a third-order polynomial of the following form is fit to the measured force-displacement data:

$$f(z) = k_1 z + k_2 z^2 + k_3 z^3, \tag{2}$$

where $k_1 = 229.61\ N/m$, $k_2 = 8289.4\ N/m^2$, and $k_3 = -750840\ N/m^3$ are constant coefficients on the first, second, and third order terms, respectively (in particular, $k_1 = m\omega_n^2$). Any constant term (coefficient of zeroth order term) of the polynomial fit is set to be zero, as the force-displacement relationship should pass through the origin. The linear coefficient can be interpreted as the linear spring stiffness, and the cubic and quadratic coefficients as the symmetric and asymmetric nonlinear stiffness terms, respectively. Note that the inflection point of the curve occurs in Figure 8 at a deflection of approximately 5 mm. The amount of asymmetry depends on the overall structural design and geometric parameters. While the much smaller asymmetry leads to an expectation of more classical

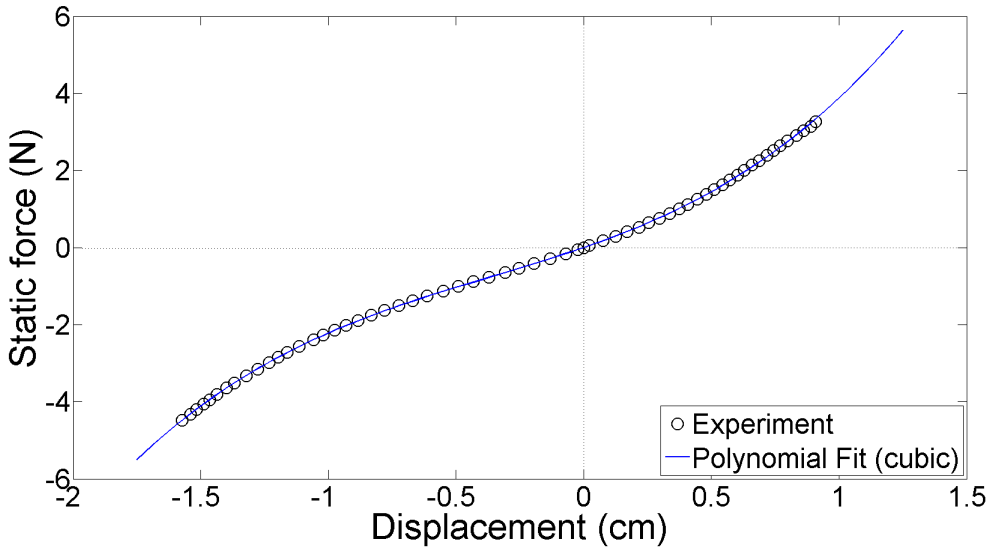

Figure 8: Experimental static force-displacement relationship and third-order polynomial curve fit.

Duffing oscillator behavior, the asymmetry is present, and further investigation on the relationship between the multiple geometric parameters of the spring design and its force-displacement characteristics is of interest for future research. In order to identify the linear damping and linear natural frequency of the system, the M-shaped oscillator (with mass attachments) is clamped horizontally to the table (to eliminate any displacements and sag due to gravity in the presence of the proof mass) and given a small initial excitation. The measured displacement time series for the linear free vibration test is shown in Figure 9. It is known from the elementary theory of vibrations [98, 65] that the natural response of a linear underdamped system decays in an exponential envelope as

$$x(t) = Xe^{-\zeta\omega_n t}\cos(\omega_d t - \phi), \tag{3}$$

where ω_d is the damped natural frequency. Fitting an exponential curve to the peaks of the time series yields $\zeta\omega_n$. The damped natural frequency is found from the period of oscillation. Damping for this system is extremely light, so the approximation $\omega_n \approx \omega_d$ is used safely. Therefore the values of $\omega_n = 84.3$ rad/s and $\zeta = 0.0011$ are obtained for the natural frequency and damping ratio, respectively. The equivalent mass is obtained from the linear stiffness component and natural frequency as $m = 0.0323$ kg. This identified equivalent mass of

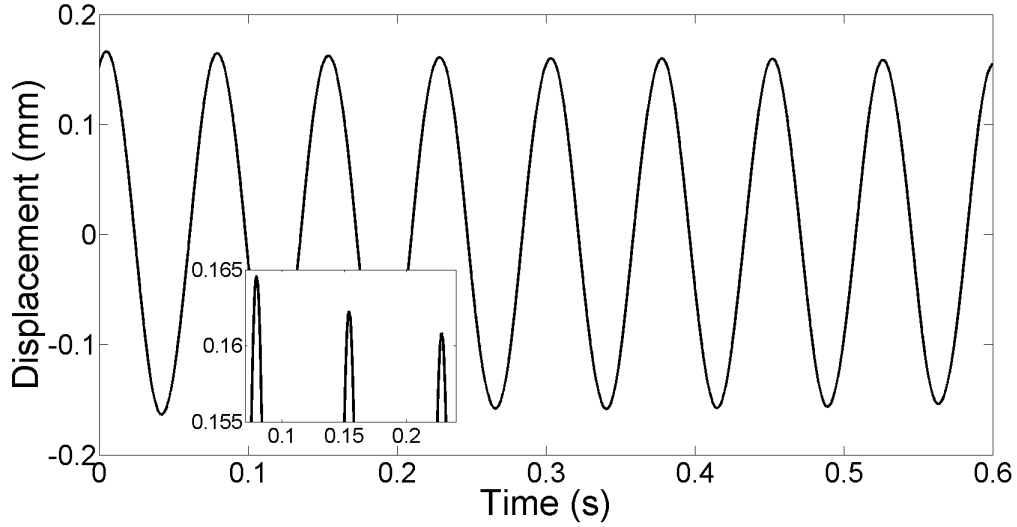

Figure 9: Time series of free vibration for linear parameter identification.

32.3 grams is consistent with the value of the attached mass of 30.4 grams. The proof mass attachment indeed makes up the majority of the equivalent mass as intended, and the contribution from the effective spring mass is minor. Finally, the quadratic damping term (γ) in Equation 3 is found to be necessary, as without it, the model tended to overestimate the amplitude and frequency of the upper saddle-node bifurcation point at which the jump phenomenon [41] takes place in the up sweep in the frequency response curves. The physical justification of quadratic (or velocity-squared) damping is nonlinear fluid damping (see, for instance, Bandstra [13], among others). It is indeed plausible that nonlinear air damping [13] would be significant, as velocities in excess of 1 m/s were observed in the experiments (see Equation 1 and note that the identified value of nonlinear damping term is 1 s/m, i.e. the linear and nonlinear dissipation components are on the same order of magnitude). The value of γ is estimated from the comparison of experimental and simulated response curves discussed in Section 2.5.1. The identified linear and nonlinear model parameters are summarized in Table 1.

2.4 Nonlinear Analysis Using the Method of Harmonic Balance

The second-order nonlinear equation of motion, Equation 1, can be expressed in the form of two nonlinear first-order equations for time-domain numerical simulations (e.g. by using

Table 1: Identified model parameters.

m	0.0323 kg
k_1	229.61 N/m
k_2	8289.4 N/m^2
k_3	750840 N/m^3
ω_n	84.3 rad/s
ζ	0.0011
γ	1 s/m

ode45 in MATLAB). However, numerical simulation in time domain to generate frequency response curves is undesirable, since the process can be computationally lengthy, numerical errors may build up over the course of the simulation, and little insight into the underlying mathematics of the problem is gleaned. A number of approximate solution and perturbation methods exist for the analysis of nonlinear ordinary differential equations, such as the Lindstedt-Poincaré method, the method of multiple scales, the Krylov-Bogoliubov averaging method, and the method of harmonic balance [72]. The system studied here exhibits a high degree of nonlinearity and therefore it is required to explore multi-harmonic solutions for enhanced accuracy. Harmonic balance is the analysis method that most easily accommodates multi-term approximate solutions. In the following, first the multi-harmonic solution is given by accounting for higher harmonics and a DC (constant) component, and then the single-harmonic solution with a closed-form frequency response equation is presented.

2.4.1 Multi-Harmonic Solution

The base excitation term is assumed to be harmonic of the form

$$\ddot{y}(t) = A\cos(\Omega t) \tag{4}$$

where A is the acceleration amplitude and Ω is the driving frequency. A Fourier series solution with the same period as the forcing is assumed for the vibration response ($z(t) = x(t) - y(t)$) relative to the moving base (see Figure 7). The displacement, velocity, and

acceleration of the mass relative to the moving base are then

$$\begin{aligned} z(t) &= a_0 + \sum_{n=1}^{\infty} \left[a_n \cos\left(n\Omega t\right) + b_n \sin\left(n\Omega t\right)\right] \\ &= a_0 + \sum_{n=1}^{\infty} Z_n \cos\left(n\Omega t + \phi_n\right) \end{aligned} \tag{5}$$

$$\begin{aligned} \dot{z}(t) &= a_0 + \sum_{n=1}^{\infty} n\Omega \left[-a_n \sin\left(n\Omega t\right) + b_n \cos\left(n\Omega t\right)\right] \\ &= -\sum_{n=1}^{\infty} n\Omega Z_n \sin\left(n\Omega t + \phi_n\right) \end{aligned} \tag{6}$$

$$\begin{aligned} \ddot{z}(t) &= a_0 + \sum_{n=1}^{\infty} -\left(n\Omega\right)^2 \left[a_n \cos\left(n\Omega t\right) + b_n \sin\left(n\Omega t\right)\right] \\ &= -\sum_{n=1}^{\infty} \left(n\Omega\right)^2 Z_n \cos\left(n\Omega t + \phi_n\right), \end{aligned} \tag{7}$$

which is an exact representation with infinitely many terms. Note that the relative displacement given by Equation 5 accounts for the constant term a_0 resulting from the asymmetric system behavior. In order to obtain an approximate solution, Equations 5-7 have to be truncated to include finite number of terms (harmonics). The truncated form of Equation 5 is

$$z_N(t) = a_0 + \sum_{n=1}^{N} \left[a_n \cos\left(n\Omega t\right) + b_n \sin\left(n\Omega t\right)\right] = a_0 + \sum_{n=1}^{N} Z_n \cos\left(n\Omega t + \phi_n\right) \tag{8}$$

which includes N harmonics. As the system has both quadratic and cubic stiffness nonlinearities, which are associated with the generation of predominant second and third harmonics in the response under hard forcing [71], the truncated Fourier series representation should contain sufficient terms ($N = 3$ is used in this work). As mentioned in Section 2.3.3, the observed nonlinear damping was characterized as quadratic and attributed to air damping [13]. While numerical simulation easily handles the non-smooth absolute value function present in the physical model, it is required for the multi-term harmonic balance analysis to introduce an equivalent viscous damping coefficient c and re-express the equation of motion as

$$m\ddot{z} + c\dot{z} + k_1 z + k_2 z^2 + k_3 z^3 + m\ddot{y} = 0, \tag{9}$$

where the viscous damping coefficient is obtained by calculating the energy dissipated in the system by considering only the dominant harmonic as an approximation:

$$c = 2m\zeta\omega_n \left(1 + \gamma \frac{8\Omega Z_1}{3\pi}\right) \tag{10}$$

Then, substitution of the truncated Fourier series into the equation of motion yields the residual function:

$$R(t) = m\ddot{z}_N + c\dot{z}_N + k_1 z_N + k_2 z_N^2 + k_3 z_N^3 + mA\cos(\Omega t) \tag{11}$$

Using the Galerkin method of mean weighted residuals, a system of algebraic equations in the harmonic amplitudes is generated:

$$\int_0^{\frac{2\pi}{\Omega}} R(t)dt = 0 \tag{12}$$

$$\int_0^{\frac{2\pi}{\Omega}} R(t)\cos(n\Omega t)dt = 0 \tag{13}$$

$$\int_0^{\frac{2\pi}{\Omega}} R(t)\sin(n\Omega t)dt = 0 \tag{14}$$

The choice to include a constant term (a_0) and three harmonics (a_n, b_n, $n = 1, 2, 3$) in the assumed solution yields a root finding problem of seven equations for seven unknowns:

$$\begin{aligned}
&8k_3a_0^2 - 6k_3b_1^2a_2 + 6k_3a_1^2a_2 + 12k_3a_0b_3^2 + 12k_3a_0a_2^2 + 12k_3a_0b_2^2 \\
&+ 12k_3a_0a_3^2 + 12k_3a_0a_1^2 + 12k_3a_0b_1^2 + 8k_1a_0 + 4k_2b_2^2 + 4k_2a_3^2 \\
&+ 4k_2b_3^2 + 4k_2a_1^2 + 4k_2b_1^2 + 4k_2a_2^2 + 8k_2a_0^2 + 12k_3b_1a_2b_3 \\
&+ 12k_3a_1b_2b_3 + 12k_3a_1a_2a_3 + 12k_3a_1b_1b_2 - 12k_3b_1b_2a_3 = 0
\end{aligned} \tag{15}$$

$$\begin{aligned}
&4k_1a_1 + 3k_3a_1^3 + 3k_3a_1b_1^2 + 6k_3a_1b_3^2 + 6k_3a_1b_2^2 + 6k_3a_1a_3^2 + 6k_3a_1a_2^2 \\
&+ 12k_3a_0b_1b_2 + 12k_3a_0a_2a_3 + 12k_3a_0b_2b_3 + 6k_3a_1b_1b_3 + 3k_3a_1^2a_3 + 4k_2a_1a_2 \\
&- 3k_3b_2^2a_3 + 3k_3a_2^2a_3 - 3k_3b_1^2a_3 + 4k_2b_2b_3 + 4k_2a_2a_3 + 4k_2b_1b_2 + 4cb_1\Omega \\
&+ 8k_2a_0a_1 + 12k_3a_0^2a_1 + 12ka_0a_1a_2 + 6k_3a_2b_2b_3 - 4ma_1\Omega^2 + 4mA = 0
\end{aligned} \tag{16}$$

$$12k_3a_0a_1b_2 - 12k_3a_0b_2a_3 + 12k_3a_0a_2b_3 - 12k_3a_0b_1a_2 + 6k_3a_2b_2a_3 - 6k_3a_1b_1a_3$$
$$+ 6k_3b_1b_2^2 - 3k_3a_2^2b_3 + 3k_3a_1^2b_1 + 12k_3a_0^2b_1 + 4k_2a_2b_3 - 4k_2b_2a_3$$
$$+ 4k_2a_1b_2 - 4k_2b_1a_2 + 8k_2a_0b_1 + 3k_3a_1^2b_3 + 6k_3b_1a_2^2 - 3k_3b_1^2b_3$$
$$+ 6k_3b_1a_3^2 + 6k_3b_1b_3^2 - 4m\Omega^2b_1 - 4c\Omega a_1 + 3k_3b_1^3 + 4k_1b_1 = 0 \tag{17}$$

$$4k_1a_2 + 3k_3a_2^3 + 2k_2a_1^2 - 2k_2b_1^2 + 4k_2b_1b_3 + 3k_3a_2b_2^2 + 12k_3a_0a_1a_3$$
$$+ 6k_3b_1^2a_2 + 6k_3a_1^2a_2 + 6k_3a_0a_1^2 - 6k_3a_0b_1^2 + 8cb_2\Omega + 8k_2a_0a_2$$
$$+ 4k_2a_0a_2 + 4k_2a_1a_3 - 16ma_2\Omega^2 + 12k_3a_0^2a_2 + 6k_3a_2b_3^2 + 6k_3a_2a_3^2$$
$$+ 6k_3a_1a_2a_3 + 6k_3b_1b_2a_3 - 6k_3b_1a_2b_3 + 6k_3a_1b_2b_3 + 12k_3a_0b_1b_3 = 0 \tag{18}$$

$$4k_1b_2 - 16m\Omega^2b_2 - 8c\Omega a_2 + 3k_3b_2^3 + 4k_2a_1b_3 + 4k_2a_1b_1 + 6k_3b_1a_2a_3$$
$$- 4k_2b_1a_3 + 3k_3a_2^2b_2 + 6k_3b_2b_3^2 + 6k_3b_1^2b_2 + 6k_3b_2a_3^2 + 6k_3a_1^2b_2$$
$$+ 12k_3a_0^2b_2 + 8k_2a_0b_2 + 12k_3a_0a_1b_1 - 6k_3a_1b_2a_3 + 6k_3a_1a_2b_3$$
$$+ 6k_3b_1b_2b_3 + 12k_3a_0a_1b_3 - 12k_3a_0b_1a_3 = 0 \tag{19}$$

$$4k_1b_2 - 16m\Omega^2b_2 - 8c\Omega a_2 + 3k_3b_2^3 + 4k_2a_1b_3 + 4k_2a_1b_1 + 6k_3b_1a_2a_3$$
$$- 4k_2b_1a_3 + 3k_3a_2^2b_2 + 6k_3b_2b_3^2 + 6k_3b_1^2b_2 + 6k_3b_2a_3^2 + 6k_3a_1^2b_2$$
$$+ 12k_3a_0^2b_2 + 8k_2a_0b_2 + 12k_3a_0a_1b_1 - 6k_3a_1b_2a_3 + 6k_3a_1a_2b_3$$
$$+ 6k_3b_1b_2b_3 + 12k_3a_0a_1b_3 - 12k_3a_0b_1a_3 = 0 \tag{20}$$

$$3k_3b_3^3 + 4k_1b_3 - k_3b_1^3 + 6k_3a_1a_2b_2 - 12c\Omega - 36m\Omega^2b_3$$
$$+ 3k_3b_1b_2^2 + 6k_3a_2^2b_3 + 6k_3b_2^2b_3 + 3k_3a_1^2b_1 + 4k_2a_1b_2 + 4k_2b_1a_2$$
$$+ 6k_3a_1^2b_3 - 3k_3b_1a_2^2 + 6k_3b_1^2b_3 + 8k_2a_0b_3 + 3k_3a_3^2b_3 + 12k_3a_0^2b_3$$
$$+ 12k_3a_0a_1b_2 + 12k_3a_0b_1a_2 = 0 \tag{21}$$

Since a closed-form solution is impossible, the multivariate Newton-Raphson method is employed to solve for the unknowns. The problem is cast into vector form, with $\mathbf{x}$ being the i-th iterate of the vector of a_0, a_n, and b_n:

$$\mathbf{f}(\mathbf{x}) = \mathbf{0} \tag{22}$$

$$\mathbf{x}_{i+1} = \mathbf{x}_i - [J(\mathbf{x}_i)]^{-1}\,\mathbf{f}(\mathbf{x}_i) \tag{23}$$

It should be highlighted once again that the main reason for keeping higher harmonics (n = 2, 3) is to explore the effect of these terms in the frequency response with comparisons to experimental measurements and numerical simulations. Otherwise including more than one harmonic term drastically complicates the resulting system of algebraic equations. Nevertheless this procedure of accounting for higher harmonics in the harmonic balance analysis is more efficient than time-domain numerical simulations. For systems with low damping, time-domain numerical simulations must involve large numbers of cycles to converge to steady state response, whereas only a few iterations of the Newton-Raphson method yield convergent harmonic balance. Depending on the choice of simulation parameters, time-domain simulations may take an order of magnitude or more time than the multi-term harmonic balance method solved with the Newton-Raphson method.

2.4.2 Single-Harmonic Closed-Form Solution

If the constant term (a_0) is neglected and only a single harmonic term is used in Equation 8, the resulting algebraic equation is simplified dramatically and it is possible to obtain a closed-form frequency response equation. Equations 12-14 reduce to

$$\int_0^{\frac{2\pi}{\Omega}} R(t)\cos(\Omega t)dt = 0 \tag{24}$$

$$\int_0^{\frac{2\pi}{\Omega}} R(t)\sin(\Omega t)dt = 0 \tag{25}$$

and the assumed response form to be used in the residual expression is

$$z(t) = Z_1\cos(\Omega t + \phi) \tag{26}$$

yielding

$$k_1 Z_1 - m\Omega^2 Z_1 + \frac{3}{4} k_3 Z^3 + mA\cos\phi = 0 \tag{27}$$

$$-c\Omega Z_1 + mA\sin\phi = 0 \tag{28}$$

The phase term in Equations 27 and 28 can then be eliminated to give the frequency response equation:

$$\left(k_1 Z_1 - m\Omega^2 Z_1 + \frac{3}{4} k_3 Z^3\right)^2 + (c\Omega Z_1)^2 = (mA)^2 \tag{29}$$

which is the same result that can be obtained using alternative perturbation methods [71, 72] for this simplified case of using a single harmonic. It should be noted that the quadratic nonlinearity term vanishes in this single-term approximation. Therefore the error in single-term approximation is expected to grow with increasing contribution from the quadratic stiffness term.

2.5 Experimental Results, Model Validation, and Case Study

Using the experimental setup shown in Figure 6, up and down frequency sweep experiments are conducted at fixed base acceleration levels to extract the nonlinear frequency response functions of the M-shaped harvester for verification of broadband behavior and validation of the mathematical model and its solution. Effects of higher harmonics in harmonic balance analysis is discussed and also demonstrated in a case study for electromagnetic energy harvesting.

2.5.1 Model Validation at Different Excitation Levels

By using the feedback shaker system (Figure 6), up and down frequency sweep experiments are conducted at RMS (root-mean-square) base acceleration levels of $0.03g$, $0.05g$, and $0.07g$. The results of these experiments are shown in Figure 10. The displacement frequency response curves discussed in this section are relative to the inertial frame, i.e. the displacement x (see Figure 7) is plotted in the frequency response graphs.

In Figure 10, the bottom, middle, and top RMS displacement response relationships correspond to low base acceleration RMS values of $0.03g$, $0.05g$, and $0.07g$, respectively. The

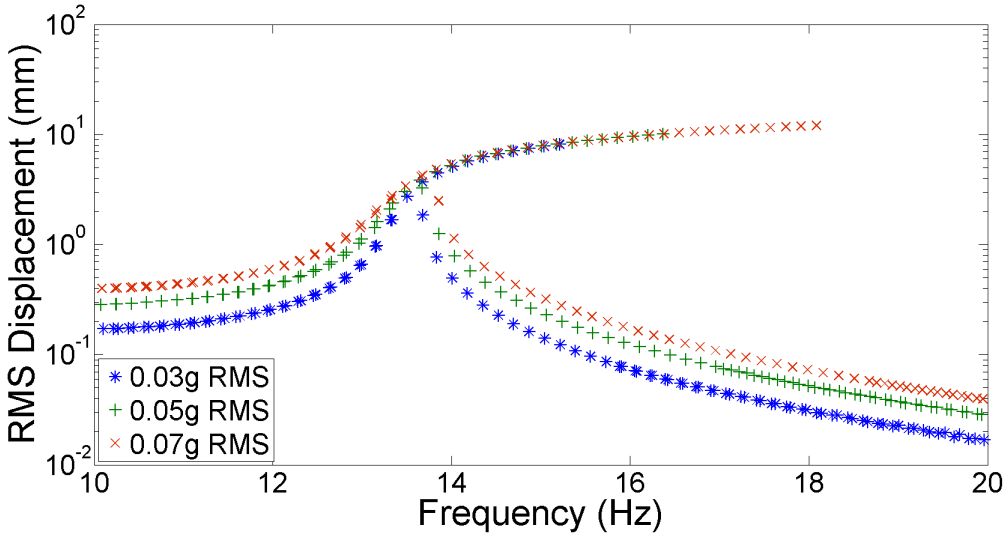

Figure 10: Experimental displacement frequency response curves of the M-shaped oscillator at $0.03g$, $0.05g$, and $0.07g$ RMS base acceleration levels (up- and down-sweep curves are shown together).

system exhibits significant nonlinear behavior in all three cases. As the base acceleration level increases, the increase in peak displacement amplitude becomes saturated, while the bandwidth of the response continues to grow. The system shows 3 dB (half-power point) bandwidths of 1.0 Hz, 1.7 Hz, and 2.7 Hz for the respective excitation levels. As a fraction of the linear resonant frequency, the bandwidths are 7.5%, 12.7%, and 20.1%, respectively. To compare, an ideal linear system with the same linear parameters would have a 3 dB bandwidth of approximately 0.03 Hz (with a much higher maximum amplitude due to the very light linear damping). Consequently the M-shaped harvester offers 3200%, 5600%, and 8900% bandwidth enhancement at the RMS base excitation levels of $0.03g$, $0.05g$, and $0.07g$, respectively. The nonlinear system displays substantial bandwidth enhancement even for these low base acceleration levels.

In order to validate the mathematical model presented in this work, both time-domain numerical simulations (using ode45 in MATLAB) and harmonic balance (Section 2.4) results are obtained and compared with experiments. For the lowest base excitation level of $0.03g$ RMS, experimental, numerical, and harmonic balance results are shown in Figure 11 along with a detail view of the large response branch. The harmonic balance results are given

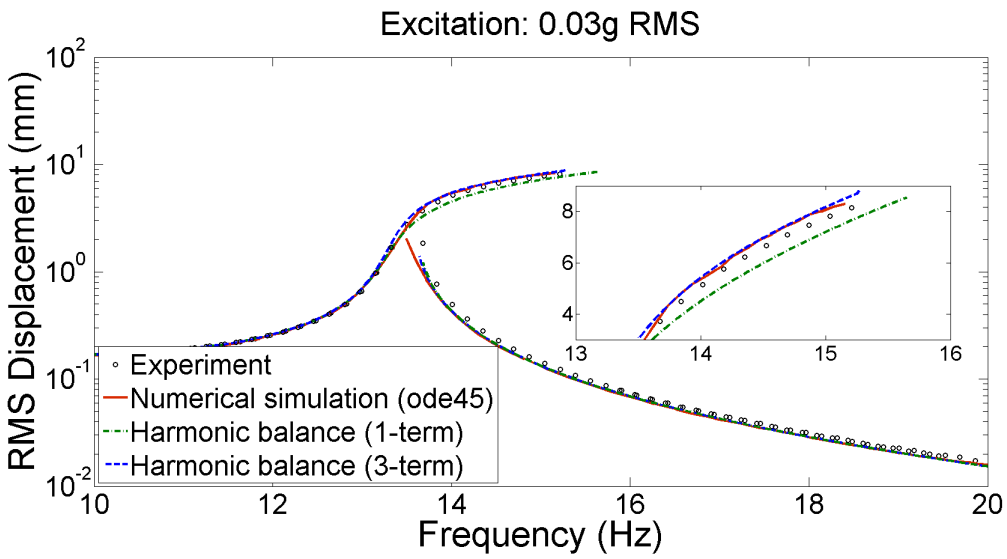

Figure 11: Displacement frequency response curves of the M-shaped oscillator at $0.03g$ RMS base acceleration level for up and down sweep: Experimental measurement, time-domain numerical simulation, and harmonic balance solutions (1-term and 3-term).

for 1-term and 3-term solutions. It is observed that the agreement between the harmonic balance and time-domain numerical simulations is improved substantially as the number of harmonics is increased from $N = 1$ to $N = 3$. Specifically the 1-term harmonic balance solution underestimates the response amplitude over the large-amplitude branch and overestimates the frequency of the upper saddle-node bifurcation point. Overall, the 3-term solution exhibits much better agreement with the experimental results and time-domain numerical solution as compared to the 1-term solution.

Further comparisons are given for the excitation levels of $0.05g$ and $0.07g$ RMS. For all excitation levels, the 3-term harmonic balance solution agrees closely with the time-domain numerical simulation. In the neighborhood of the up-sweep jump in the frequency response, both deviate from the experimental result. The numerical results overestimate the response, likely due to additional unmodeled dissipation and stiffness effects. Damping is assumed to be well-modeled by a combination of linear viscous and quadratic damping in the lumped-parameter model, while other dissipative effects may be significant. Terms of higher order may also start to be significant in the elastic restoring force. In all cases, the time-domain simulation and 3-term harmonic balance solution provide a better estimate of the frequency

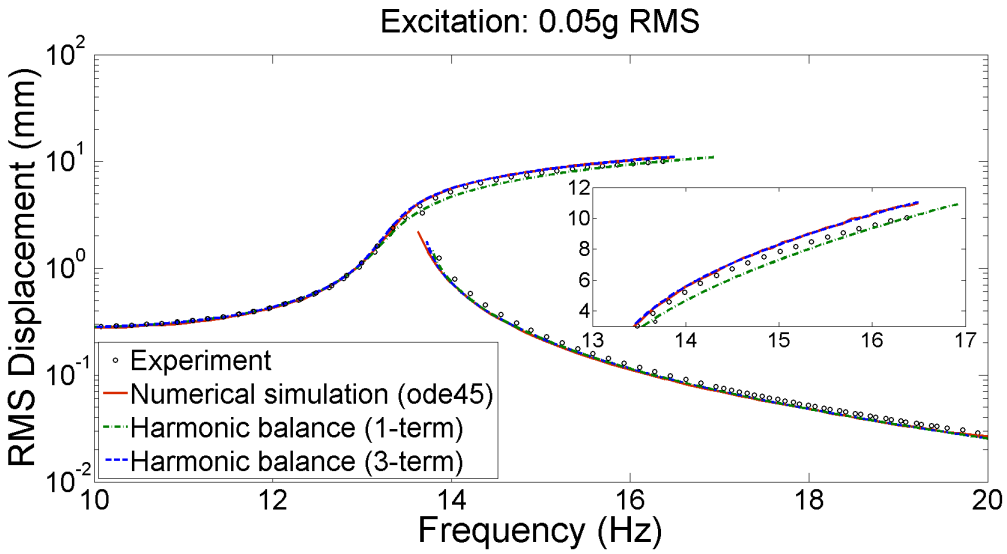

Figure 12: Displacement frequency response curves of the M-shaped oscillator at $0.05g$ RMS base acceleration level for up and down sweep: Experimental measurement, time-domain numerical simulation, and harmonic balance solutions (1-term and 3-term).

at which the bifurcation in the upper branch occurs as compared to the 1-term harmonic balance solution.

Overall, the experimental and simulated data are observed to be in very close agreement. The $0.03g$ and $0.05g$ cases show agreement at all frequencies, while the $0.07g$ case shows a discrepancy between the magnitude and frequency of the top of the upper branch. The simulation predicts a maximum RMS amplitude of 12.8 mm at a frequency of 17.5 Hz. The experimental values are 12.1 mm at 18.1 Hz. Increasing the value of γ would reduce the error of the maximum amplitude, but would increase the error of the maximum amplitude frequency. The value of 1 s/m is deemed acceptable for this model for all excitation levels covered in this work.

Experimental evidence of high bandwidth behavior at remarkably low excitation amplitudes is of particular interest. Studies involving the nonlinear vibrations of magnetoelastic oscillators showed only very slight nonlinear behavior at excitation levels around $0.1g$ and required levels of 0.3-$0.5g$ to display pronounced nonlinear behavior [92, 93, 94, 31, 33]. The M-shaped oscillator presented here suggests substantial reduction in the required excitation

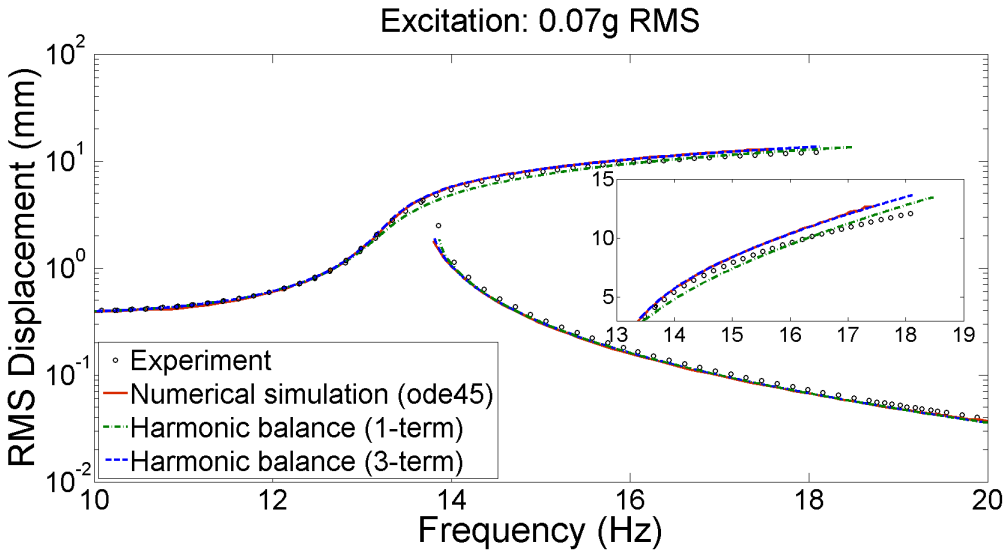

Figure 13: Displacement frequency response curves of the M-shaped oscillator at $0.07g$ RMS base acceleration level for up and down sweep: Experimental measurement, time-domain numerical simulation, and harmonic balance solutions (1-term and 3-term).

level from magnetoelastic oscillators by an order of magnitude. Additionally, the configuration presented in this work exhibits the desired broadband behavior due to a simpler arrangement of components without any magnetoelastic restoring force.

2.5.2 Effects of the Static Component and Higher Harmonics

Further details regarding the effect of higher harmonics are discussed next, focusing on different kinematic forms of the response. Electromechanical coupling is more closely related to velocity than displacement in basic energy harvesting techniques [34, 30] (e.g. piezoelectric transduction and electromagnetic induction). Figure 14 displays the contributions of the different harmonics to the displacement, velocity, and acceleration responses at the $0.07g$ RMS base acceleration level. For the M-shaped oscillator explored in this work, the nonlinearities are related to either displacement or velocity according to Equation 1; and as shown in Figure 14, the first harmonic dominates all other components of the displacement and velocity responses by at least an order of magnitude. The small magnitude of the DC component of the displacement as well as the higher harmonics does not, however, mean that they can be ignored in harmonic balance analysis. These different harmonics are

coupled in Equations 15-21, and ignoring seemingly insignificant higher harmonics in the response can lead to considerable errors in the prediction of important characteristics of the system, such as the frequency and magnitude of the response at the saddle-node bifurcation point in the upper branch.

Additionally, since the structure is intended for vibrational energy harvesting, the inclusion of higher harmonics may be even more important. Compared with the relative contribution of the different harmonics to displacement, the contribution of each successive harmonic to the velocity increases linearly with harmonic number. For energy harvesting systems, velocity is the variable that couples the electrical and mechanical domains, e.g. due to linear piezoelectricity and Faraday's law of induction, making higher harmonics very significant, as demonstrated next.

2.5.3 Case Study for Electromagnetic Energy Harvesting

In order to demonstrate the potential of the M-shaped configuration for broadband electrical power generation, and to illustrate the effects of higher harmonics in the power output, consider an electromagnetic energy harvesting implementation for the case of negligible coil inductance and linear electromechanical coupling as in Mann and Sims [61]. Zero internal (coil) resistance is assumed for simplicity. The governing electromechanical equations are then

$$m\ddot{z} + 2m\zeta\omega_n \left(1 + \gamma \left|\dot{z}\right|\right) \dot{z} + k_1 z + k_2 z^2 + k_3 z^3 - \theta i = -m'\ddot{y} \tag{30}$$

$$R_l i + \theta \dot{z} = 0 \tag{31}$$

where i is the electric current, θ is the electromechanical coupling, and R_l is the electrical load resistance. Equations 30 and 31 can then be combined to give

$$m\ddot{z} + \left(c_m + c_e\right) \dot{z} + k_1 z + k_2 z^2 + k_3 z^3 = -m'\ddot{y} \tag{32}$$

Here, c_m is the mechanical viscous damping coefficient including the equivalent quadratic damping according to Equation 10,

$$c_m = 2\zeta\omega_n m \left(1 + \gamma \frac{8\Omega Z_1}{3\pi}\right) \tag{33}$$

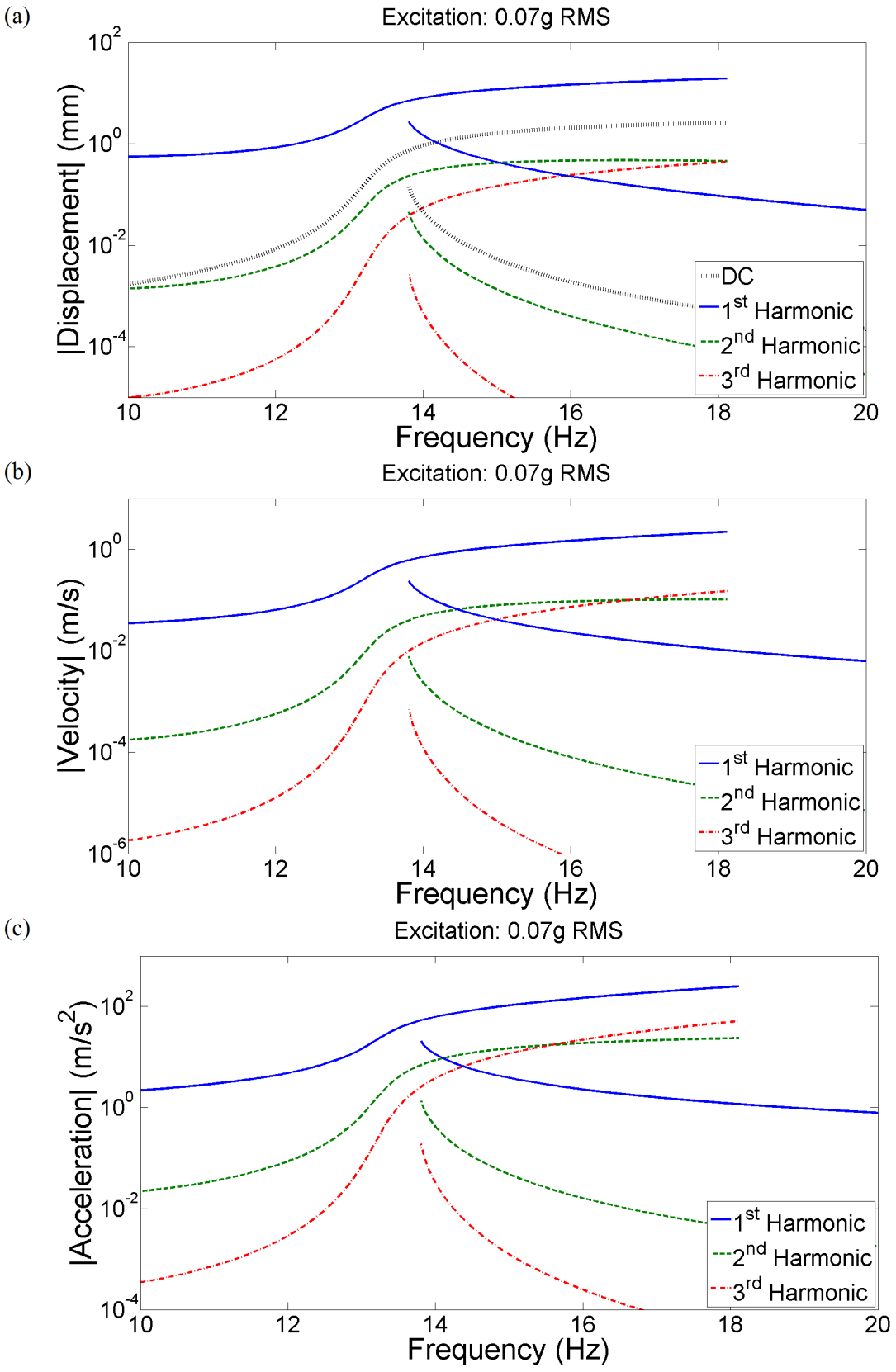

Figure 14: Magnitudes of the harmonic balance terms versus frequency for different kinematic forms of the response: (a) displacement; (b) velocity; (c) acceleration.

while c_e is the electrical damping coefficient,

$$c_e = \frac{\theta^2}{R_l} \tag{34}$$

The average electrical power output is calculated using

$$\bar{P} = i_{RMS}^2 R_l = \left(\frac{\theta \dot{z}_{RMS}}{R_l}\right)^2 R_l = c_e \dot{z}_{RMS}^2 \tag{35}$$

which can be analyzed for a range of c_e values by using multi-term and single-term harmonic balance expressions for the vibration response given by Equations 8 and 26, respectively. The only modification required in the harmonic balance analysis of Section 2.4 is to update the damping coefficient given by Equation 10 to account for the electrical damping:

$$c = c_m + c_e = 2\zeta\omega_n m \left(1 + \gamma \frac{8\Omega Z_1}{3\pi}\right) + \frac{\theta^2}{R_l} \tag{36}$$

For instance, the single-term solution for the average electrical power is

$$\bar{P} = \frac{1}{2} c_e \Omega^2 Z_1^2 \tag{37}$$

where Z_1 is obtained from

$$\left(k_1 Z_1 - m\Omega^2 Z_1 + \frac{3}{4} k_3 Z^3\right)^2 + \left[\left(c_m + c_e\right) \Omega Z_1\right]^2 = (mA)^2 \tag{38}$$

For a set of electrical damping coefficient values in the range of $0 < \frac{c_e}{c_m} < 2$, average power output frequency response curves are plotted based on the 3-term harmonic balance solution in Figure 15(a) for $0.07g$ RMS base excitation. The two-dimensional view of the average power frequency response curves in Figure 15(b) reveals that the maximum power output corresponds to the case of $c_e = c_m$ as in linear electromagnetic energy harvesters (with linear electromechanical coupling) in the absence of internal load resistance [95]. More importantly, Figure 15(b) clearly shows that the frequency bandwidth of large amplitude response shrinks monotonically with increased electrical damping. Wide bandwidths correspond to low values of electrical damping ($0 < \frac{c_e}{c_m} < 1$); however, low values of $\frac{c_e}{c_m}$ are associated with low power output as the fundamental trade-off. The maximum power output is obtained for $c_e = c_m$ with reduced bandwidth as compared to the cases of $0 < \frac{c_e}{c_m} < 1$. Further increase in the electrical damping to the range of $\frac{c_e}{c_m} > 1$ results in both reduced

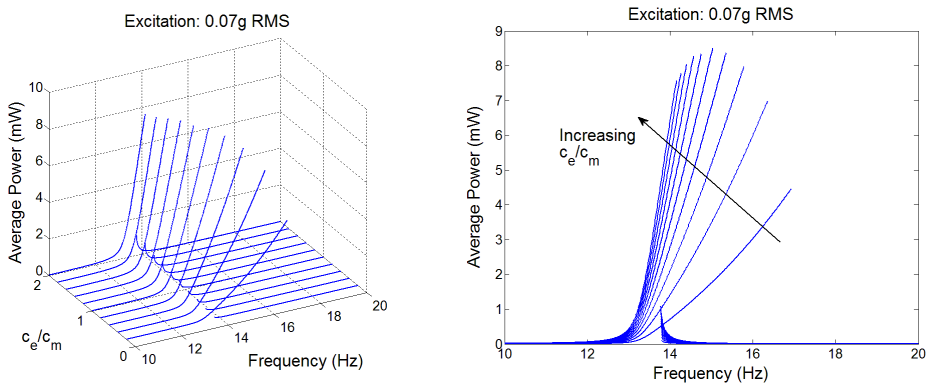

Figure 15: Average electrical power output frequency response curves for different values of the normalized electrical damping coefficient c_e/c_m: (a) 3-D view of power output versus frequency and normalized electrical damping and (b) 2-D view to visualize the maximum power case that corresponds to $c_e = c_m$ and the monotonic shortening of the frequency bandwidth of large-amplitude branch with increased electrical damping. RMS base acceleration is $0.07g$.

power output and reduced frequency bandwidth, gradually eliminating the advantages of the nonlinear M-shaped design over is linear counterpart.

Finally, the comparison of 1-term and 3-term solutions of the power frequency response curves for the case of $c_e = c_m$ is given in Figure 16. Recall from the previous graphs (Section 2.5.1) that the 3-term solution agrees very well with the time-domain numerical solution. As can be seen from this figure, in agreement with the discussion given in Section 2.5.2, the harvested power can be very sensitive to higher harmonics of the M-shaped oscillator. The upper saddle-node bifurcation point is predicted by the 1-term harmonic balance solution as 15.42 Hz, overestimating the 3-term solution of 15.04 Hz. Therefore the electrical power predictions of the 1-term harmonic balance solution between these two frequencies would be off by several orders of magnitude (since only the lower branch exists in the more accurate 3-term solution between 15.04 Hz and 15.42 Hz). The large-amplitude branch of the 3-term harmonic balance solution lies in the frequency range of 13.78 Hz to 15.04 Hz. In this frequency range, the 1-term solution underestimates the power output by more than 20%. For instance, the errors in the 1-term solution relative to 3-term solution at the frequencies of 14 Hz, 14.5 Hz, and 15 Hz are 29%, 25%, and 21%, respectively. Clearly the M-shaped energy harvester requires multi-term harmonic balance analysis for the accurate

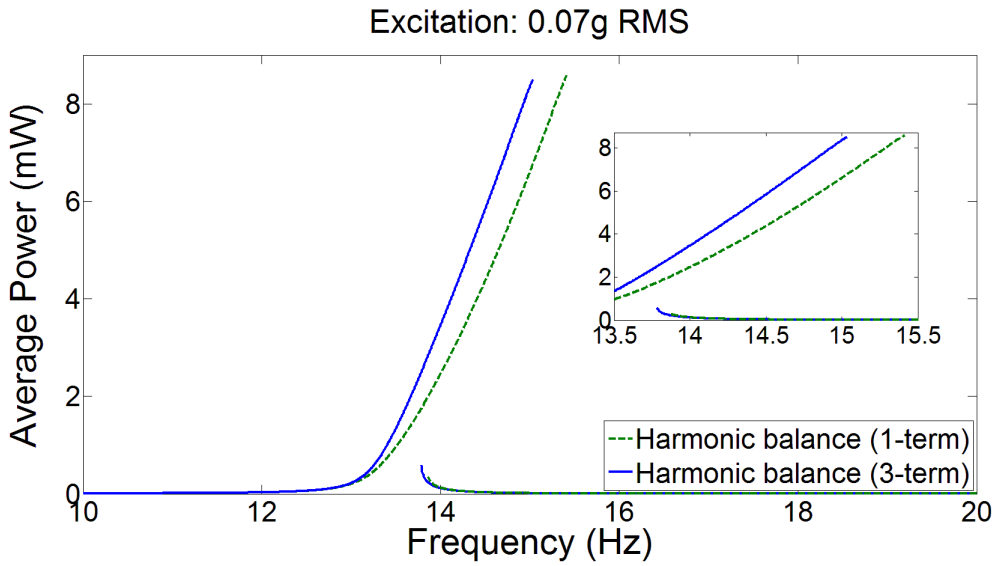

Figure 16: Comparison of average electrical power output frequency response curves obtained from the 1-term and 3-term harmonic balance solutions for $0.07g$ RMS base acceleration amplitude.

representation of its dynamics and prediction of the harvested power output.

2.6 Conclusion

An M-shaped bent beam with clamped end conditions is investigated theoretically and experimentally for bandwidth enhancement in vibration energy harvesting from base excitation. The proposed M-shaped oscillator made of spring steel is simpler to fabricate as it does not require extra discrete components to assemble. Furthermore the asymmetric nonlinear behavior of this configuration can easily be pronounced to yield broadband behavior under low excitation levels. Linear and nonlinear system parameters extracted from experiments are used to develop a lumped-parameter mathematical model. A quadratic damping term is included in the model and observed to be sufficient in order to account for nonlinear dissipative effects. In the absence of such a nonlinear dissipative term, the model tends to overestimate the frequency and amplitude of the upper saddle-node bifurcation point. A multi-term harmonic balance solution is developed to study the effects of higher harmonics and a constant term. Additionally, a single-term closed-form frequency response equation is also extracted and compared with the multi-term harmonic balance solution. Specifically, it

is observed that the single-term solution overestimates the frequency of upper saddle-node bifurcation point and underestimates the response amplitude in the large response branch. Multi-term harmonic balance solutions can be as accurate as time-domain solutions, and offer the advantage of substantially reduced computation time. Overall, very good agreement is observed between the model predictions and experimental measurements of the nonlinear frequency response under different base excitation levels. Substantial bandwidth enhancement with increasing base excitation is validated experimentally, analytically, and numerically. As compared to the 3dB bandwidth of the corresponding linear system (with the same damping linear ratio), the M-shaped oscillator offers 3200%, 5600%, and 8900% bandwidth enhancement at the root-mean-square base excitation levels of $0.03g$, $0.05g$, and $0.07g$, respectively. A case study is also given for electromagnetic energy harvesting, revealing the importance of higher harmonics and the need for multi-term harmonic balance analysis for predicting the power output accurately. Due to the existence of multiple regions of large strain and kinetic energy, the M-shaped oscillator can be conveniently employed in piezoelectric and electromagnetic energy harvesting as well as hybrid combinations thereof.

Chapter III

AN M-SHAPED PIEZOELECTRIC ENERGY HARVESTER

3.1 Introduction

It has been well demonstrated over the past few years that vibration energy harvesters with intentionally designed nonlinear stiffness components can be used for frequency bandwidth enhancement under harmonic excitation for sufficiently high vibration amplitudes. In order to overcome the need for high excitation intensities that are required to exploit nonlinear dynamic phenomena, an M-shaped piezoelectric energy harvester configuration has been developed that can exhibit a nonlinear frequency response under very low vibration levels. Chapter 2 focuses on purely mechanical (structural) dynamics of this configuration. It was found that broadband energy harvesting can be achieved for excitations below $0.1g$ base acceleration. In this chapter, the author introduces an M-shaped piezoelectric energy harvester prototype, presents its empirical mathematical model, and investigates its linear and nonlinear electromechanical dynamics by rigorous experiments and high-fidelity modeling using the method of harmonic balance with multiple terms. Both primary resonance and secondary resonance (for superharmonic response) behaviors, as well as multi-harmonic excitation, are modeled and experimentally validated.

3.2 Nonlinear Piezoelectric Energy Harvester, Mathematical Description, and Analysis

3.2.1 M-shaped Piezoelectric Energy Harvester

3-D model and photographic views of the nonlinear M-shaped piezoelectric energy harvester prototype explored in this work are shown in Figure 17 along with its clamp and shaker mount. While this device can be fabricated at different geometric scales, the M-shaped energy harvester analyzed in this work consists of a flexible beam made from 25.4 mm wide by 0.254 mm thick AISI 1075 spring steel and is approximately 20 cm long. The steel is cut and bent using common sheet metal tools. The bend angles used are small enough to allow near

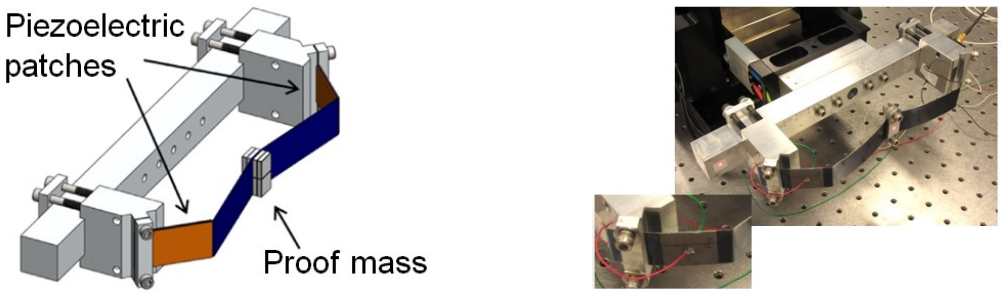

(a) (b)

Figure 17: (a) 3-D model and (b) photographs of the nonlinear M-shaped piezoelectric energy harvester prototype along with its clamp and shaker mount. Close-up picture shows one of the four piezoelectric patches, which form two bimorphs.

zero radius bends without first heating the metal. The lumped mass attachment consists of pieces of stainless steel, bolted together sandwiching the center of the beam. Both ends of the bent beam are clamped. The clamp and shaker mount are made from 6061 aluminum. Electromechanical coupling is due to four piezoelectric patches bonded near the clamps (resulting in two bimorphs bracketing the continuous spring steel substrate). Dynamic bending of the spring causes tensile and compressive strains on the piezoelectric layers, yielding an alternating voltage via the direct piezoelectric effect, which is then connected to an electrical load for AC power generation (or it can be rectified and conditioned in an energy harvesting circuit to obtain a stable DC signal for charging a storage component). In the present effort, focus is placed on the analyzing the AC power generation characteristics and harmonic balance analysis of this nonlinear piezoelectric energy harvester when excited near its primary or secondary (superharmonic) resonance frequencies.

3.2.2 Governing Electromechanical Equations

The M-shaped energy harvester is modeled as a single-degree-of-freedom system undergoing base excitation with linear viscous and quadratic damping terms, a nonlinear elastic restoring force, and linear electromechanical coupling (Figure 18). The locations of the piezoelectric patches in Figure 17(b) are chosen to reduce piezoelectric softening nonlinearity[54] and best exploit the geometric hardening nonlinearity of the M-shaped design. [1] The force

[1]Piezoelectric material nonlinearity in energy harvesting is manifested in the form of ferroelastic softening (of quadratic order from the dynamical system standpoint according to our recent work [54], see Chapter

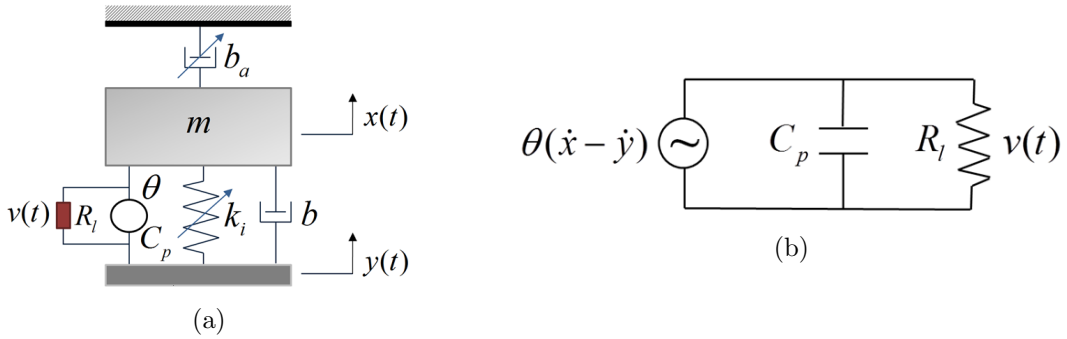

Figure 18: (a) Lumped-parameter electromechanical model and (b) equivalent circuit model with a dependent current source and linear electromechanical coupling.

balance and current balance equations are then

$$m\ddot{z} + b\dot{z} + b_a|\dot{x}|\dot{x} + F_s(z) - \theta v = -\bar{m}\ddot{y} \tag{39}$$

$$C_p\dot{v} + \frac{1}{R_l}v + \theta\dot{z} = 0 \tag{40}$$

where m is the equivalent mass of the device, $\bar{m}$ is the effective mass that causes the forcing term due to base excitation ($\bar{m} \approx m$ if the lumped mass dominates the mass of the rest of the structure), b is the linear viscous damping coefficient, b_a is the quadratic (velocity-squared) damping coefficient (typically attributed to fluid-structure interaction), $F_s(z)$ is the nonlinear elastic restoring force, $y(t)$ is the base displacement measured in an inertial frame, $z(t)$ is the displacement of the oscillator relative to the moving base, $x(t)$ is the displacement of the mass relative to the fixed reference frame (i.e. $x(t) = y(t) + z(t)$), and an overdot represents differentiation with respect to time.

3.2.3 General Multi-Term Harmonic Balance Formulation

The second-order force balance equation with nonlinear terms and linear current balance equation given by equations (1) and (2) can be expressed in the form of three first-order equations for time-domain numerical simulations (e.g. by using ode45 in MATLAB). However, the process of numerical simulation in time domain can be computationally lengthy (especially to reach steady state in high-quality-factor systems), and it offers little or no

4), which would inherently eliminate significant part of geometric hardening bandwidth (before it appears) in the case tightly clamped piezoelectrics at the roots. Therefore piezoelectric patches are deliberately located slightly outside the clamps to reduce the strain in piezoelectrics. This is a tradeoff between the peak power output and the frequency bandwidth, and clearly the effort presented here is concerned with the latter.

insight into the underlying mathematics of the problem. Among the methods of approximate analytical solutions for nonlinear differential equations, the method of harmonic balance[71, 53, 51] is preferred in this work, since the system studied here exhibits a high degree of nonlinearity (strong nonlinearity) and therefore it is required to explore multi-harmonic solutions for enhanced accuracy[53]. In the following, first the multi-harmonic solution is given by accounting for higher harmonics and a DC (constant) component prior to demonstrating the solution process for the case of a single harmonic.

The base excitation term is assumed to be harmonic of the form:

$$\ddot{y}(t) = A\cos(\Omega t) \tag{41}$$

where A is the base acceleration amplitude and Ω is the driving frequency. It is useful to write the governing in state-space form:

$$\begin{aligned} x_1 &= z \\ x_2 &= \dot{z} \\ x_3 &= v \end{aligned} \tag{42}$$

The governing equations then become the first order system of ordinary differential equations:

$$\begin{aligned} \dot{x}_1 &= x_2 \\ \dot{x}_2 &= \frac{1}{m}\left[-bx_2 - b_a\left|x_2 + \frac{A}{\Omega}\sin(\Omega t)\right|\left(x_2 + \frac{A}{\Omega}\sin(\Omega t)\right) - F_s(x_1) + \theta x_3 - \bar{m}A\cos(\Omega t)\right] \\ \dot{x}_3 &= \frac{-1}{C_p}\left(\frac{1}{R_l}x_3 + \theta x_2\right) \end{aligned} \tag{43}$$

which can be written in vector form:

$$\dot{\vec{x}} = \vec{f}(t, \vec{x}) = \vec{f}(t + T, \vec{x}) \tag{44}$$

This system with explicit time dependence is periodic in time with period $T = 2\pi/\Omega$. A truncated Fourier series solution with N harmonics and the same period is assumed for solution:

$$\vec{x}(t) = \vec{a} + \mathbf{A}\vec{c}(t) + \mathbf{B}\vec{s}(t) \tag{45}$$

where $\vec{a}$ is a constant vector representing the DC components of the response, $\mathbf{A}$ and $\mathbf{B}$ are constant 3xN rectangular matrices containing the cosine and sine coefficients, while $\vec{c}(t)$ and $\vec{s}(t)$ are vectors of cosine and sine functions defined as

$$\begin{aligned} c_n(t) &= \cos(n\Omega t) \\ s_n(t) &= \sin(n\Omega t) \end{aligned} \tag{46}$$

With the chosen approximate solution, the residual function is

$$\vec{r}(t) = \vec{f}(t, \vec{x}(t)) - \dot{\vec{x}}(t) \tag{47}$$

In order to find the unknowns $\vec{a}$, $\mathbf{A}$, and $\mathbf{B}$ the residual function is minimized in the Galerkin method sense such that

$$\begin{aligned} \int_0^{2\pi/\Omega} \vec{r}(t)dt &= 0 \\ \int_0^{2\pi/\Omega} \vec{r}(t)\vec{c}^T(t)dt &= 0 \\ \int_0^{2\pi/\Omega} \vec{r}(t)\vec{s}^T(t)dt &= 0 \end{aligned} \tag{48}$$

This yields $3(2N+1)$ equations for the same number of unknowns. This nonlinear system of algebraic equations can be solved in a number of ways, one of the best being the Newton-Raphson method.

3.2.4 Single-Harmonic Formulation and Frequency Response Equations

While the main advantage of harmonic balance analysis is the ease of including higher harmonics in a systematic way, consider the simplest solution using only the constant term and first frequency component, i.e. N = 1, in order to illustrate the solution process. The assumed solutions for the relative displacement, relative velocity, and electrode voltages are

$$z(t) = x_1(t) = a_1 + A_{11}\cos(\Omega t) + B_{11}\sin(\Omega t) \tag{49}$$

$$\dot{z}(t) = x_2(t) = a_2 + A_{21}\cos(\Omega t) + B_{21}\sin(\Omega t) \tag{50}$$

$$v(t) = x_3(t) = a_3 + A_{31}\cos(\Omega t) + B_{31}\sin(\Omega t) \tag{51}$$

which yield the following residual functions:

$$r_1(t) = a_2 + A_{21}\cos(\Omega t) + B_{21}\sin(\Omega t) + A_{11}\Omega\sin(\Omega t) - B_{11}\Omega\cos(\Omega t) \tag{52}$$

$$\begin{aligned} r_2(t) = {} & m\Omega\left[-A_{21}sin(\Omega t) + B_{21}cos(\Omega t)\right] + b\left[a_2 + A_{21}\cos(\Omega t) + B_{21}\sin(\Omega t)\right] \\ & + b_a\left|a_2 + A_{21}\cos(\Omega t) + \left(B_{21} + \frac{A}{\Omega}\right)\sin(\Omega t)\right| \\ & \quad \times \left[a_2 + A_{21}\cos(\Omega t) + \left(B_{21} + \frac{A}{\Omega}\right)\sin(\Omega t)\right] \\ & + k_1(a_1 + A_{11}\cos(\Omega t) + B_{11}\sin(\Omega t)) + k_2[a_1 + A_{11}\cos(\Omega t) + B_{11}\sin(\Omega t)]^2 \\ & + k_3[a_1 + A_{11}\cos(\Omega t) + B_{11}\sin(\Omega t)]^3 + k_4[a_1 + A_{11}\cos(\Omega t) + B_{11}\sin(\Omega t)]^4 \\ & + k_5[a_1 + A_{11}\cos(\Omega t) + B_{11}\sin(\Omega t)]^5 - \theta\left[a_3 + A_{31}\cos(\Omega t) + B_{31}\sin(\Omega t)\right] \\ & + \bar{m}A\cos(\Omega t) \end{aligned} \tag{53}$$

$$\begin{aligned} r_3(t) = {} & C_p\Omega\left[-A_{31}\sin(\Omega t) + B_{31}\cos(\Omega t)\right] + \frac{1}{R_l}\left[a_3 + A_{31}\cos(\Omega t) + B_{31}\sin(\Omega t)\right] \\ & + \theta\left[a_2 + A_{21}\cos(\Omega t) + B_{21}\sin(\Omega t)\right] \end{aligned} \tag{54}$$

Minimizing the residual functions in the Galerkin sense (equations (10)) means finding the unknowns (elements of $\vec{a}$, $\mathbf{A}$, and $\mathbf{B}$) such that each of the residual functions is orthogonal to each of the basis functions: 1, $\cos(\Omega t)$, and $\sin(\Omega t)$ in this particular case of $N = 1$. Carrying out the required integrations yields the following system of 9 nonlinear algebraic equations for the 9 unknown Fourier coefficients in equations (11)-(13):

$$a_2 = 0 \tag{55}$$

$$A_{21} - \Omega B_{11} = 0 \tag{56}$$

$$B_{21} + \Omega A_{11} = 0 \tag{57}$$

$$\begin{aligned} & 3k_3a_1A_{11}^2 + 3k_3a_1B_{11}^2 + 6k_4a_1^2A_{11}^2 + 6k_4a_1^2B_{11}^2 + \frac{3}{2}k_4A_{11}^2B_{11}^2 + 10k_5a_1^3A_{11}^2 + 10k_5a_1^3B_{11}^2 \\ & + \frac{15}{4}k_5a_1A_{11}^4 + \frac{15}{4}k_5a_1B_{11}^4 + k_2A_{11}^2 + k_2B_{11}^2 + 2k_3a_1^3 + \frac{3}{4}k_4A_{11}^4 + \frac{3}{4}k_4B_{11}^4 \\ & + 2k_4a_1^4 + 2k_5a_1^5 - 2\theta a_3 + 2b_{eq}a_2 + 2k_1a_1 + 2k_2a_1^2 + \frac{15}{2}k_5a_1A_{11}^2B_{11}^2 = 0 \end{aligned} \tag{58}$$

$$\frac{3}{4}k_3A_{11}^3 + \bar{m}A + \frac{5}{8}k_5A_{11}^5 + b_{eq}A_{21} + k_1A_{11} - \theta A_{31} + 3k_4a_1A_{11}B_{11}^2 + \frac{15}{2}k_5a_1^2A_{11}B_{11}^2 + \frac{5}{8}k_5A_{11}B_{11}^4 + \frac{15}{2}k_5a_1^2A_{11}^3 + 4k_4a_1^3A_{11} + 3k_4a_1A_{11}^3 + 5k_5a_1^4A_{11} + m\Omega B_{21} + 2k_2a_1A_{11} + 3k_4a_1^2A_{11} + \frac{5}{4}k_5A_{11}^3B_{11}^2 + \frac{3}{4}k_3A_{11}B_{11}^2 = 0 \tag{59}$$

$$-m\Omega A_{21} + 4k_4a_1^3B_{11} + 5k_5a_1^4B_{11} + 2k_2a_1B_{11} + 3k_3a_1^2B_{11} + \frac{5}{8}k_5A_{11}^4B_{11} + \frac{3}{4}k_3A_{11}^2B_{11} + \frac{5}{4}k_5A_{11}^2B_{11}^3 + 3k_4a_1B_{11}^3 + \frac{15}{2}k_5a_1^2B_{11}^3 + b_{eq}B_{21} + k_1B_{11} + \frac{5}{8}k_5B_{11}^5 + \frac{3}{4}k_3B_{11}^3 - \theta B_{31} + 3k_4a_1A_{11}^2B_{11} + \frac{15}{2}k_5a_1^2A_{11}^2B_{11} = 0 \tag{60}$$

$$\theta a_2 + \frac{1}{R_l}a_3 = 0 \tag{61}$$

$$C_p\Omega B_{31} + \frac{1}{R_l}A_{31} + \theta A_{21} = 0 \tag{62}$$

$$C_p\Omega A_{31} - \frac{1}{R_l}B_{31} - \theta B_{21} = 0 \tag{63}$$

where the first three equations confirm the expected relationship between z and $\dot{z}$. In these equations the dissipative terms have been combined by defining an equivalent viscous damping coefficient, b_eq, as

$$b_{eq} = b + \frac{8}{3\pi}b_a\sqrt{A_{21}^2 + B_{21}^2} \tag{64}$$

This is a very good approximation when the base velocity ($\dot{y}$) is small compared to the relative velocity ($\dot{z}$). This approximation is necessary, as integrating the quadratic dissipation term in closed form is impossible for general harmonic balance solutions with N harmonics. As is apparent, this system of equations is not solvable directly, and a numerical method such as Newton-Raphson is required to solve them. The difficulty of generating the system of algebraic equations in closed form and the necessity of solving them numerically make it evident that, in practice, it is better to numerically generate and solve the system of nonlinear equations for harmonic balance analyses from the outset.

It is worth mentioning the approach used in the computational algorithm to obtain the harmonic balance analysis results presented in this work. A general harmonic balance solver is written to solve any system that can be written in the form of equation (6), which might include other nonlinearities (e.g. inertial[96], piezoelectric[54], and even circuit[43]

nonlinearities). Since the integrations in equation (10) (and associated integrations to find elements of the Jacobian necessary for the Newton-Raphson method) are equivalent to finding Fourier series components, the algorithm's speed is significantly increased using FFT (Fast Fourier Transform) algorithms. In this way, harmonic balance analyses to find periodic solutions to high order/dimension systems can be completed orders of magnitude faster than time domain simulations, even while keeping many more harmonic components than is feasible with perturbation methods such as the LindstedtPoincar method or the method of multiple scales[72]. The benefits over time domain simulation are especially apparent for high-quality-factor systems, where much computation time can be wasted simulating transients. Also by including the appropriate harmonics and choosing the correct driving frequency range, it is simple to use the method of harmonic balance to analyze secondary and combination resonances in addition to the primary resonance of a nonlinear oscillatory system.

3.2.5 Multi-Harmonic Excitation

Another advantage of the method of harmonic balance is the ease with which the analysis may be extended to include excitation from an arbitrary periodic source rather than a pure sinusoid. From the experimental standpoint, providing an ideal single frequency base acceleration is impossible, and in some circumstances, the contribution of harmonic distortion in the excitation to the response may not be negligible (which might yield misleading experimental results). For example, an ideal experiment to observe a quadratic superharmonic resonance would involve a single frequency excitation at $\Omega \approx \omega_n/2$, where ω_n is the linear natural frequency of the system. If a quadratic nonlinearity is present, a response at ω_n would be generated and then dynamically amplified, dominating the subresonant quasi-linear response at Ω. However, suppose the excitation (base acceleration) is not a pure sinusoid and instead is a general periodic function with form:

$$\ddot{y}(t) = p_0 + \sum_{n=1}^{\infty} p_n \cos(n\Omega t + \phi_n) \tag{65}$$

In this case, the response at ω_n is due to both the quadratic nonlinearity as well as forcing at the natural frequency directly from the term with coefficient p_2. Experimentally, it is

impossible to separate the superharmonic resonant response to the fundamental frequency of excitation signal from the quasi-linear resonant response due to higher harmonics of the excitation signal. Therefore it is useful to be able to simulate response to multi-harmonic excitation to validate experiments and analyze differences between ideal experimental conditions and more realistic ones. Not to mention there might be practical scenarios of energy harvesting in which the ambient excitation form is indeed general periodic rather than simple harmonic.

3.3 Experimental Results and Model Validation

3.3.1 Experimental Procedure

In order to analyze the primary and secondary (superharmonic) resonance energy harvesting performance of the device, as well as identify model parameters to simulate the system as previously discussed, a series of experiments are conducted. A static force-displacement test is completed to identify the nonlinear restoring force, F_s. Low amplitude linear regime energy harvesting tests are conducted to extract the equivalent mass, linear damping, and electromechanical coupling parameters. Finally nonlinear frequency sweep energy harvesting tests are reported for both primary and secondary (superharmonic) resonance excitation to evaluate the performance of the M-shaped energy harvester and the fidelity of the nonlinear electromechanical model and harmonic balance based analysis method. Multi-harmonic excitation (as a part of secondary resonance excitation for superharmonic response) is also demonstrated and validated as an application of the model presented here.

3.3.2 Experimental Setup for Nonlinear Dynamic Analysis

An overview picture of the experimental setup is shown in Figure 19 along with a close up view of the M-shaped piezoelectric energy harvester. Experiments are performed using an APS-113 seismic shaker driven by an APS-125 amplifier and controlled by a SPEKTRA VCS-201 controller. These devices allow for the sample to be subjected to harmonic base acceleration at specified amplitudes and frequencies. Tests consist of up and down frequency sweeps at a constant kinematic variable (in this case base acceleration amplitude) necessary for frequency response analysis of the nonlinear system. Base acceleration measured by a

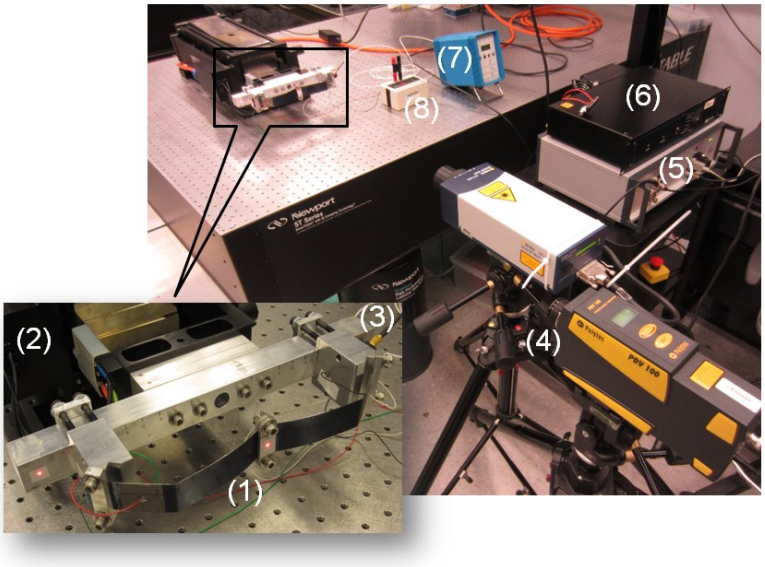

Figure 19: Experimental setup: (1) M-shaped nonlinear piezoelectric energy harvester; (2) vibration exciter (electrodynamic shaker); (3) accelerometer; (4) laser Doppler vibrometers; (5) vibration control unit (using base acceleration as the feedback signal); (6) power amplifier; (7) signal conditioner; and (8) resistance substitution box.

Kistler model 8636C50 ICP accelerometer is used for feedback to the VCS-201 controller. A Polytec PDV-100 Portable Digital Vibrometer is used to measure the base velocity. The velocity of the lumped mass (i.e. center of the M-shaped oscillator) is measured using a Polytec OFV-505 sensor head and OFV-5000 controller. Current output from the piezoelectric elements is shunted through a variable resistance box (IET Labs, Inc., RS-201W), the voltage across which is measured. A National Instruments NI USB-4431 unit is employed for data acquisition.

3.3.3 Parameter Identification

In order to investigate the nonlinear system dynamics theoretically, it is necessary to identify the relevant parameters of the M-shaped energy harvester. First the relationship between deflection and restoring force (F_s) is extracted to empirically model the nonlinear stiffness behavior under short-circuit condition. To this end, the oscillator is bolted to the rigid optical table vertically (to set $y = 0$ so that $x = z$). The lumped mass attachment is removed (to avoid any sag due to gravity), and then weights are suspended from the center of the spring. Central deflection (z) is measured using the OFV-5000 displacement decoder

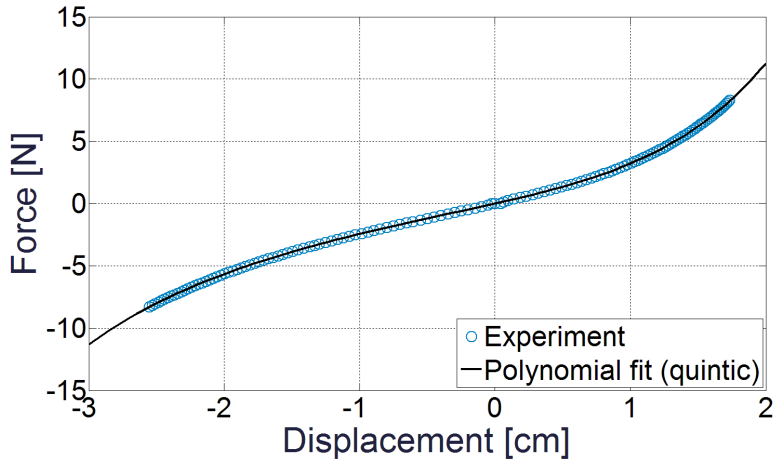

Figure 20: Experimental nonlinear static force vs. displacement data (under short-circuit condition for the piezoelectric patches) and a quintic polynomial curve fit.

of the laser vibrometer. The sample is turned over and the process repeated. It is assumed that the weight of the spring itself is negligible compared to the suspended weights. It is also assumed the removal of the mass attachments does not change the stiffness characteristics of the spring. The resulting force vs. displacement curve is plotted in Figure 20 along with a polynomial curve fit.

The following quintic (fifth-order) polynomial form is fit to the experimental nonlinear static force vs. displacement data:

$$F_s(z) = k_1 z + k_2 z^2 + k_3 z^3 + k_4 z^4 + k_5 z^5 \tag{66}$$

Here, the linear coefficient (k_1) can be interpreted as the linear spring stiffness for small displacements, while the higher order coefficients define the nonlinearity. Identified values of the stiffness coefficients are listed in Table 2. The values of the coefficients are displayed with respect to a cm length scale, as this is the order of magnitude of displacements during nonlinear testing (note that the model obviously uses consistent SI units that take the displacement in meters in calculations). It is apparent that the quadratic and cubic terms dominate the nonlinearity, and are relatively comparable to each other in strength. Specifically, if the displacement is $O(1)$ ("order 1" in cm-scale) the cubic nonlinearity dominates the nonlinear part and comparable contribution is also due to the quadratic nonlinearity (this $O(1)$ response physically happens for primary resonance excitation). On the other

Table 2: Identified nonlinear spring coefficients.

k_1 [N/cm]	k_2 [N/cm^2]	k_3 [N/cm^3]	k_4 [N/cm^4]	k_5 [N/cm^5]
2.441	0.268	0.363	0.103	0.021

Table 3: Identified lumped mass, dissipation, electromechanical coupling, and capacitance parameters.

m [g]	b [Ns/m]	b_a [Ns^2/m^2]	θ [N/V]	C_p [nF]
31.9	5.5×10^{-3}	1.2×10^{-2}	1.7×10^{-4}	34.27

hand, if the displacement response is $O(0.1)$ ("order 0.1" in cm-scale, or "order 1" in mm-scale which is expected to happen in secondary resonance excitation, e.g. superharmonic resonance), there is a predominant effect of quadratic nonlinearity, rather than cubic nonlinearity. This discussion will be revisited in the secondary resonance for superharmonic response section.

The equivalent mass, linear damping coefficient, and electromechanical coupling coefficients are obtained from linear energy harvesting resistor sweep experiments, and the harvester capacitance is measured directly. Note that the equivalent mass is simply $m = k_1/\omega_n^2$ (where ω_n is the short-circuit natural frequency). Linear viscous damping coefficient is simply $b = 2\zeta m\omega_n$, where the mechanical damping ratio (ζ) is identified from half-power points of the short-circuit vibration frequency response (it could as well be identified from free vibrations [53] under short-circuit condition by using the logarithmic decrement). Finally, the quadratic damping term, b_a, in Equation (1) is found to account for overestimates of peak response with linear damping alone. The physical justification of quadratic (or velocity-squared) dissipation is nonlinear fluid damping [68, 13] associated with drag force resulting from large amplitude vibration. These model parameters are summarized in Table 3.

3.3.4 Linear Frequency Response

The linear regime energy harvesting tests allow the measuring of the velocity, voltage, current, and power frequency response functions by means of white noise type random base excitation. For this system, white noise excitation is preferable to a chirp or sine sweep, because the threshold for nonlinear behavior is extremely low (which is the advantage of the configuration to exploit nonlinear broadband behavior for low excitation intensities),

on the order of 5×10^{-3} g RMS base acceleration. A finite set of resistive loads has to be used in the experiments and it is preferable to cover a broad range between the short-circuit ($R_l \to 0$) and open-circuit ($R_l \to \infty$) extremes. While the system is not too weakly coupled, $R_l \approx 1/\omega_n C_p$ can be used to estimate the optimal load resistance neighborhood as an approximation. For this system, $1/\omega_n C_p$ yields approximately 300kΩ, so the range of 30kΩ to 3MΩ is selected to include electrical boundary conditions ranging from nearly short circuit to nearly open circuit.

Figure 21 shows the velocity, voltage, current and power frequency response functions (FRFs) for the five chosen load resistances. Once again, to eliminate a strong piezoelectric softening nonlinearity[54], the level of piezoelectric coupling is designed to be relatively low by locating the piezoceramic patches outside the clamps, and therefore the short–circuit and open–circuit resonance frequencies are quite close, approximately 13.91 Hz and 13.94 Hz, respectively. In the linear regime, mechanical dissipation is extremely light, with a viscous damping ratio identified from the short-circuit voltage FRF of $\zeta \approx 0.001$. As anticipated, the 300kΩ load is a reasonable approximation to the optimal electrical load neighborhood, yielding a peak normalized power of approximately 5.4 W/g^2 (linear estimate). As the linear model parameters are extracted empirically, the model yields an excellent match in Figure 21. It should be noted that the linear system has very low bandwidth (0.05 Hz for 300kΩ load resistance). It is of interest how much this bandwidth increases with increased base acceleration levels, which is discussed next.

3.3.5 Nonlinear Frequency Response

The nonlinear energy harvesting experiments consist of controlled (i.e. constant base acceleration) up and down frequency sweeps to capture the jump phenomenon associated with saddle-node bifurcation[41, 70] that provides nonlinear bandwidth enhancement. Primary resonance tests refer to excitation frequencies that are near the linear natural frequency of the energy harvester, i.e. $\Omega \approx \omega_n$. In this work, secondary resonance behavior refers to excitation that is either one half or one third of the linear natural frequency (i.e. rather than subharmonic, focus is placed on these superharmonic resonances). In the case of the

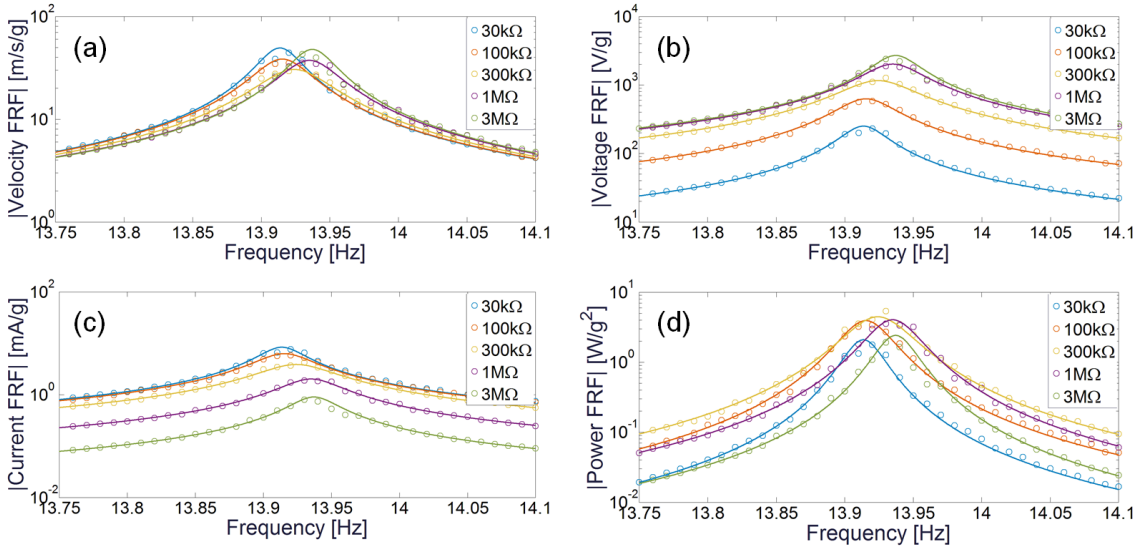

Figure 21: Linear electromechanical FRFs: (a) velocity, (b) voltage, (c) current, and (d) power output per base acceleration at various load resistance levels (obtained by very low intensity white noise excitation). Circles represent experimental data and solid curves represent model predictions.

one half secondary resonance, excitation at Ω will yield a response at $2\Omega \approx \omega_n$ that will resonate. Similarly, the one third secondary resonance would involve a response at $3\Omega \approx \omega_n$.

3.3.5.1 Primary Resonance

By using the feedback shaker system (Figure 19), up and down frequency sweep experiments are conducted at RMS (root-mean-square) base acceleration levels of $0.01g$, $0.02g$, $0.03g$, and $0.04g$. Only the results of the $0.04g$ experiments are shown in Figure 22 for brevity. There is a very good match between the model predicted behavior (5-term harmonic balance solution) and the experimental results at all studied base acceleration levels and load resistance values. The main discrepancy is that the model underestimates the response magnitude somewhat in every case. While both the nonlinear restoring force and dissipative forces play a role in this, even with no velocity squared dissipation ($b_a = 0$), the model still under predicts the response. Part of the error can be attributed to unmodeled inertial nonlinearity. Because the potential (and expectedly minor) ferroelastic (stress-strain) nonlinearity due to piezoelectric laminates would be captured within the force-displacement relationship, part of the unmodeled nonlinearity might be due to electromechanical coupling

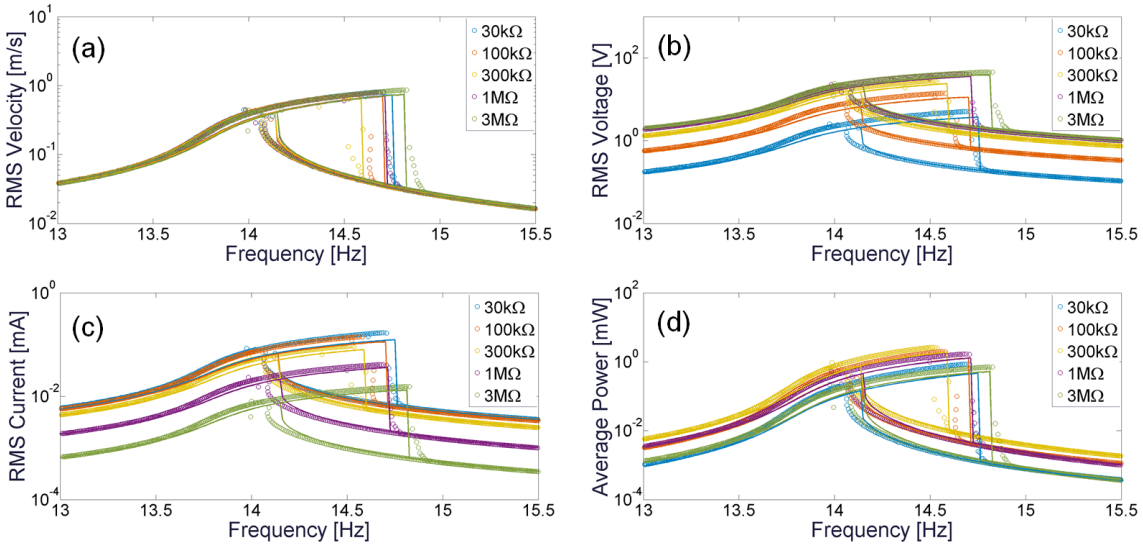

Figure 22: Nonlinear electromechanical frequency response curves in the neighborhood of primary resonance excitation ($\Omega \approx \omega_n$): (a) velocity, (b) voltage, (c) current, and (d) power output. Base acceleration amplitude is $0.04g$ RMS. Circles represent experimental data and solid curves represent model predictions.

[90] associated with increased forcing. The energy harvesting performance of the M-shaped device at near optimal load conditions and various base acceleration amplitudes is summarized in Table 4. Due to the dominant hardening nonlinearity and jump phenomenon, a saturation of the response amplitude and a widening of the response bandwidth are observed. Despite the aforementioned errors, the model shows the correct trends and provides very good predictions of harvester performance. For the largest excitation level studied in this work ($0.04g$ RMS case, i.e. Figure 22), the bandwidth of the system for 300kΩ load resistance is 0.38 Hz, which is 660% larger than the linear bandwidth (0.05 Hz) summarized in the previous section.

Note that the nonlinear frequency response bandwidth, Δf, is shorter for the optimal load case inevitably due to dissipation as a result of Joule heating in the resistor that is used to quantify the electrical power output. This phenomenon is inevitable in more complex nonlinear energy harvesting circuits[75, 47] as well (due to power transfer from the mechanical to electrical domain) and is the nonlinear counterpart of damping resulting from energy harvesting (see Lesieutre et al.[55] for its linear counterpart in the sense of classical shunt damping). As one moves away from the optimal electrical load condition,

Table 4: Summary of experimental results and model predictions at various base acceleration levels (load resistance: 300kΩ).

	g_{RMS}	0.01	0.02	0.03	0.04
$\dot{x}_{RMS}$ [mm/s]	Experiment	244	415	564	708
	Model	244	415	564	708
v_{RMS} [V]	Experiment	9.2	15.9	22.0	28.0
	Model	8.7	14.9	20.0	23.0
i_{RMS} [μA]	Experiment	9.2	15.9	22.0	28.0
	Model	8.7	14.9	20.0	23.0
P_{AVG} [mW]	Experiment	0.28	0.84	1.62	2.61
	Model	0.25	0.74	1.33	1.91
f_{peak} [Hz]	Experiment	14.00	14.13	14.31	14.51
	Model	14.01	14.20	14.40	14.59
Δf [Hz]	Experiment	0.12	0.18	0.27	0.38
	Model	0.08	0.19	0.28	0.37

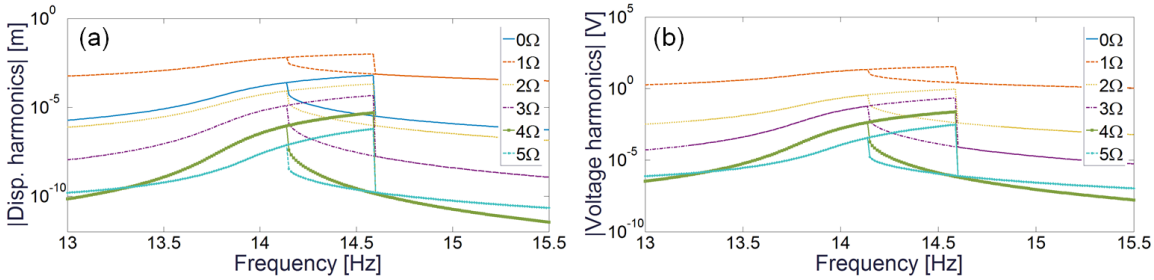

Figure 23: Harmonic content of (a) relative displacement and (b) voltage output obtained by model simulation for the neighborhood of primary resonance excitation ($\Omega \approx \omega_n$). The base acceleration amplitude is $0.04g$ RMS, and load resistance is 300kΩ.

the nonlinear bandwidth increases at the expense of reduced power output as a trade-off.

The individual harmonics contributing the relative displacement and voltage output frequency response functions in the 5–term ($N = 5$) harmonic balance solution are reported in Figure 23. Note that the voltage response has no DC (zero frequency) component whereas the DC component in the displacement response is the second major content in the frequency response after the first harmonic. Crossing of the curves at certain frequencies is also noteworthy. The effects of individual harmonics on the dynamics of the M-shaped oscillator is discussed in detail elsewhere[53]. Next the secondary resonance behavior is considered, specifically superharmonic response in the M-shaped piezoelectric energy harvester.

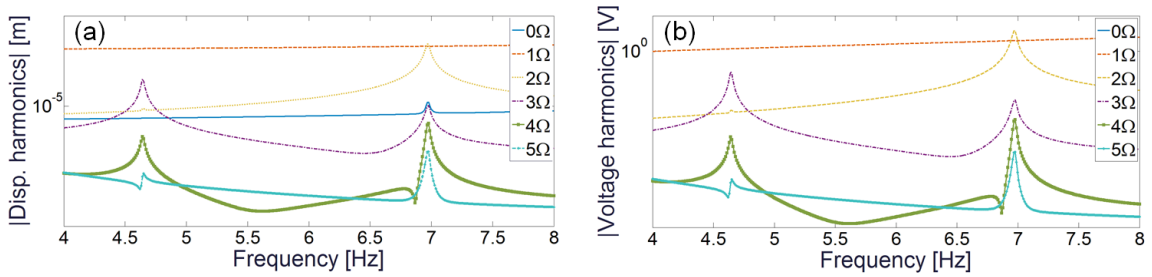

Figure 24: Frequency content of (a) relative displacement and (b) voltage output obtained by model simulation for the neighborhood of secondary resonance excitation (a frequency range including $\Omega \approx \omega_n/3$ and $\Omega \approx \omega_n/2$). The base acceleration amplitude is $0.4g$ RMS, and load resistance is 300kΩ.

3.3.5.2 Secondary Resonance for Superharmonic Response

Superharmonic and subharmonic resonance behaviors[71] can be observed in the M-shaped piezoelectric energy harvester. However, only the superharmonic resonance range is considered as it may have more practical implications (such as MEMS configurations or other compact designs under high excitation intensities with frequency content well below the primary resonance frequency neighborhood). In order to study the 1:2 and 1:3 superharmonic resonance behaviors of the M-shaped energy harvester, simulations and frequency sweep tests are conducted for frequency ranges near one half of the linear natural frequency and one third of the linear natural frequency. To become apparent, secondary resonances typically require higher forcing amplitudes, as they are effectively excited internally by the nonlinearities acting on the quasilinear response, as opposed to being excited by the external forcing directly as with the primary resonance. Tests and simulations are therefore carried out at RMS base acceleration levels of 0.1, 0.2, 0.3, and $0.4g$. Figure 24 shows the displacement and voltage response frequency contents predicted by the 5-term harmonic balance analysis for the cubic and quadratic superharmonic resonance neighborhoods for $0.4g$ RMS base acceleration.

As anticipated based on the quadratic and cubic stiffness terms in Table 2, the quadratic nonlinearity is more significant than the cubic nonlinearity for response levels on the order ∼0.1 cm (which is indeed the displacement response level under $0.4g$ RMS excitation in the range of 4-8 Hz). Therefore, Figure 24 confirms the fact that the predominant secondary

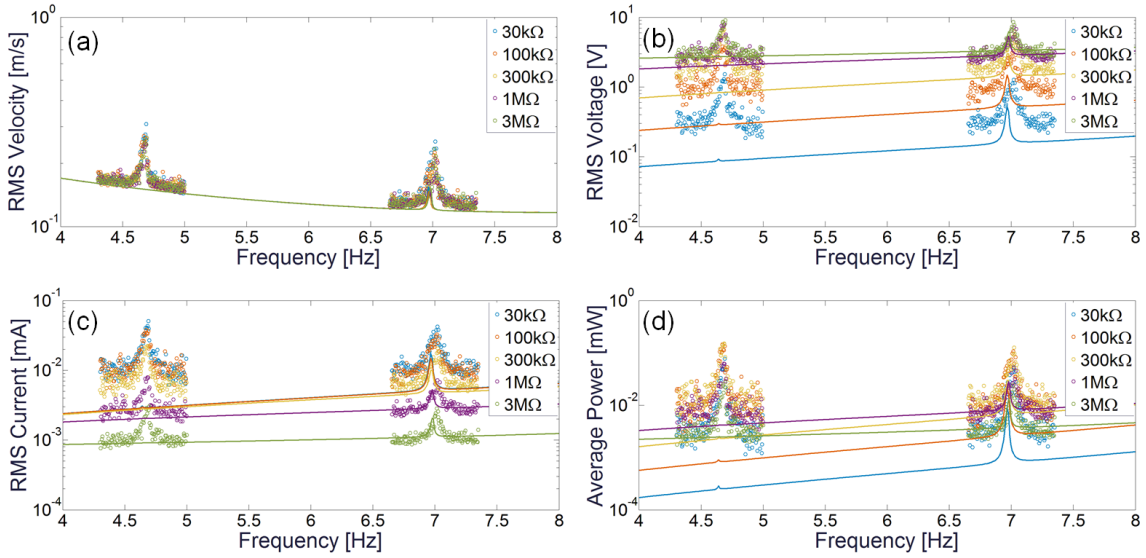

Figure 25: Nonlinear electromechanical frequency response curves in the neighborhood of secondary resonance excitation: (a) velocity, (b) voltage, (c) current, and (d) power output. Base acceleration amplitude is $0.4g$ RMS. Substantial mismatch for $\Omega \approx \omega_n/3$ is due to the shaker's limitation in low-frequency (roughly for < 5 Hz) excitation that results in higher harmonics in base acceleration. Circles represent experimental data and solid curves represent model predictions.

resonance behavior should be expected in the neighborhood of $\Omega \approx \omega_n/2 \approx 7$ Hz; that is, quadratic superharmonic resonance is expected to be the dominant secondary resonance. Figure 25 shows the experimental RMS velocity, voltage, current, and average power output frequency response curves of the M-shaped harvester along with model predictions. Surprisingly, the experimental data shows significant mismatch around $\Omega \approx \omega_n/3 \approx 4.7$ with an unexpected resonance behavior contradicting the previous argument, which is explained next.

In Figure 25, unlike model predictions, the experimental data shows large responses for both the quadratic and cubic superharmonic resonances, with the cubic resonance unexpectedly being the larger of the two. As discussed previously in Section 3.2.5, superharmonic resonance experiments are made more complicated as harmonic distortion in the excitation signal generates response at the same frequencies as those created by the nonlinearities of interest in the harvester. Therefore the major suspect that might cause this unexpected resonance around $\Omega \approx \omega_n/3 \approx 4.7$ is potentially the distortion in the excitation signal itself (i.e. failure of the shaker to produce pure harmonic excitation at low frequencies). The time

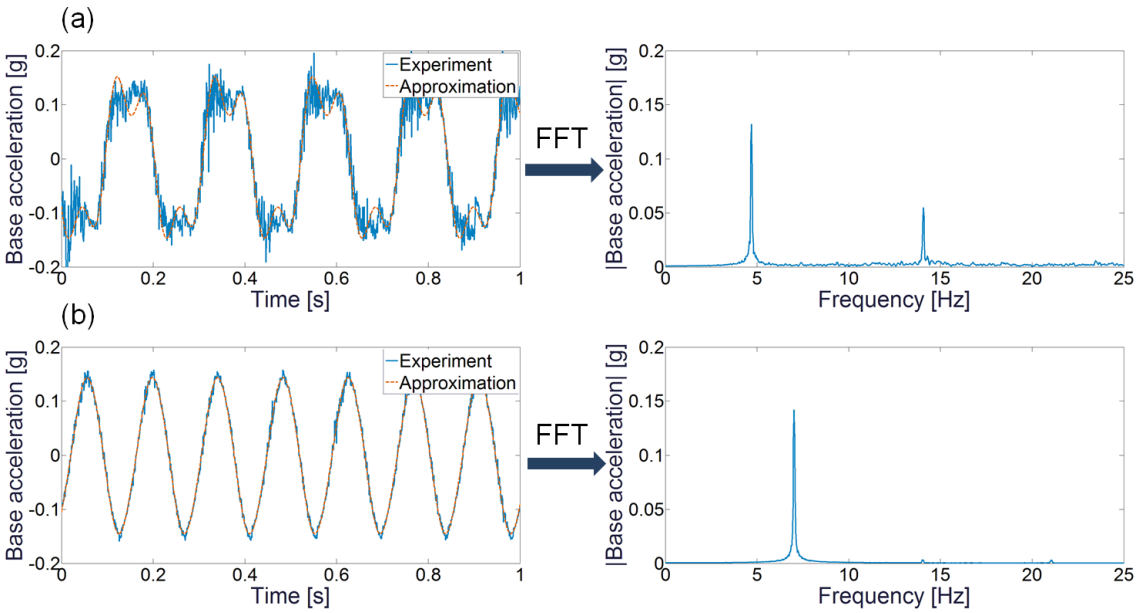

Figure 26: Base acceleration time series produced by the shaker for excitation at (a) 4.7 Hz ($\Omega \approx \omega_n/3$) and (b) 7 Hz ($\Omega \approx \omega_n/2$) along with their FFTs at $0.1g$ RMS base acceleration amplitude. The time series at 4.7 Hz results in multi-harmonic excitation of the harvester due to the shaker's imperfection at low frequencies.

histories of base acceleration signals at 4.7 Hz (i.e. $\Omega \approx \omega_n/3$) and 7 Hz (i.e. $\Omega \approx \omega_n/2$) are shown in Figure 26 along with their FFTs.

For frequencies under approximately 5 Hz, the shaker and vibration controller used for these experiments are unable to produce a suitably pure sinusoidal acceleration. The motion of the shaker is corrupted by a number of sources of error, including measurement noise from the accelerometer (sent to the controller), quantization errors in the digital controller, and perhaps most important for the low frequencies as in these experiments, dry friction in the shaker armature. Dry friction in the shaker armature can cause unwanted stop-start (or "stick-slip") like motion. This causes the desired sinusoidal output acceleration to become distorted into a shape more resembling a square wave, i.e. a signal with content at three times the fundamental frequency (Figure 26(a)). It is therefore concluded that the peak at $\omega_n/3$ seen in experiments is not due to secondary resonance nonlinear behavior, but rather due to harmonic distortion in the input base acceleration exciting the primary resonance directly. Next, knowing the frequency content (Figure 26) of the multi-harmonic excitation caused by the shaker, the frequency response in 4-8 Hz (Figure 25) can be modeled

Table 5: Coefficients of higher harmonics in base acceleration to explore the superharmonic resonance accounting for the multi-harmonic nature of true (experimental) excitation.

	$3\Omega = \omega_n$		$2\Omega = \omega_n$	
g_{RMS}	α_2	α_3	α_2	α_3
0.1	0.0342	0.3823	0.0214	0.0206
0.2	0.0296	0.1095	0.0116	0.0572
0.3	0.0178	0.0320	0.0248	0.0240
0.4	0.0069	0.0456	0.0340	0.0257

more accurately as a combined exercise of multi-harmonic excitation and superharmonic secondary resonance. In order to better model the experimental behavior around 4.7 Hz (i.e. $\Omega \approx \omega_n/3$) and 7 Hz (i.e. $\Omega \approx \omega_n/2$), the true (non-ideal) representation of the base acceleration can be used based on Figure 26:

$$\ddot{y}(t) = A\left[\cos(\Omega t) + \alpha_2 \cos(2\Omega t + \phi_2) + \alpha_3 \cos(3\Omega t + \phi_3)\right] \tag{67}$$

Here, A is the nominal acceleration amplitude (at the intended single-frequency excitation), and α_2 and α_3 are the amplitudes of the harmonics of interest expressed as fractions of the nominal acceleration (for ideal single frequency excitation, $\alpha_2 = \alpha_3 = 0$). The values of the coefficients of the higher harmonic components in the base acceleration signal are found by recording time histories of steady-state base acceleration signals at the frequencies of interest and extracting their frequency content (as shown in Figure 26 for $0.1g$ RMS base acceleration). The coefficients needed to properly model the base acceleration seen in the performed experiments are summarized in Table 5.

Using this more accurate model of the base acceleration signal and the ability of the method of harmonic balance to simulate the response of the M-shaped harvester to multi-harmonic excitation, the observed behavior can be simulated. The experimental RMS velocity, voltage, current, and average power output and model predictions with the multi-harmonic base acceleration model are shown in Figure 27. The 3–harmonic model for the base acceleration signal used in the 5–term harmonic balance solution results in a much better prediction of the observed experimental responses amplitudes. The model simulation still differs from the observed response in that the model predicts hardening jump phenomenon behavior, while the experimental data shows no clear jump, which may

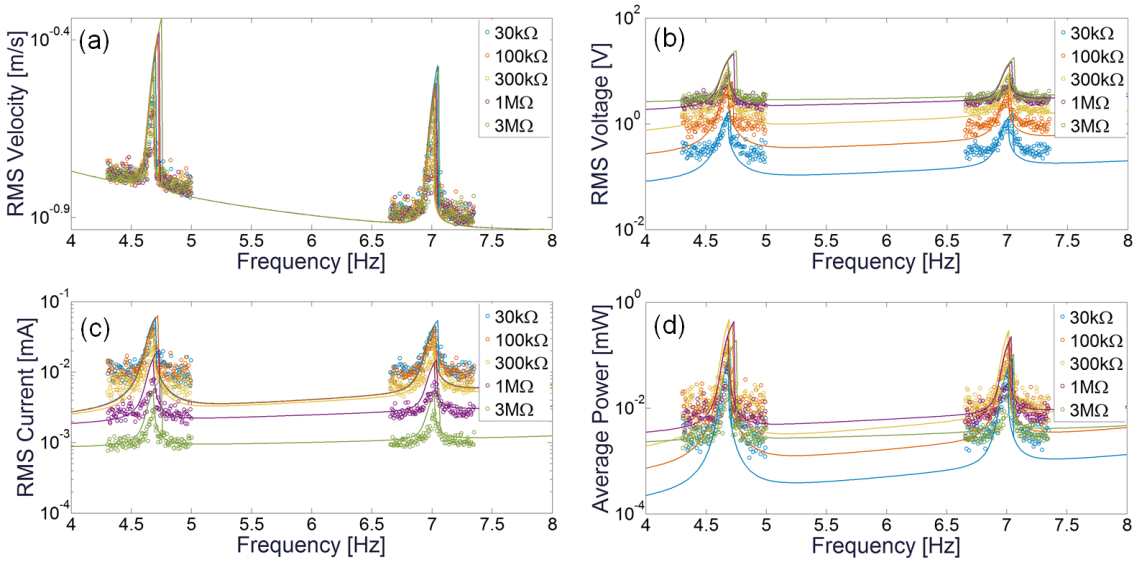

Figure 27: Nonlinear electromechanical frequency response curves in the neighborhood of secondary resonance excitation (a frequency range including $\Omega \approx \omega_n/3$ and $\Omega \approx \omega_n/2$) by accounting for multi-harmonic excitation effects of the shaker in modeling: (a) velocity, (b) voltage, (c) current, and (d) power output. The base acceleration amplitude is $0.4g$ RMS. Circles represent experimental data and solid curves represent model predictions.

be attributed to the fact that the experimental base acceleration is significantly noisier than the ideal 3–harmonic excitation used in the model.

An interesting observation is regarding the optimal resistance of the maximum power output. When attempting to harvest energy from superharmonic resonances, the optimal load impedance for the energy harvester will be close to the optimal load impedance for the same harvester under primary resonance excitation. This is because the optimal load impedance depends on the dominant frequency content of the harvesters response, not the dominant frequency content of the excitation. For a properly tuned linear resonant vibration energy harvester (and for a nonlinear harvester operating under primary resonance excitation), the dominant frequency of the response will match the dominant frequency of excitation, but this is not the case for secondary resonance behavior of a nonlinear energy harvester as it is the response frequency content that matters. Beyond the intriguing nature of secondary resonance excitations as a nonlinear dynamics exercise, superharmonic resonance behavior may be exploited for energy harvesting purposes as it allows low frequency

ambient vibrations to excite energy harvesting devices that might have higher natural frequencies due to size and mass constraints (e.g. MEMS energy harvesters) in the sense of nonlinear frequency-up converter[14]. Since secondary resonances require higher forcing amplitudes to become apparent, power generation efficiency will be smaller than for primary resonance excitation.

3.4 Conclusions

Nonlinear frequency bandwidth enhancement in vibration energy harvesting can be achieved most effectively in the presence of strong nonlinearities and under high excitation levels. This constitutes a fundamental challenge in enabling nonlinear energy harvesters for low-intensity environments. To overcome the need for high excitation intensities that are required to exploit nonlinear dynamic phenomena, an M-shaped piezoelectric energy harvester configuration was developed that can exhibit a nonlinear frequency response under very low vibration levels (below $0.1g$). This configuration was made from a continuous bent spring steel with piezoelectric laminates and a proof mass but no magnetic components. Properly locating the piezoelectric patches (to avoid substantial piezoelectric softening) in this design enables achieving the jump phenomenon in hardening at a few milli-g base acceleration levels.

Both primary and secondary (superharmonic) resonance excitations were explored at different vibration levels and load resistance values. The primary resonance excitation case that offers a 660% increase in the half-power bandwidth as compared to the linear system at a root-mean-square excitation level as low as $0.04g$. The secondary resonance behavior was investigated with a focus on 1:2 and 1:3 superharmonic resonances. Following the development of an empirical model, a multi-term harmonic balance framework was developed for a computationally effective yet high-fidelity analysis of this high-quality-factor system with cubic and quadratic nonlinearities. Experimental measurements and electromechanical model predictions resulted in very good match for both primary and secondary resonance cases explored in this work.

Overall, substantial nonlinear bandwidth is achieved for very low base acceleration levels under primary resonance excitation. The secondary resonance of interest in this work was superharmonic resonance for nonlinear frequency-up conversion. It has been pointed out that the optimal electrical load of superharmonic response is close to that of the same harvester under primary resonance excitation. This is because the optimal load impedance depends on the dominant frequency content of the harvesters response, rather than the dominant frequency content of the excitation (no such distinction exists in linear harvesters or nonlinear ones under primary resonance excitation). Superharmonic resonance behavior may be exploited for energy harvesting purposes as it allows low frequency ambient vibrations to excite energy harvesting devices that might have higher natural frequencies due to size and mass constraints (e.g. MEMS energy harvesters), as a nonlinear frequency-up conversion mechanism.

In low-frequency superharmonic resonance experiments, an experimental imperfection of the electrodynamic shaker (which fails to produce pure harmonic signal for excitations roughly below 5 Hz) was pointed out and used as an opportunity to formulate and explore nonlinear response to multi-harmonic excitation in the secondary resonance regime. Multi-term harmonic balance solution resulted in very good match for the complex case of multi-harmonic excitation combined with secondary resonance behavior.

Chapter IV

ELECTROELASTIC MATERIAL AND DISSIPATIVE NONLINEARITIES

4.1 Introduction

In this chapter, a physical model for the nonlinear behavior of soft piezoceramic materials is proposed including stiffness, damping, and electromechanical coupling nonlinearities. A distributed parameter electroelastic model is developed by accounting for these nonlinearities to analyze the primary resonance of a cantilever for the fundamental bending mode using the method of harmonic balance. The system to be studied consists of symmetric piezoelectric bimorph cantilever with two piezoelectric layers on either side of a metal central layer. The piezoelectric layers are poled in opposite directions, with the top and bottom surfaces forming the electrodes. A diagram of the bimorph for energy harvesting from base motion and dynamic actuation with fixed base is shown in Figure 29. While the schematics are given for the series connection of piezoelectric layers, the formulation in the following sections will address the parallel connection case as well.

The cantilever used in this work exhibits high stiffness, resulting in small deflections and slopes for all practical excitation levels within the structural failure limits. This ensures that geometric nonlinearity is negligible, making observation and identification of the electroelastic nonlinearities of interest possible. Considering the work of von Wagner and Hagedorn [104] and Goldschmidtboeing et al. [38], the following nonlinear electric enthalpy density expression is proposed along with a nonlinear structural dissipation term:

$$H = \frac{1}{2}c_{11}S_1^2 + \frac{1}{3}c_{111}S_1^3\,\mathrm{sgn}(S_1) - e_{31}S_1E_3 - \frac{1}{2}e_{311}S_1^2\,\mathrm{sgn}(S_1)E_3 - \frac{1}{2}\epsilon_{33}E_3^2 \tag{68}$$

$$U_{dis} \propto |S_1|^3. \tag{69}$$

As discussed previously, common practice currently is to express the enthalpy as a polynomial in the strain and electric field. When applying such a model to a symmetric structure,

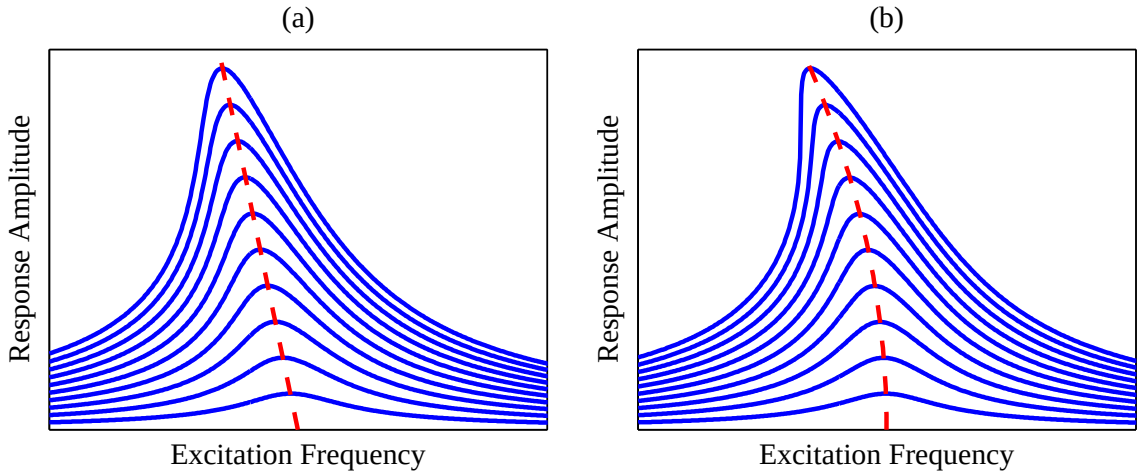

Figure 28: Response of an oscillator with quadratic (a) and cubic (b) softening stiffness nonlinearity. Response curves at various excitation amplitudes are shown by solid blue lines. The backbone curve is shown by a dashed red line.

terms proportional to second order nonlinear coefficients vanish, making third order nonlinear terms necessary to predict any nonlinear behavior. In this work, electric enthalpy density expressed as a polynomial in the strain magnitude, rather than the strain itself is proposed. In this way, second order terms do not vanish unlike the previous efforts [104]. For illustration, Figure 28 shows behavior due to quadratic and cubic stiffness nonlinearities.

While both quadratic and cubic stiffness models can exhibit the same type of nonlinearities (hardening or softening) as an experimentally observed system, the two models are qualitatively different. This is apparent by examining the *backbone curve*, which connects the peaks of frequency response curves at all excitation amplitudes. A quadratic stiffness model predicts a backbone curve that changes linearly with the response amplitude. A cubic stiffness model predicts a quadratic variation of the peak response frequency with response amplitude. As shown by Goldschmidtboeing et al. [38], stiff piezoelectric bimorphs display a linear decrease in peak response frequency with increased excitation level. In fact, other published experimental data in the literature also exhibit first-order backbone curve trends, e.g. Figure 4 in Usher and Sim [102] and Figure 5 in Mahmoodi et al. [59], among others, while the respective models predict second-order backbone curves. Therefore, a model is required that does not allow second order stiffness and electromechanical coupling terms to

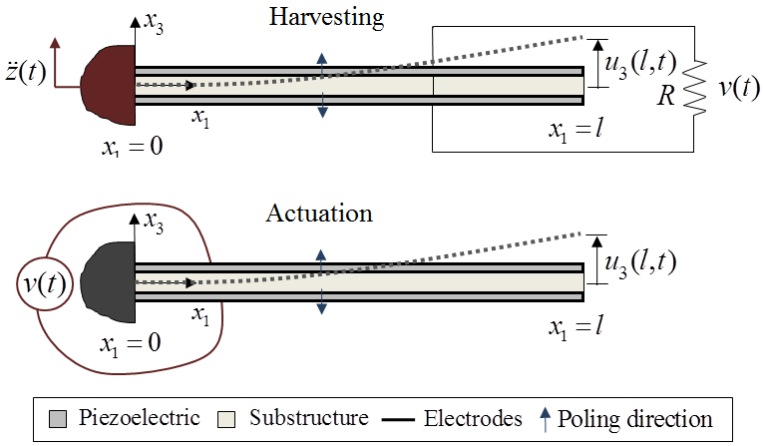

Figure 29: Schematic representation of a piezoelectric bimorph for operation in base motion energy harvesting and actuation with series connected electrodes.

vanish. As for nonlinear dissipation, only mechanical hysteresis is assumed with Equation 69, since the present work is intended for low-to-moderate excitation levels near resonance, yielding electric fields well below of the coercive field of piezoelectric layers. Therefore ferroelectric (polarization-electric field) and dielectric (electric displacement-field) hysteresis effects [21] and resulting high-field losses are excluded in this framework.

4.2 Distributed Parameter Model Derivation

The primary system to be studied consists of symmetric piezoelectric bimorph cantilever with two piezoelectric layers on either side of a metal central layer. The piezoelectric layers are poled in opposite directions, with the top and bottom surfaces forming the electrodes. A diagram of the bimorph for energy harvesting from base motion and dynamic actuation with fixed base is shown in Figure 29.

The cantilever used in this work exhibits high stiffness, resulting in small deflections and slopes for all practical excitation levels within the structural failure limits. This ensures that geometric nonlinearity is negligible, making observation and identification of the elastic nonlinearity of interest possible. As mentioned previously, the nonlinear resonant behavior of stiff piezoelectric cantilevers made with soft piezoelectric materials (e.g. PZT-5A and

PZT-5H), is dominated by elastic and dissipative nonlinearities.

$$H = \frac{1}{2}c_{11}S_1^2 + \frac{1}{3}c_{111}S_1^3\,\mathrm{sgn}(S_1) - e_{31}S_1E_3 - \frac{1}{2}e_{311}S_1^2\,\mathrm{sgn}(S_1)E_3 - \frac{1}{2}\epsilon_{33}E_3^2. \tag{70}$$

Here c_{11} and c_{111} are the real components of the complex first and second order elastic moduli, c_{11}^* and c_{111}^*, respectively. The imaginary portion governs the first and second order dissipation. The complex moduli can be written in the form,

$$c_{11}^* = c_{11}(1 + \gamma_1 j) \tag{71}$$

$$c_{111}^* = c_{111}(1 - \gamma_2 j) \tag{72}$$

The terms γ_1 and γ_2 can be viewed as the first and second order loss tangents, respectively. From the electric enthalpy density expression, the longitudinal stress, T_1, and the transverse electric displacement, D_3, can be found using the following relations:

$$T_1 = \frac{\partial H}{\partial S_1} = c_{11}S_1 + c_{111}S_1^2\,\mathrm{sgn}(S_1) - e_{31}E_3 - e_{311}S_1\,\mathrm{sgn}(S_1)E_3 \tag{73}$$

$$D_3 = -\frac{\partial H}{\partial E_3} = e_{31}S_1 + \frac{1}{2}e_{311}S_1^2\,\mathrm{sgn}(S_1) + \epsilon_{33}E_3, \tag{74}$$

which satisfy the relation,

$$\frac{\partial T_1}{\partial E_3} = -\frac{\partial D_3}{\partial S_1}. \tag{75}$$

Deformations are assumed to be small (in agreement with the experiments for the stiff and brittle sample explored in this work), therefore axial strain in the beam is modeled using Euler-Bernoulli theory, namely

$$S_1 = -x_3u_3''(x_1, t), \tag{76}$$

where $u_3(x_1, t)$ is the transverse deflection of the beam from equilibrium, and $(\ )'$ denotes the spatial derivative, $\partial/\partial x_1$. For the case of series connected piezoelectric laminates (which is the case in the experimental samples of this work), the transverse electric field is modeled as

$$E_3 = -\frac{\dot{\lambda}}{2h_p}\,\mathrm{sgn}(x_3), \tag{77}$$

where λ is the electric flux linkage coordinate [90, 89, 20, 54], h_p is the thickness of each piezoelectric layer, and $\dot{(\ )}$ denotes the time derivative, $\partial/\partial t$. The time derivative of flux

linkage represents the electrode voltage, which will be substituted in later in the analysis. The sign of the electric field is opposite for the two piezoelectric laminates to account for the oppositely poled piezoelectric material on each side. The total kinetic energy of the beam undergoing prescribed transverse base motion is,

$$T = \frac{1}{2}\int_0^l \hat{m}\left[\dot{u}_3 + \dot{z}(t)\right]^2 dx_1. \tag{78}$$

The base velocity is denoted by, $\dot{z}(t)$, and $\hat{m}$ represents the mass per unit length of the bimorph. The total potential energy of the piezoelectric bimorph is the sum of the potential energies of the substrate, U_s, and piezoelectric laminates, U_p:

$$U = U_s + U_p. \tag{79}$$

The substrate strain energy can be expressed as,

$$U_s = \frac{1}{2}\int_0^l \frac{c_s b h_s^3}{12}\left(u_3''\right)^2 dx_1, \tag{80}$$

where c_s is the substrate Young's modulus, b is the width of the beam, and h_s is the thickness of the substrate layer. The piezoelectric laminate potential energy is volumetric integral of the electric enthalpy density, H.

$$U_p = \int_{V_p} H dV_p = \int_0^l \left\{ \int_{-\frac{b}{2}}^{\frac{b}{2}} \left[\int_{\frac{h_s}{2}}^{\frac{h_s}{2}+h_p} H dx_3 \; + \; \int_{-\frac{h_s}{2}-h_p}^{-\frac{h_s}{2}} H dx_3 \right] dx_2 \right\} dx_1 \tag{81}$$

Performing the spatial integration over the cross section yields the following potential energy expression:

$$U = \frac{1}{2}\int_0^l \left\{ \hat{k}_1\left(u_3''\right)^2 + \frac{1}{3}\hat{k}_2\left(u_3''\right)^3 \operatorname{sgn}(u_3'') - \left[2\hat{\theta}_1 u_3'' + \hat{\theta}_2\left(u_3''\right)^2 \operatorname{sgn}(u_3'')\right]\dot{\lambda} \right\} dx_1 - \frac{1}{2}C\dot{\lambda}^2 \tag{82}$$

The distributed mass and stiffness coefficients are given as:

$$\begin{aligned}
\hat{m} &= b(\rho_s h_s + 2\rho_p h_p) \\
\hat{k}_1 &= \frac{1}{12}c_s b h_s^3 + \frac{1}{6}c_{11} b h_p\left(4h_p^2 + 6h_p h_s + 3h_s^2\right) \\
\hat{k}_2 &= \frac{1}{2}c_{111} b h_p\left(2h_p^3 + 4h_p^2 h_s + 3h_p h_s^2 + h_s^3\right)
\end{aligned} \tag{83}$$

To take into account dissipation, $\hat{k}_1$ and $\hat{k}_2$ are allowed to be complex quantities defined as:

$$\begin{aligned}
\hat{k}_1^* &= \frac{1}{12}c_s b h_s^3 + \frac{1}{6}c_{11}^* b h_p\left(4h_p^2 + 6h_p h_s + 3h_s^2\right) \\
\hat{k}_2^* &= \frac{1}{2}c_{111}^* b h_p\left(2h_p^3 + 4h_p^2 h_s + 3h_p h_s^2 + h_s^3\right)
\end{aligned} \tag{84}$$

For series connected electrodes, the electromechanical coupling coefficients and harvester capacitance are,

$$\begin{aligned}\hat{\theta}_1 &= \frac{1}{2} e_{31} b \left(h_p + h_s\right) \\ \hat{\theta}_2 &= \frac{1}{12} e_{311} b \left(4h_p^2 + 6h_p h_s + 3h_s^2\right) \\ C &= \frac{b l_e \epsilon_{33}}{2h_p}.\end{aligned} \tag{85}$$

For parallel connected electrodes, the electromechanical coupling coefficients and harvester capacitance are,

$$\begin{aligned}\hat{\theta}_1 &= e_{31} b \left(h_p + h_s\right) \\ \hat{\theta}_2 &= \frac{1}{6} e_{311} b \left(4h_p^2 + 6h_p h_s + 3h_s^2\right) \\ C &= \frac{2b l_e \epsilon_{33}}{h_p}.\end{aligned} \tag{86}$$

The capacitance, C, depends on the effective length of the bimorph, l_e, rather than the overhanging cantilever length, l. In this work, the total length is used for l_e. To generate governing partial differential equations and boundary conditions, Hamilton's principle is used.

$$\int_{t_0}^{t_1} \left(\delta L + \delta W_{nc}\right) dt = 0 \tag{87}$$

The Lagrangian, L, is the difference of kinetic and potential energy, $T - U$, and δW_{nc} is the nonconservative virtual work. The variation of the Lagrangian can be expressed using the chain rule,

$$\delta L \left(\dot{u}_3, u_3'', \dot{\lambda}\right) = \frac{\partial L}{\partial \dot{u}_3} \delta \dot{u}_3 + \frac{\partial L}{\partial \dot{\lambda}} \delta \dot{\lambda} + \frac{\partial L}{\partial u_3''} \delta u_3''. \tag{88}$$

The nonconservative virtual work is due to Joule heating of the load resistance, as given in the following equation.

$$\delta W_{nc} = -\frac{\dot{\lambda}}{R} \delta \lambda \tag{89}$$

Integrating by parts results in a variational expression for the governing partial differential

equations and boundary conditions.

$$\int_{t_0}^{t_1} \Bigg\{ \left[-\frac{\partial}{\partial t}\left(\frac{\partial L}{\partial \dot{u}_3}\right) + \frac{\partial^2}{\partial x_1^2}\left(\frac{\partial L}{\partial u_3''}\right)\right]\delta u_3 + \left[-\frac{\partial}{\partial t}\left(\frac{\partial L}{\partial \dot{\lambda}}\right) - \frac{\dot{\lambda}}{R}\right]\delta\lambda + \left[-\frac{\partial}{\partial x_1}\left(\frac{\partial L}{\partial u_3''}\right)\right]\delta u_3\Big|_0^l + \frac{\partial L}{\partial u_3''}\delta u_3'\Big|_0^l \Bigg\} dt = 0 \tag{90}$$

The first portion governs the mechanical domain for arbitrary δu_3:

$$-\frac{\partial}{\partial t}\left(\frac{\partial L}{\partial \dot{u}_3}\right) + \frac{\partial^2}{\partial x_1^2}\left(\frac{\partial L}{\partial u_3''}\right) = 0, \tag{91}$$

and results in the PDE:

$$\hat{m}\ddot{u}_3 + \hat{k}_1^* u_3'''' + \hat{k}_2^*\left[u_3'' u_3'''' + \left(u_3'''\right)^2\right]\operatorname{sgn}(u_3'') - \left\{\hat{\theta}_1\left[\delta'(x_1) - \delta'(x_1 - l)\right] + \hat{\theta}_2 u_3''''\operatorname{sgn}(u_3'')\right\}\dot{\lambda} = -\hat{m}\ddot{z}(t). \tag{92}$$

Here, δ' represents the first spatial derivative of the Dirac delta function. The second portion of the variational expression for arbitrary $\delta\lambda$ governs the electrical domain:

$$-\frac{\partial}{\partial t}\left(\frac{\partial L}{\partial \dot{\lambda}}\right) - \frac{\dot{\lambda}}{R} = 0, \tag{93}$$

and results in the ODE:

$$C\ddot{\lambda} + \frac{\dot{\lambda}}{R} + \int_0^l \left[\hat{\theta}_1 + \hat{\theta}_2 u_3''\operatorname{sgn}(u_3'')\right]\dot{u}_3'' dx_1 = 0. \tag{94}$$

Substituting voltage, v, for the time derivative of the flux linkage coordinate, λ, yields the following pair of governing differential equations for the piezoelectric bimorph:

$$\hat{m}\ddot{u}_3 + \hat{k}_1^* u_3'''' + \hat{k}_2^*\left[u_3'' u_3'''' + \left(u_3'''\right)^2\right]\operatorname{sgn}(u_3'') - \left\{\hat{\theta}_1\left[\delta'(x_1) - \delta'(x_1 - l)\right] + \hat{\theta}_2 u_3''''\operatorname{sgn}(u_3'')\right\} v = -\hat{m}\ddot{z}(t) \tag{95}$$

$$C\dot{v} + \frac{v}{R} + \int_0^l \left[\hat{\theta}_1 + \hat{\theta}_2 u_3''\operatorname{sgn}(u_3'')\right]\dot{u}_3'' dx_1 = 0. \tag{96}$$

4.3 Discretization

To reduce the partial differential equations to ordinary differential equations, Galerkin's method is applied. A single-mode solution is used for the first bending mode, namely

$$u_3(x_1, t) = x(t)\phi(x_1). \tag{97}$$

Here $x(t) = u_3(l,t)$ is the deflection of the cantilever tip relative to equilibrium, and $\phi(x_1)$ is the unit normalized shape function, i.e.

$$\phi(l) = 1. \tag{98}$$

In this analysis, the first mode shape of a purely mechanical Euler-Bernoulli cantilever beam chosen for ϕ, i.e.

$$\phi(x_1) = \frac{1}{2}\left\{\cosh\left(\frac{\beta x_1}{l}\right) - \cos\left(\frac{\beta x_1}{l}\right) - \sigma\left[\sinh\left(\frac{\beta x_1}{l}\right) - \sin\left(\frac{\beta x_1}{l}\right)\right]\right\}, \tag{99}$$

$$\begin{aligned}\beta &= 1.8751\ldots \\ \sigma &= 0.7341\ldots\end{aligned} \tag{100}$$

Substitution of Equation (97) into Equation (95), multiplying by $\phi(x_1)$, and integrating over the length, yields the following ordinary differential equation for the mechanical behavior of the bimorph,

$$m\ddot{x} + k_1^* x + k_2^* x^2 \operatorname{sgn}(x) - [\theta_1 + \theta_2 x \operatorname{sgn}(x)]\, v = -\bar{m}\ddot{z}(t) \tag{101}$$

Substitution of Equation (97) into Equation (96) results in the governing equation for the electrical behavior of the bimorph,

$$C\dot{v} + \frac{v}{R} + [\theta_1 + \psi_2 x \operatorname{sgn}(x)]\, \dot{x} = 0. \tag{102}$$

The spatially discretized model is parameterized by the following values:

$$\begin{aligned}
m &= \hat{m}\int_0^l \phi^2 dx_1 \\
\bar{m} &= \hat{m}\int_0^l \phi\ dx_1 \\
k_1^* &= \hat{k}_1^*\int_0^l \phi''''\phi\ dx_1 \\
k_2^* &= \hat{k}_2^*\int_0^l \left[\phi''\phi'''' + \left(\phi'''\right)^2\right]\phi \operatorname{sgn}(\phi'')dx_1 \\
\theta_1 &= \hat{\theta}_1\phi'(l) \\
\theta_2 &= \hat{\theta}_2\int_0^l \phi''''\phi \operatorname{sgn}(\phi'')dx_1 \\
\psi_2 &= \hat{\theta}_2\int_0^l \left(\phi''\right)^2 \operatorname{sgn}(\phi'')dx_1.
\end{aligned} \tag{103}$$

With this choice of ϕ, the forward and backward quadratic electromechanical coupling coefficients, θ_2 and ψ_2 are equal.

$$\theta_2 = \psi_2 \tag{104}$$

To correctly analyze the nonlinear dynamics, the governing ODEs must be real-valued. Therefore the imaginary parts of the first and second order stiffness are replaced by equivalent first and second order internal (displacement) damping, namely:

$$m\ddot{x} + \left[d_1 x \operatorname{sgn}(x) + d_2 x^2\right] \operatorname{sgn}(\dot{x}) + k_1 x + k_2 x^2 \operatorname{sgn}(x) - \left[\theta_1 + \theta_2 x \operatorname{sgn}(x)\right] v = -\bar{m}\ddot{z}(t). \tag{105}$$

The first and second order stiffness coefficients, k_1 and k_2, are the real parts of the complex stiffness, k_1^* and k_2^*, respectively.

$$k_1 = \operatorname{Re}\{k_1^*\} \tag{106}$$

$$k_2 = \operatorname{Re}\{k_2^*\} \tag{107}$$

The first and second order dissipation coefficients, d_1 and d_2, are found by equating per cycle energy dissipation assuming harmonic motion and identifying multiplication by the imaginary unit, j, with a phase shift of $\pi/2$. Explicitly,

$$\begin{aligned} x(t) &= X\cos\left(\Omega t + \gamma\right) \\ jx(t) &= X\cos\left(\Omega t + \gamma + \frac{\pi}{2}\right) = -X\sin\left(\Omega t + \gamma\right) \\ \dot{x}(t) &= -\Omega X\sin\left(\Omega t + \gamma\right). \end{aligned} \tag{108}$$

The mechanical energy dissipated per cycle due to the first order damping term can then be written as:

$$\int_0^{2\pi/\Omega} \operatorname{Im}\{k_1^*\} jx\dot{x}dt = \int_0^{2\pi/\Omega} d_1 x \operatorname{sgn}(x)\dot{x}\operatorname{sgn}(\dot{x})dt \tag{109}$$

Similarly, the mechanical energy dissipated per cycle due to the second order damping term can be written as:

$$\int_0^{2\pi/\Omega} \operatorname{Im}\{k_2^*\}\left(jx\right)^2 \operatorname{sgn}\left(jx\right)\dot{x}dt = \int_0^{2\pi/\Omega} d_2 x^2 \dot{x}\operatorname{sgn}(\dot{x})dt. \tag{110}$$

After rearranging, the dissipation coefficients are therefore defined as:

$$d_1 = \frac{\pi}{2}\operatorname{Im}\{k_1^*\} \tag{111}$$

$$d_2 = 2\operatorname{Im}\{k_2^*\} \tag{112}$$

4.3.1 Energy Harvesting and Sensing

For the case of energy harvesting and sensing, the bimorph is subjected to a transverse base acceleration, $\ddot{z}(t)$, and the electrodes are shunted by a load resistance, R. The lumped parameter dynamical model for energy harvesting is given as,

$$m\ddot{x} + \left[d_1 x\,\mathrm{sgn}(x) + d_2 x^2\right]\mathrm{sgn}(\dot{x}) + k_1 x + k_2 x^2\,\mathrm{sgn}(x) - \left[\theta_1 + \theta_2 x\,\mathrm{sgn}(x)\right]v = -\bar{m}\ddot{z}(t) \quad (113)$$

$$C\dot{v} + \frac{v}{R} + \left[\theta_1 + \theta_2 x\,\mathrm{sgn}(x)\right]\dot{x} = 0. \quad (114)$$

The coordinates, x and v, are the relative tip displacement of the cantilever and the voltage across the electrodes. Here, $\bar{m}$ and m are base acceleration forcing constant and the effective mass of the beam. The parameters, d_1, k_1, and θ_1, are the linear damping, stiffness, and electromechanical coupling constants, respectively. The parameters k_2, d_2, and θ_2 represent the nonlinear stiffness, damping, and electromechanical coupling effects. The equivalent capacitance, C, is the value measured across the electrodes of the bimorph.

4.3.2 Dynamic Actuation

The dynamic actuation case refers to the piezolectric bimorph fixed from one end to a rigid base, and a prescribed dynamic voltage, $v(t)$, applied to the electrodes.

$$m\ddot{x} + \left[d_1 x\,\mathrm{sgn}(x) + d_2 x^2\right]\mathrm{sgn}(\dot{x}) + k_1 x + k_2 x^2\,\mathrm{sgn}(x) = \left[\theta_1 + \theta_2 x\,\mathrm{sgn}(x)\right]v(t) \quad (115)$$

$$C\dot{v} + i + \left[\theta_1 + \theta_2 x\,\mathrm{sgn}(x)\right]\dot{x} = 0 \quad (116)$$

The model differs from the energy harvesting case in that the electromechanical coupling is now the forcing term on the right hand side of Equation 115, and the current through the bimorph, i, is supplied by the power source, rather than related to the voltage across the load resistance by Ohm's Law. The model parameters are the same as in Section 4.3.1, making Equations 113-116 a global set of nonlinear nonconservative equations in physical coordinates for energy harvesting, sensing, and dynamic actuation.

4.4 Harmonic Balance Analysis

The method of harmonic balance has been used extensively to analyze periodic solutions of nonlinear ordinary differential equations. A Fourier series solution is assumed, replacing

the ordinary differential equations with algebraic equations. The error of the approximate solution is minimized in the Galerkin method sense. The resulting system of algebraic equations is solved iteratively, with a method such as the Newton-Raphson method. In this analysis, a single term harmonic balance solution is sufficient to approximate the steady-state response to harmonic excitation.

4.4.1 Energy Harvesting and Sensing

For the energy harvesting and sensing configuration, base acceleration is taken to be harmonic with constant amplitude, i.e.

$$\ddot{z}(t) = A\cos(\Omega t) \tag{117}$$

The unknown steady-state tip displacement and voltage responses are assumed to be of the form:

$$\begin{aligned} x(t) &= X_1\cos(\Omega t) + X_2\sin(\Omega t) \\ v(t) &= V_1\cos(\Omega t) + V_2\sin(\Omega t) \end{aligned} \tag{118}$$

The amplitude of x is given by $X = \sqrt{X_1^2 + X_2^2}$. Subsitution of Equations 117 and 118 into Equations 113 and 114 and application of the harmonic balance method yields the following set of algebraic equations in X_1, X_2, V_1, and V_2:

$$\begin{aligned} &-m\Omega^2 X_1 + \left(\frac{2}{\pi}d_1 + \frac{4}{3\pi}d_2 X\right)X_2 + \left(k_1 + \frac{8}{3\pi}k_2 X\right)X_1 - \theta_1 V_1 \\ &\quad - \frac{4}{3\pi}\theta_2\left[\frac{\left(2X_1^2 + X_2^2\right)V_1 + X_1 X_2 V_2}{X}\right] + \bar{m}A = 0 \\ &-m\Omega^2 X_2 - \left(\frac{2}{\pi}d_1 + \frac{4}{3\pi}d_2 X\right)X_1 + \left(k_1 + \frac{8}{3\pi}k_2 X\right)X_2 - \theta_1 V_2 \\ &\quad - \frac{4}{3\pi}\theta_2\left[\frac{X_1 X_2 V_1 + \left(X_1^2 + 2X_2^2\right)V_2}{X}\right] = 0 \\ &C\Omega V_2 + \frac{1}{R}V_1 + \left(\theta_1 + \frac{4}{3\pi}\theta_2 X\right)\Omega X_2 = 0 \\ &C\Omega V_1 - \frac{1}{R}V_2 + \left(\theta_1 + \frac{4}{3\pi}\theta_2 X\right)\Omega X_1 = 0. \end{aligned} \tag{119}$$

4.4.2 Dynamic Actuation

For the dynamic actuation configuration, the unknown steady-state tip displacement is the same as in Equation 118, while the voltage is replaced by the expression:

$$v(t) = V\cos(\Omega t). \tag{120}$$

The current flow through the piezoelectric bimorph is assumed to be of the form:

$$i(t) = I_1\cos(\Omega t) + I_2\sin(\Omega t). \tag{121}$$

Substituting Equations 120 and 121 into Equations 115 and 116 and application of the harmonic balance method yields the follow set of algebraic equations in X_1, X_2, I_1, and I_2:

$$\begin{aligned}
&-m\Omega^2 X_1 + \left(\frac{2}{\pi}d_1 + \frac{4}{3\pi}d_2 X\right)X_2 + \left(k_1 + \frac{8}{3\pi}k_2 X\right)X_1 \\
&\quad - \left[\theta_1 + \frac{4}{3\pi}\theta_2\left(\frac{2X_1^2 + X_2^2}{X}\right)\right]V = 0 \\
&-m\Omega^2 X_2 - \left(\frac{2}{\pi}d_1 + \frac{4}{3\pi}d_2 X\right)X_1 + \left(k_1 + \frac{8}{3\pi}k_2 X\right)X_2 \\
&\quad - \frac{4}{3\pi}\theta_2\left(\frac{X_1 X_2}{X}\right)V = 0 \\
&I_1 + \left(\theta_1 + \frac{4}{3\pi}\theta_2 X\right)\Omega X_2 = 0 \\
&-I_2 + \left(\theta_1 + \frac{4}{3\pi}\theta_2 X\right)\Omega X_1 + C\Omega V = 0.
\end{aligned} \tag{122}$$

4.4.3 Quasi-Static Actuation

Low frequncy harmonic actuation can be analyzed simply by setting the forcing frequency, Ω, equal to zero in Equation 122 yielding,

$$\begin{aligned}
&\left(\frac{2}{\pi}d_1 + \frac{4}{3\pi}d_2 X\right)X_2 + \left(k_1 + \frac{8}{3\pi}k_2 X\right)X_1 - \left[\theta_1 + \frac{4}{3\pi}\theta_2\left(\frac{2X_1^2 + X_2^2}{X}\right)\right]V = 0 \\
&-\left(\frac{2}{\pi}d_1 + \frac{4}{3\pi}d_2 X\right)X_1 + \left(k_1 + \frac{8}{3\pi}k_2 X\right)X_2 - \frac{4}{3\pi}\theta_2\left(\frac{X_1 X_2}{X}\right)V = 0.
\end{aligned} \tag{123}$$

4.5 Experimental Validation

To validate the proposed model with quadratic nonlinearities in stiffness, damping, and electromechanical coupling, energy harvesting and dynamic actuation experiments are conducted.

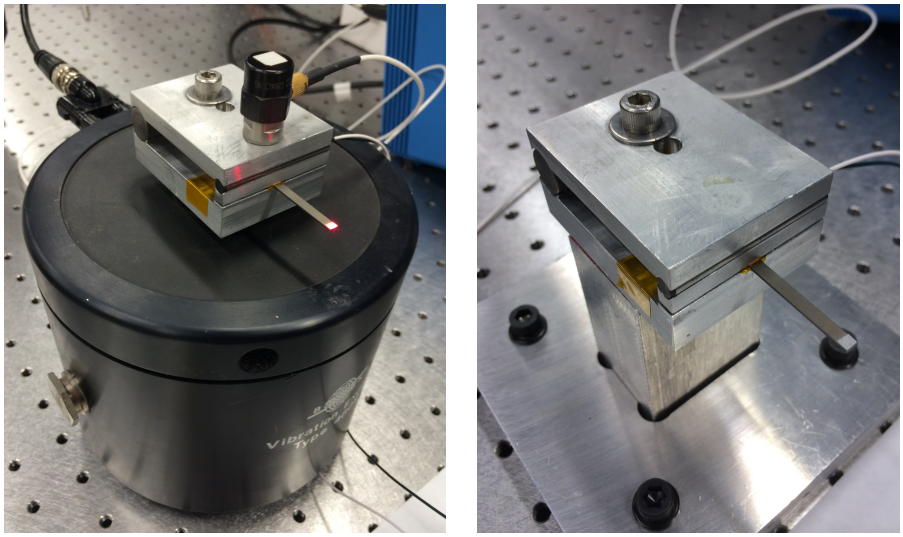

Figure 30: Sample cantilever in fixture mounted to shaker for energy harvesting tests under base excitation (left) and mounted rigidly to table for dynamic actuation tests (right). In the left photograph, the accelerometer used for feedback control of the base accleration is shown.

4.5.1 Experimental Setup

The test sample for the energy harvesting and dynamic actuation tests consists of a brass-reinforced PZT-5A piezoelectric cantilever bimorph (Piezo Systems, Inc. T226-A4-103X) secured in a custom fixture, shown in Figure 30. For base excitation during energy harvesting tests, the fixture is mounted to a shaker (Brüel and Kjær Type 4809). Forward and reverse frequency sweeps at constant base acceleration amplitude are conducted using a vibration control system (APS Dynamics, Inc. VCS201) and accelerometer for acceleration feedback (Kistler AG Type 8636C5). The voltage across the cantilever electrodes are shunted across a load resistance box (IET Labs, Inc. RS-201W). Tip velocity measurements are made using a laser-Doppler vibrometer (Polytec, Inc. OFV-505) and controller (Polytec, Inc. OFV-5000). Data is collected using National Instruments NI 9215 and NI 9223 data acquisition units. During dynamic actuation experiments, the fixture is mounted to a rigid support. The actuation voltage signal is generated by a National Instruments NI USB-4431 and amplified using a power amplifier (Trek, Inc. Model 2220). Output voltage and current data are collected from the amplifier, as well as tip velocity measurements from the

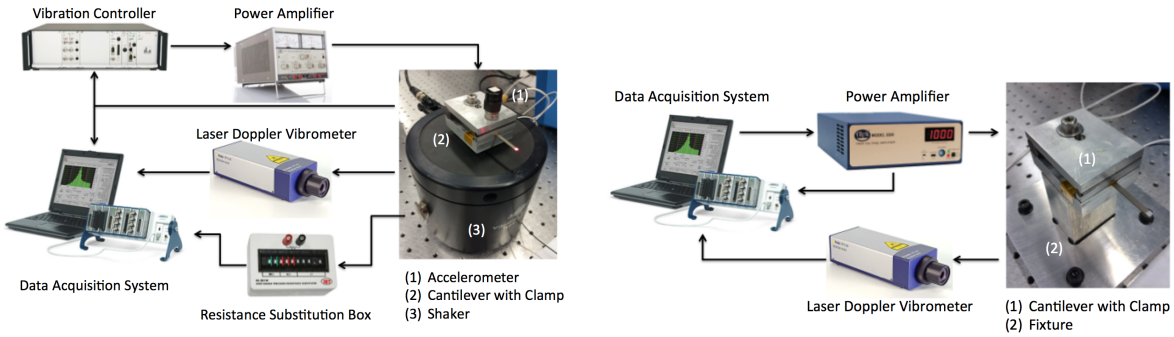

Figure 31: Flow charts of energy harvesting (left) and dynamic actuation (right) experimental apparatuses.

Table 6: Identified model parameters.

Forcing mass	$\bar{m}$	1.58e-4	kg
Effective mass	m	8.79e-5	kg
First order damping	d_1	1.2e1	N/m
Second order damping	d_2	3.25e5	N/m^2
First order stiffness	k_1	6.39e2	N/m
Second order stiffness	k_2	-4.8e5	N/m^2
First order coupling	θ_1	3.29e-4	N/V
Second order coupling	θ_2	3.5e-1	N/Vm
Capacitance	C	2.76e-9	F

laser-Doppler vibrometer and recorded using the NI USB-4431. Schematic representations of experimental setups for energy harvesting and dynamic actuation experiments are shown in Figure 31.

The identified model parameters are summarized in Table 6.

4.5.2 Energy Harvesting Experiments and Model Validation

Energy harvesting experiments consist of frequency sweep tests at seven constant acceleration levels ranging from $0.01g$ RMS to $1.0g$ RMS. Tests at each acceleration level were repeated for nine load resistance values ranging from 1kΩ to 10MΩ, which cover a broad range between short- and open-circuit conditions. The upper limit for the base acceleration level results in a tip displacement approximately 60% of the maximum allowable tip displacement given by the manufacturer. The tests therefore span nearly the entire safe

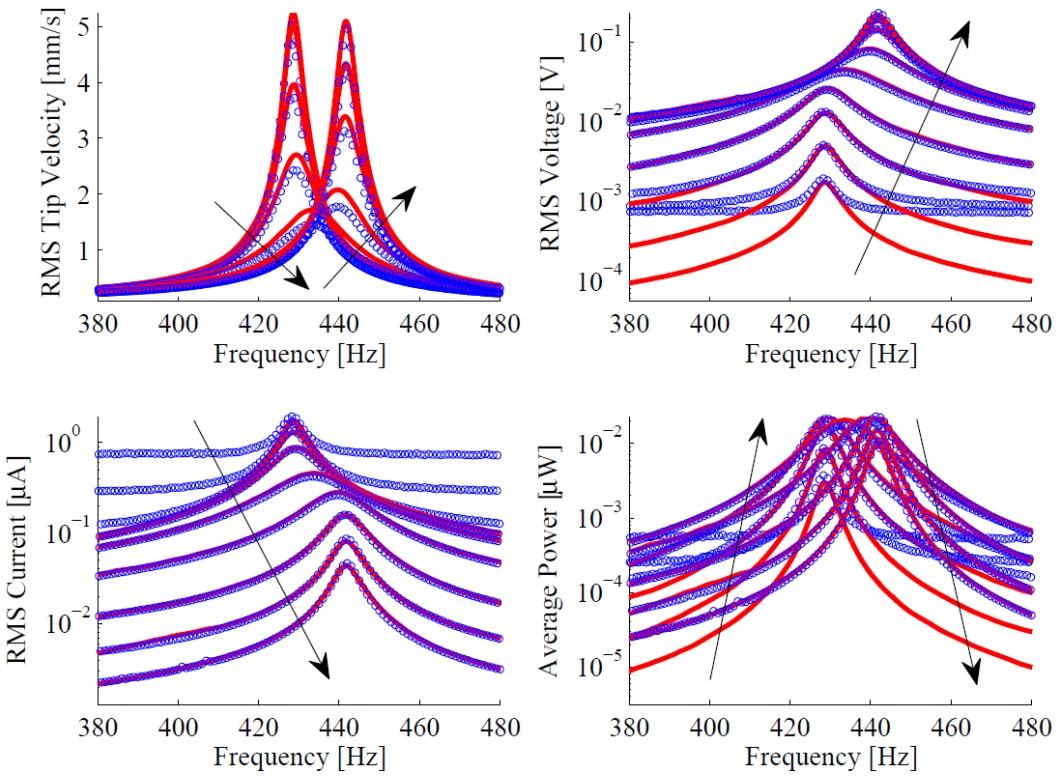

Figure 32: Resistor sweep energy harvesting test at $0.01g$ RMS base acceleration level for resistance values of 1kΩ, 3kΩ, 10kΩ, 30kΩ, 100kΩ, 300kΩ, 1MΩ, 3MΩ, and 10MΩ. Blue circles represent experimental data, and red curves represent model predictions. Arrows indicate direction of increasing load resistance.

operation limits for the cantilever bimorph. Figures 32-34 display the RMS tip velocity and RMS voltage for the cantilever for different base acceleration and load resistance levels.

As shown in Figure 32, the model and experiment show excellent correlation at a low base acceleration level, where linear behavior is expected. The model and experiment only disagree for the voltage curves, when the harvester voltage is below the noise floor of the data acquisition unit, which is an experimental limitation. Agreement of the model and experiment in the linear behavior regime is important, but expected, as high-fidelity models for the linear behavior of piezoelectric cantilevers are readily available.[27, 32, 34] Nonlinear behavior begins to appear at base acceleration levels as low as $0.05g$ RMS, and is readily apparent at $0.1g$ RMS, as shown in Figure 33.

The short- and open-circuit resonant frequencies drop from 428 Hz and 442 Hz to 426 Hz and 440 Hz respectively. Similarly, an increase in damping is observed as an order of

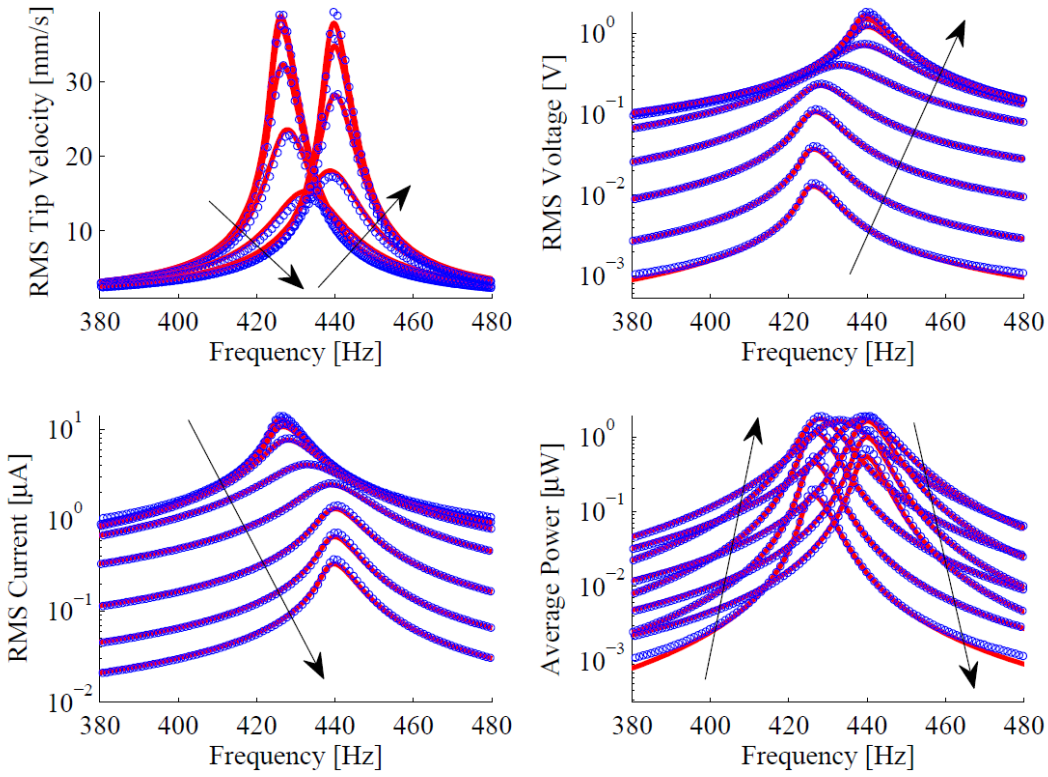

Figure 33: Resistor sweep energy harvesting test at $0.1g$ RMS base acceleration level for resistance values of 1kΩ, 3kΩ, 10kΩ, 30kΩ, 100kΩ, 300kΩ, 1MΩ, 3MΩ, and 10MΩ. Blue circles represent experimental data, and red curves represent model predictions. Arrows indicate direction of increasing load resistance.

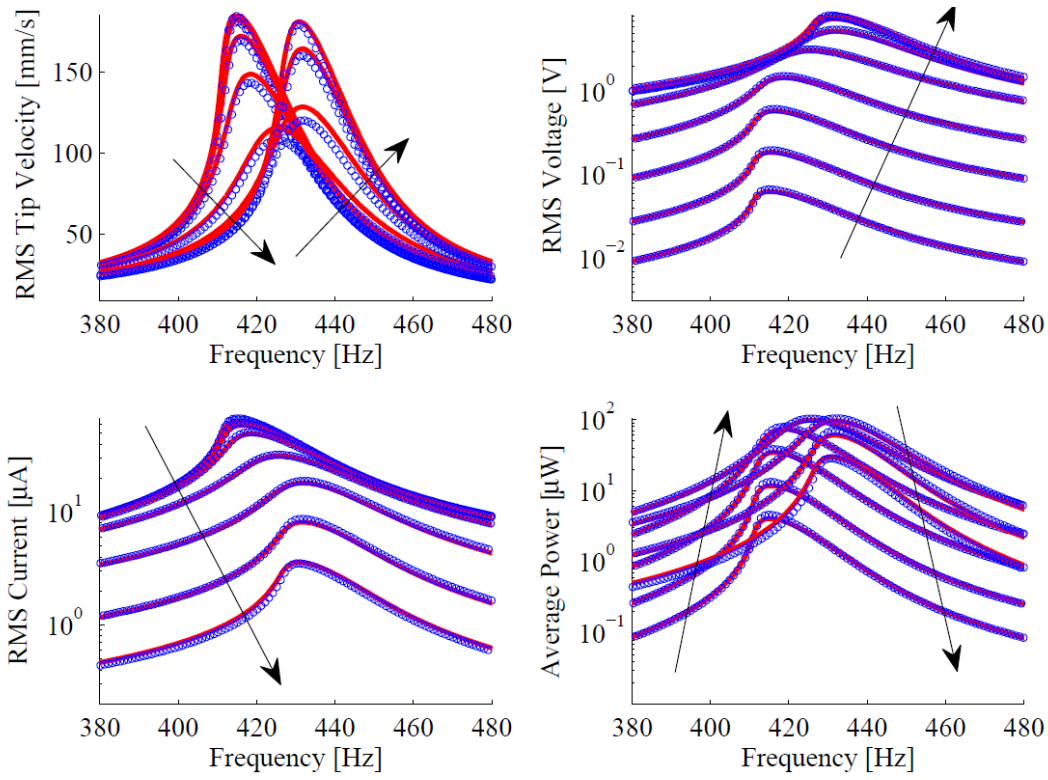

Figure 34: Resistor sweep energy harvesting test at $1.0g$ RMS base acceleration level for resistance values of 1kΩ, 3kΩ, 10kΩ, 30kΩ, 100kΩ, 300kΩ, 1MΩ, 3MΩ, and 10MΩ. Blue circles represent experimental data, and red curves represent model predictions. Arrows indicate direction of increasing load resistance.

magnitude increase in base acceleration results in a less than an order of magnitude increase in the responses. At $1g$ RMS base acceleration (Figure 34) the trend continues, with the short- and open-circuit resonant frequencies falling to 415 Hz and 430 Hz respectively, with increased damping.

The early appearance of a softening nonlinear behavior and its near linear increase with excitation level is evidence that a negative cubic stiffness alone improperly models the type of softening present in this class of piezoelectric cantilevers. A cubic stiffness nonlinearity yields a frequency correction that rises quadratically with response amplitude, whereas ferroelastic softening and dissipation provides a physical mechanism for the observed linear frequency correction and damping increase. The electromechanical coupling nonlinearity causes an additional resonant frequency shift that increases from short- to open-circuit conditions (low to high voltage). Importantly, the proposed model shows very strong agreement at the

low, medium, and high base acceleration levels.

4.5.3 Dynamic Actuation Experiments and Model Validation

Dynamic actuation tests are performed for voltages ranging from 0.01 to 10 volts and shown in Figure 35. This captures both the low voltage linear behavior and higher voltage behavior near the structural safety limits of the cantilever. These voltage levels result in electric fields well below the coercive field ($E_c = 12$ kV/cm for PZT-5A according to the manufacturer). However, resonant actuation above 10V amplitude in cantilever configuration is expected to result in mechanical failure of the stiff and brittle sample. The model uses the same parameters as shown in Table 6. The model and experiment show strong agreement over the entire voltage range, except in the cases where the consumed current is below the noise floor of the amplifier's current monitor output. Between the low (0.01 volts) and moderate (10 volts) voltage actuation tests, the bimorph displayed a decrease in resonant frequency from 429 Hz to 413 Hz, matching the behavior shown during the energy harvesting tests at short-circuit conditions. This is expected, because power amplifiers typically have very low output impedance, and the velocity response amplitudes for the corresponding dynamic actuation and energy harvesting experiments are of the same order of magnitude. As shown in Equation 115, during dynamic actuation, the electromechanical coupling nonlinearity appears as a correction to the forcing amplitude. At moderate response amplitudes, this can appear to have the same effect as another quadratic damping effect, making identification of the two parameters from the dynamic actuation tests alone difficult. However, as shown in Section 4.5.2, both effects are pronounced during the energy harvesting tests. The proposed model for dynamic actuation, using the same parameters as in the energy harvesting tests, shows strong agreement at all voltage levels reported in Figure 35.

4.5.4 Experimental Backbone Curve

As discussed previously in Section 4.1, quadratic and cubic nonlinearities model qualitatively different behaviors that both can be described as softening. To confirm that the type of geometrically linear, piezoelectric cantilever bimorph studied in this work is better modeled with quadratic nonlinearities than cubic nonlinearity alone, the backbone curve

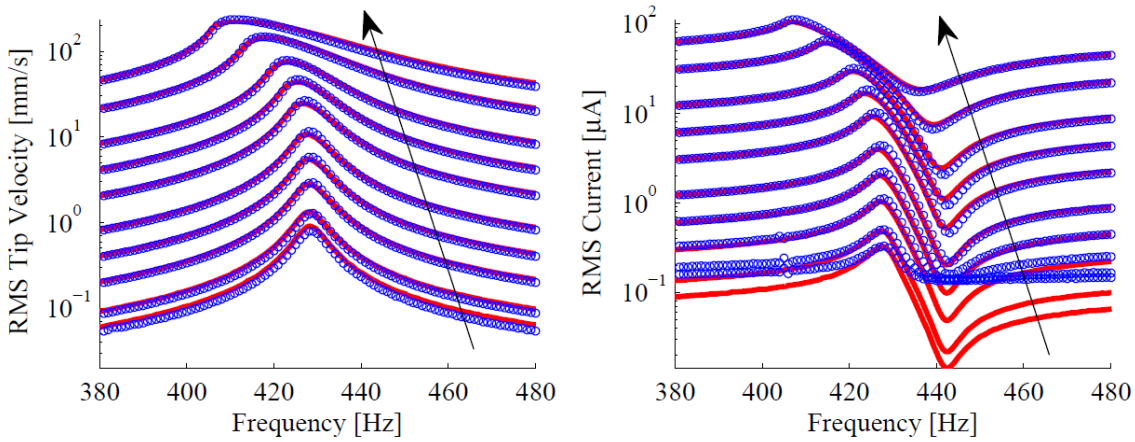

Figure 35: RMS tip velocity and RMS actuation current responses under dynamic actuation for voltage amplitudes of 0.01, 0.02, 0.05, 0.1, 0.2, 0.5, 1, 2, 5 and 10 volts. Blue circles represent experimental data, and red curves represent model predictions. Arrows indicate direction of increasing actuation voltage amplitude.

found from experimental data. Shown in Figure 36 are the open-circuit (10 MΩ) voltage responses during base acceleration tests and tip velocity responses during actuation tests for a broad range of excitation levels. For both the open circuit energy harvesting and dynamic actuation tests, the backbone curve is generated by fitting a second order polynomial to the peak response points. In both open circuit energy harvesting and dynamic actuation cases, the backbone curve is primarily linear, indicating that until very close to the safe operation limits of the cantilever, a quadratic stiffness model is satisfactory. More importantly, the backbone curve clearly does not cross the frequency axis at a right angle, which is characteristic of a purely cubic stiffness nonlinearity. Therefore, models in which quadratic terms vanish cannot accurately model observed behavior.

4.5.5 Quasi-Static Actuation Experiments

While the the proposed models and analysis pertains directly to the behavior of piezoelectric bimorph cantilevers near resonance, low frequency actuation tests were conducted to evaluate the model's performance for quasi-static, high voltage actuation. Low-frequency, off-resonant excitation allows for high voltage input levels that would damage the brittle sample structurally if applied near resonance. Using the same experimental apparatus as

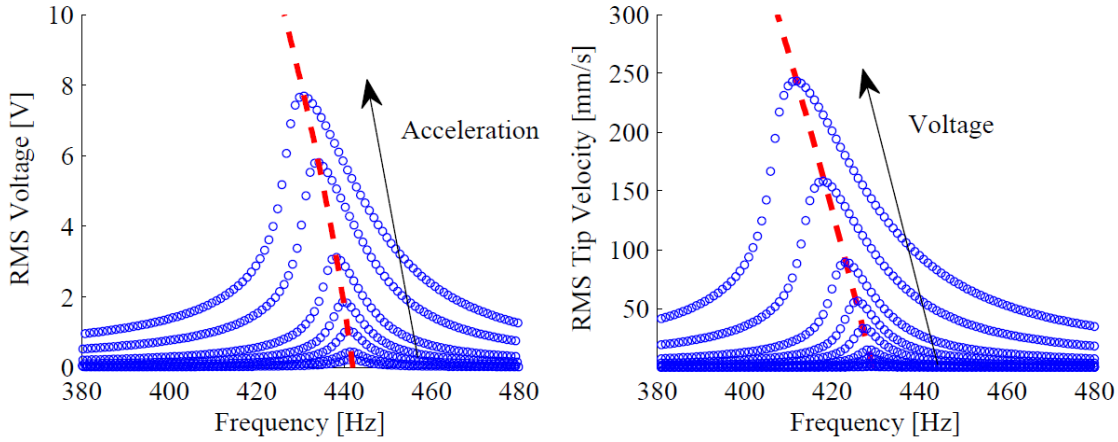

Figure 36: Open-circuit voltage responses for various base acceleration levels (left) and tip velocity responses to various excitation voltage levels (right). Experimental data is shown by blue circles, and the backbone curve is shown by the dashed red curve.

the dynamic actuation tests, the sample cantilever was actuated with a 10 Hz harmonic voltage with amplitudes ranging from 0.2 to 200 V. The highest voltage level of 200 V results in an electric field of 3.8 kV/cm for each piezoelectric layer (still below the coercive field of 12 kV/cm, but closer in terms of the order of magnitude as compared to the previous section). Figure 37 displays the the variation of tip displacement amplitude with actuation voltage amplitude. For actuation voltages of 20 V and below, the model accurately predicts the relationship between actuation voltage and displacement, which is governed by the ratio of electromechanical coupling to stiffness. For higher voltages exceeding the levels achievable in energy harvesting applications or resonant actuation, the model under predicts the deflection. For the 200 V test, the voltage is an order of magnitude higher than in the highest resonant actuation test, while the maximum deflections observed are on the same order of magnitude (∼0.1 mm). Therefore, the error is likely due to electromechanical coupling or excluded electric field nonlinearities rather than stiffness. A model that can more accurately predict both resonant and off-resonant actuation should include linear and quadratic stiffness terms and linear, quadratic, and cubic electromechanical coupling terms. High-field hysteretic effects[21] and resulting dissipation become important and should be included for excitations close to the coercive field.

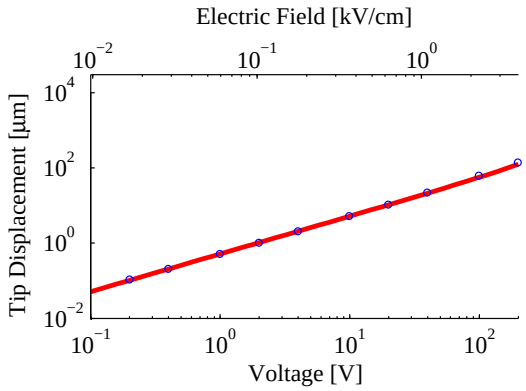

Figure 37: Quasistatic (10 Hz) tip displacement vs. actuation voltage amplitude. Experimental data is shown by blue circles, and model prediction is shown by the red curve.

4.6 Conclusions

An experimentally validated, nonlinear, nonconservative model has been proposed to describe the energy harvesting, sensing, and dynamic actuation behavior of piezoelectric cantilevers for a wide (low-to-moderately nonlinear) range of mechanical and electrical excitation levels. A set of governing partial differential equations was derived using Hamilton's principle. Those equations were spatially discretized for the fundamental bending mode, creating a lumped parameter model to be analyzed using the method of harmonic balance. The model showed excellent agreement to extensive experimental investigation of energy harvesting and dynamic actuation over the full range of structurally safe excitation levels of the brittle PZT-5A bimorph cantilever near resonance. The agreement of the model and experiment at all excitation levels is evidence that the dominant stiffness and electromechanical coupling nonlinearity apparent in certain piezoelectric structures is quadratic in nature. The backbone curves of both energy harvesting and actuation frequency responses are reported to be dominantly of first order for a broad range of mechanical and electrical excitation levels, in agreement with the experiments. While quadratic terms vanish during the analysis of a symmetric bimorph when examining polynomial electric enthalpy expansions in strain, an expansion form in strain amplitude retains those quadratic terms. Therefore, nonlinear effects associated with ferroelastic softening and dissipation should be given the priority in modeling of electroelastic nonlinearities in energy harvesting, sensing,

and actuation for low-to-moderately nonlinear response forms with electric fields well below the coercive field.

Chapter V

PZT-5A AND PZT-5H PARAMETER IDENTIFICATION

5.1 Introduction

This chapter contains an investigation of the nonlinear nonconservative dynamic behavior of bimorph piezoelectric cantilevers under low-to-high excitation levels with a focus on most popular soft piezoceramics: PZT-5A and PZT-5H. The unified mathematical framework using the method of harmonic balance derived and validated in Chapter 4 is used to identify nonlinear system parameters based on a set of rigorous experiments for different samples. Additionally, in-vacuo experiments are conducted verifying that observed nonlinear dissipation is internal to the structure rather than aerodynamic. Tests conducted of electrically inactive unpoled PZT-5A cantilevers verify that observed nonlinear behavior of soft piezoceramic materials is predominantly elastic and dissipative and nonlinearities in electromechanical coupling are negligible across the entire mechanical operating range. In Chapter 4, hysteretic, elastic, and electromechanical coupling nonlinearities were considered. A nonlinear electric enthalpy density expression along with a nonlinear structural dissipation term was validated, with the form:

$$H = \frac{1}{2}c_{11}S_1^2 + \frac{1}{3}c_{111}S_1^3\,\mathrm{sgn}(S_1) - e_{31}S_1E_3 - \frac{1}{2}e_{311}S_1^2\,\mathrm{sgn}(S_1)E_3 - \frac{1}{2}\epsilon_{33}E_3^2$$

$$U_{dis} \propto |S_1|^3.$$

This model was shown to correctly predict the observed behavior across a wide range of response amplitudes. It was also noted that the elastic and dissipative nonlinearities are dominant for a class of stiff piezoelectric bimorphs. In this chapter the values for the quadratic elasticity coefficient, c_{111}, and second order loss factor, γ_2, are extracted using a simplified model neglecting coupling nonlinearity due to e_{311}. This is done for the soft piezoelectric ceramics PZT-5A and PZT-5H from electromechanical resonant excitation experiments of piezoelectric bimorph cantilevers of various sizes. Photographs showing the cross section of the six bimorphs used in this study are shown in Figure 38.

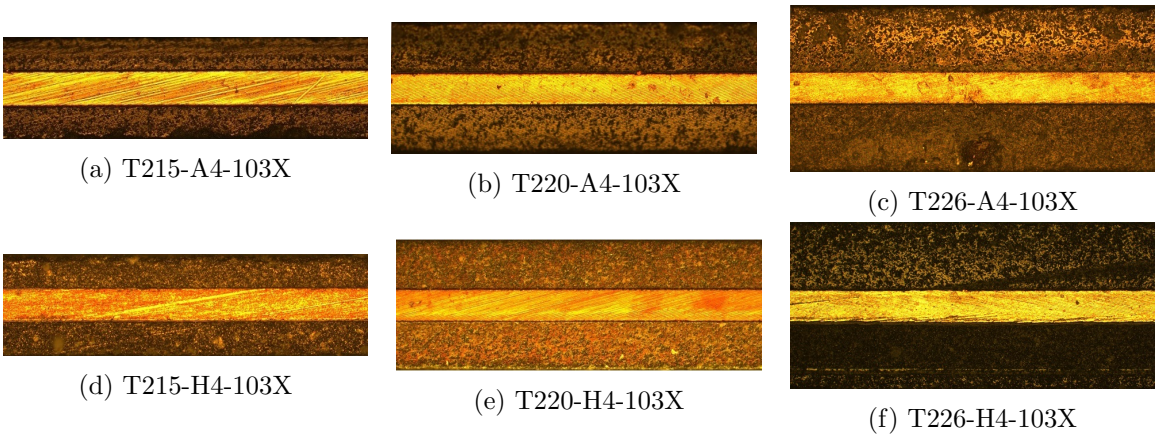

(a) T215-A4-103X (b) T220-A4-103X (c) T226-A4-103X

(d) T215-H4-103X (e) T220-H4-103X (f) T226-H4-103X

Figure 38: Side view photographs of six Piezo Systems, Inc. bimorphs. The brass substrate is the central light colored layer with darker PZT layers bonded above and below. For these samples, the number after "T2" refers to the overall thickness in thousandths of an inch, and the type of soft PZT (5A or 5H) is indicated by the following letter. The brass substrate is the same thickness for all samples.

5.2 Model Derivation

To obtain a lumped parameter model that can be used to identify nonlinear elasticity and dissipation parameters, the complex model derived in Chapter 4 can be simplified starting from:

$$m\ddot{x} + k_1^* x + k_2^* x^2 \operatorname{sgn}(x) - [\theta_1 + \theta_2 x \operatorname{sgn}(x)]\, v = -\bar{m}\ddot{z}(t) \tag{124}$$

$$C\dot{v} + i + [\theta_1 + \theta_2 x \operatorname{sgn}(x)]\, \dot{x} = 0. \tag{125}$$

As before, the governing ODEs must be real-valued. Also, if the governing equations are at least C^1 continuous, the method of harmonic balance (Appendices A and B) will be more numerically stable and efficient. Therefore the imaginary parts of the first and second order stiffness are replaced by velocity and velocity squared proportionate dissipation. Additionally, the second order electromechanical coupling parameterized by θ_2 is omitted, as this nonlinear effect was shown to be of lesser importance.

$$m\ddot{x} + b_1\dot{x} + b_2\dot{x}^2 \operatorname{sgn}(\dot{x}) + k_1 x + k_2 x^2 \operatorname{sgn}(x) - \theta_1 v = -\bar{m}\ddot{z}(t). \tag{126}$$

$$C\dot{v} + i + \theta_1 \dot{x} = 0. \tag{127}$$

As in the previous chapter, the underlying physics is the same, with internal mechanical dissipation. The velocity squared dissipation here is simply used for computational convenience, unlike the velocity squared dissipation modeled with the M-shaped oscillator and energy harvesters of Chapters 2 and 3, which physically represents aerodynamic drag. The first and second order stiffness coefficients, k_1 and k_2, are the real parts of the complex stiffness, k_1^* and k_2^*, respectively.

$$k_1 = \mathrm{Re}\{k_1^*\} \tag{128}$$

$$k_2 = \mathrm{Re}\{k_2^*\} \tag{129}$$

The first and second order dissipation coefficients, b_1 and b_2, are found by equating per cycle energy dissipation assuming harmonic motion and identifying multiplication by the imaginary unit, j, with a phase shift of $\pi/2$. Explicitly,

$$\begin{aligned} x(t) &= X\cos\left(\Omega t + \gamma\right) \\ jx(t) &= X\cos\left(\Omega t + \gamma + \frac{\pi}{2}\right) = -X\sin\left(\Omega t + \gamma\right) \\ \dot{x}(t) &= -\Omega X\sin\left(\Omega t + \gamma\right). \end{aligned} \tag{130}$$

The mechanical energy dissipated per cycle due to the first order damping term can then be written as:

$$\int_0^{2\pi/\Omega} \mathrm{Im}\{k_1^*\} jx\dot{x}dt = \int_0^{2\pi/\Omega} b_1\left(\dot{x}\right)^2 dt \tag{131}$$

Similarly, the mechanical energy dissipated per cycle due to the second order damping term can be written as:

$$\int_0^{2\pi/\Omega} \mathrm{Im}\{k_2^*\}\left(jx\right)^2 \mathrm{sgn}\left(jx\right)\dot{x}dt = \int_0^{2\pi/\Omega} b_2\left(\dot{x}\right)^3 \mathrm{sgn}\left(\dot{x}\right)dt. \tag{132}$$

After rearranging, the dissipation coefficients are therefore defined as:

$$b_1 = \frac{\mathrm{Im}\{k_1^*\}}{\Omega} \tag{133}$$

$$b_2 = \frac{\mathrm{Im}\{k_2^*\}}{\Omega^2} \tag{134}$$

Here, Ω is the dominant frequency of response. For the case of energy harvesting and sensing, the bimorph is subjected to a transverse base acceleration, $\ddot{z}(t)$, and the electrodes are

shunted by a load resistance, R. The coordinates, x and v, are the relative tip displacement of the cantilever and the voltage across the electrodes. Here, $\bar{m}$ and m are base acceleration forcing constant and the effective mass of the beam. The parameters, b_1, k_1, and θ, are the linear dissipation, stiffness, and electromechanical coupling constants, respectively. The parameters k_2, and b_2 represent the nonlinear stiffness and dissipation effects. The equivalent capacitance, C, is the value measured across the electrodes of the bimorph. Equations (126) and (127), which govern the dynamics of the piezoelectric beam when subjected to base motion and electrically terminated into a resistance, can easily be modified to describe actuation behavior when the voltage across the electrodes are prescribed. Base motion vanishes from the equations ($\ddot{z}(t) = 0$), forcing is due to the prescribed electrode voltage,$v(t)$, and the current through the cantilever becomes an unknown signal, $i(t)$. This yields the following set of ODEs governing actuation behavior:

$$m\ddot{x} + b_1\dot{x} + b_2\dot{x}^2\,\mathrm{sgn}(\dot{x}) + k_1 x + k_2 x^2\,\mathrm{sgn}(x) = \theta_1 v(t) \tag{135}$$

$$C\dot{v}(t) + i + \theta_1\dot{x} = 0 \tag{136}$$

5.3 Harmonic Balance Analysis

The method of harmonic balance has been used extensively to analyze periodic solutions of nonlinear ordinary differential equations. A Fourier series solution is assumed, replacing the ordinary differential equations with algebraic equations. The error of the approximate solution is minimized in the Galerkin method sense. The resulting system of algebraic equations is solved iteratively, with a method such as the Newton-Raphson method. For illustration, a single term harmonic balance solution is shown, although five harmonics are used in the analysis. For base motion excitation, base acceleration is taken to be harmonic with constant amplitude, i.e.

$$\ddot{z}(t) = A\cos(\Omega t) \tag{137}$$

The unknown steady-state tip displacement and voltage responses are assumed to be of the form:

$$x(t) = X_1 \cos(\Omega t) + X_2 \sin(\Omega t)$$
$$v(t) = V_1 \cos(\Omega t) + V_2 \sin(\Omega t) \tag{138}$$

The amplitude of x is given by $X = \sqrt{X_1^2 + X_2^2}$. Subsitution of Equations (137) and (138) into Equations (126) and (127) and application of the harmonic balance method yields the following set of algebraic equations in X_1, X_2, V_1, and V_2:

$$\begin{aligned}
-m\Omega^2 X_1 + \left(b_1 + \frac{8}{3\pi} b_2 \Omega X\right) \Omega X_2 + \left(k_1 + \frac{8}{3\pi} k_2 X\right) X_1 - \theta_1 V_1 + \bar{m} A = 0 \\
-m\Omega^2 X_2 - \left(b_1 + \frac{8}{3\pi} b_2 \Omega X\right) \Omega X_1 + \left(k_1 + \frac{8}{3\pi} k_2 X\right) X_2 - \theta_1 V_2 = 0 \\
C\Omega V_2 + \frac{1}{R} V_1 + \theta \Omega X_2 = 0 \\
C\Omega V_1 - \frac{1}{R} V_2 + \theta \Omega X_1 = 0.
\end{aligned} \tag{139}$$

For actuation due to a prescribed electrode voltage, the voltage is assumed to have the form:

$$v(t) = V \cos(\Omega t) \tag{140}$$

The unknown steady-state tip displacement and voltage responses are assumed to be of the form:

$$x(t) = X_1 \cos(\Omega t) + X_2 \sin(\Omega t)$$
$$i(t) = I_1 \cos(\Omega t) + I_2 \sin(\Omega t) \tag{141}$$

The algebraic equations governing the response amplitudes for harmonic voltage actuation are therefore:

$$\begin{aligned}
-m\Omega^2 X_1 + \left(b_1 + \frac{8}{3\pi} b_2 \Omega X\right) \Omega X_2 + \left(k_1 + \frac{8}{3\pi} k_2 X\right) X_1 - \theta V = 0 \\
-m\Omega^2 X_2 - \left(b_1 + \frac{8}{3\pi} b_2 \Omega X\right) \Omega X_1 + \left(k_1 + \frac{8}{3\pi} k_2 X\right) X_2 = 0 \\
I_1 + \theta \Omega X_2 = 0 \\
C\Omega V - I_2 + \theta \Omega X_1 = 0.
\end{aligned} \tag{142}$$

5.4 Experimental Setup

The test samples consist of brass-reinforced PZT-5A and PZT-5H piezoelectric cantilever bimorphs (manufactured Piezo Systems, Inc.) secured in a custom fixture. Microscope photographs showing the central brass substrate and upper and lower piezoelectric laminates is shown in Figure 38. Geometric and material properties of the bimorph can be found in Table 7 (the linear material parameters are in agreement with standard data[34] and manufacturer's data). For base excitation, the fixture is mounted to a shaker (Brüel and Kjær Type 4809). Forward and reverse frequency sweeps at constant base acceleration amplitude are conducted using a vibration control system (APS Dynamics, Inc. VCS201) and accelerometer for acceleration feedback (Kistler AG Type 8636C5). The voltage across the cantilever electrodes are shunted across a load resistance box (IET Labs, Inc. RS-201W). Tip velocity measurements are made using a laser Doppler vibrometer (Polytec, Inc. OFV-505) and controller (Polytec, Inc. OFV-5000). Data is collected using National Instruments NI 9215 and NI 9223 data acquisition units. A schematic representation of the experimental setup is shown in Chapter 4. During dynamic actuation experiments, the fixture is mounted to a rigid support. The actuation voltage signal is generated by a National Instruments NI USB-4431 and amplified using a power amplifier (Trek, Inc. Model 2220). Output voltage and current data are collected from the amplifier, as well as tip velocity measurements from the laser-Doppler vibrometer and recorded using the NI USB-4431.

5.5 Base Acceleration Experiments

Energy harvesting experiments consist of frequency sweep tests at seven constant acceleration levels ranging from $0.01g$ RMS to $2.0g$ RMS. Tests at each acceleration level were repeated for nine load resistance values ranging from 1kΩ to 10MΩ, which cover a broad range between short- and open-circuit conditions. For each cantilever, the maximum base acceleration amplitude is chosen to keep the cantilever tip deflection within the safe limits provided by the manufacturer. Plots of representative experimental data are shown in Figures 39 and 40.

As shown in Figure 39, the model and experiment show excellent correlation at a low

Table 7: Material and geometric parameters for brass-reinforced PZT bimorph cantilevers (Piezo Systems, Inc.).

(a) Material parameters

PZT density	ρ_p	7800	kg	
PZT elastic modulus	c_{11}	66	GPa	(PZT-5A)
		62	GPa	(PZT-5H)
Piezoelectric	e_{31}	-12.3	C/m^2	(PZT-5A)
coupling		-16.2	C/m^2	(PZT-5H)
Permitivity	ϵ_{33}	14.8	nF/m	(PZT-5A)
		23.7	nF/m	(PZT-5H)
Brass density	ρ_s	8500	kg	
Brass elastic modulus	c_s	100	GPa	

(b) Geometric parameters

Overhang length	l	26.6	mm	
Total length	l_e	31.8	mm	
Width	b	3.16	mm	
PZT thickness (each)	h_p	0.127	mm	(T215...)
		0.191	mm	(T220...)
		0.267	mm	(T226...)
Brass thickness	h_s	0.127	mm	

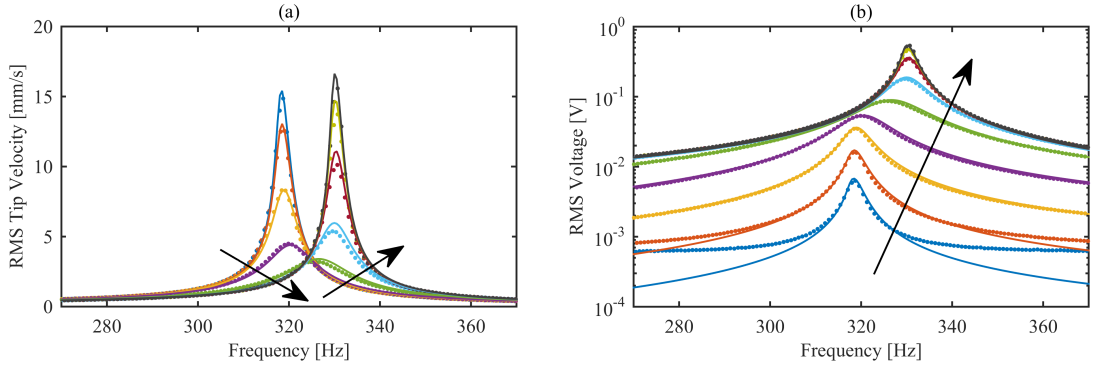

Figure 39: Representative low amplitude ($0.01g$ RMS) test data and model fit using the medium thickness PZT-5H cantilever (T220-H4-103X). Experimental data shown with markers and model predictions shown with curves. Arrows indicate trend of increasing load resistance.

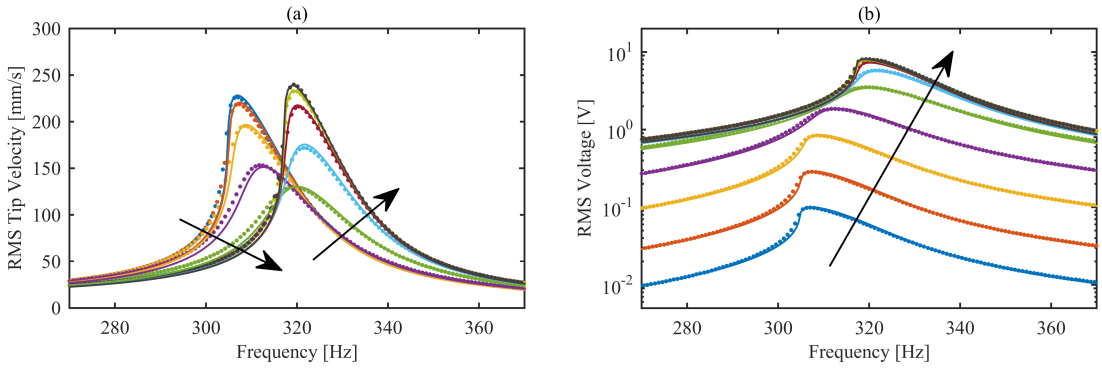

Figure 40: Representative high amplitude ($0.5g$ RMS) test data and model fit using the medium thickness PZT-5H cantilever (T220-H4-103X). Experimental data shown with markers and model predictions shown with curves. Arrows indicate trend of increasing load resistance.

base acceleration level, where linear behavior is expected. The model and experiment only disagree for the voltage curves, when the harvester voltage is below the noise floor of the data acquisition unit, which is an experimental limitation. Agreement of the model and experiment in the linear behavior regime is important, but expected, as high-fidelity models for the linear behavior of piezoelectric cantilevers are readily available [27, 32, 34] to predict the linear electroelastic dynamics using the relevant geometric and material properties in Table 7. Nonlinear behavior is readily apparent at $0.5g$ RMS, as shown in Figure 40, and is noticeable even at moderate excitation levels. Importantly, the model correctly predicts nonlinear stiffness trends, and so can be used to extract the quadratic elastic modulus, c_{111}.

5.6 Voltage Actuation Experiments

Resonant actuation tests are performed for voltage amplitudes ranging from 0.01 to 10 volts, with the upper limit again chosen to stay within the operating limits of each sample. This range captures both the low voltage linear behavior and nonlinear higher voltage behavior. Representative results are shown in Figure 41. The model and experiment show strong agreement over the entire voltage range, except in the cases where the consumed current is below the noise floor of the amplifier's current monitor output. There is also a discrepancy between the model predictions and experimental results for the current consumed by the

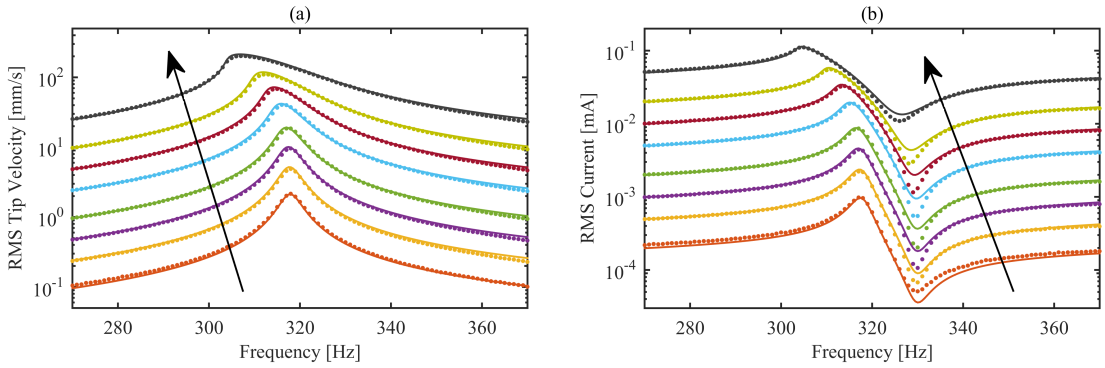

Figure 41: Representative voltage actuation test data and model fit using the medium thickness PZT-5H cantilever (T220-H4-103X). Experimental data shown with markers and model predictions shown with curves. Arrows indicate trend of increasing actuation voltage amplitude.

Table 8: Identified first order dissipation coefficients (γ_1) for six PZT bimorphs.

	PZT Layer Thickness, h_p			
Material	0.127 mm	0.191 mm	0.267 mm	Average
PZT-5A	0.013	0.013	0.014	0.013
PZT-5H	0.015	0.015	0.016	0.015

cantilever at frequencies around the admittance antiresonance frequency. This is likely caused by the power amplifier acting as a non-ideal voltage source, as the voltage output from the amplifier dipped significantly.

5.7 Identified Quadratic Elasticity Coefficients

The identified quadratic elasticity coefficients are summarized in Table 9. The extracted values of the quadratic elasticity coefficient, c_{111}, show a few characteristics. First, the

Table 9: Identified quadratic elasticity coefficients (c_{111}) for six PZT bimorphs.

	PZT Layer Thickness, h_p			
Material	0.127 mm	0.191 mm	0.267 mm	Average
PZT-5A	-65 TPa	-57 TPa	-59 TPa	-60 TPa
PZT-5H	-52 TPa	-45 TPa	-40 TPa	-46 TPa

Table 10: Identified second order dissipation coefficients (γ_2) for six PZT bimorphs.

	PZT Layer Thickness, h_p			
Material	0.127 mm	0.191 mm	0.267 mm	Average
PZT-5A	0.30	0.38	0.36	0.35
PZT-5H	0.30	0.35	0.36	0.34

values are on the order of TPa. The types of PZT bimorphs tested in this work can safely withstand maximum strains of approximately 1 mε, or 0.001. At that maximum level, the quadratic correction to the elastic modulus is on the order of GPa, so it is unsurprising that the nonlinear behavior is apparent. Second, as with the linear elastic modulus, c_{11}, the quadratic elasticity coefficient is greater for PZT-5A than for PZT-5H. Third, the identified quadratic elasticity coefficients for both PZT-5A and PZT-5H decrease with the thickness of the piezoelectric layers. This is an indication of additional unmodeled effects. When modeling piezoelectric structures, it is already typical to update the accepted material parameters to better match experiments, because elastic moduli and piezoelectric coupling values can vary significantly between manufacturers and batches. The values presented here are therefore a similarly useful as guidelines for the modeling of nonlinear device behavior.

5.8 In-Vacuo Cantilever Bimorph Behavior

Mechanical dissipation is an inherently nonlinear phenomenon, and can arise from a variety of sources. It is therefore often difficult to claim with any certainty what the particular cause of the dissipation is. In this analysis, the observed second order damping is attributed to internal dissipation in the piezoelectric material approximately described by an effective mechanical loss factor that grows linearly with strain amplitude. Oftentimes observed nonlinear damping is attributed to aerodynamic drag caused by the vibrating structure interacting with the surrounding air. By examining the drag equation and the ideal gas law one can see that damping forces due to aerodynamic drag will be proportional to the pressure of the air surrounding a structure, with other conditions held constant. Therefore, if aerodynamic drag is the dominant source of second order dissipation, there should be a large difference between the velocity response behavior between in air and in-vacuo tests,

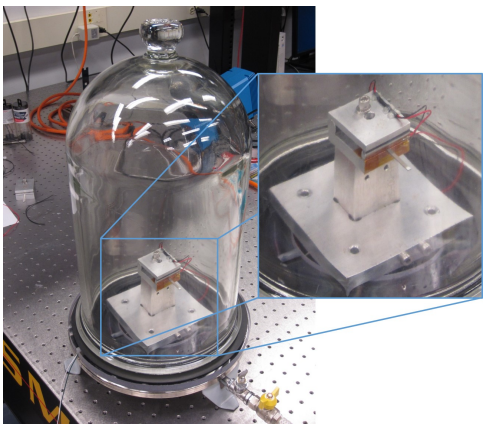

(a) Vacuum setup

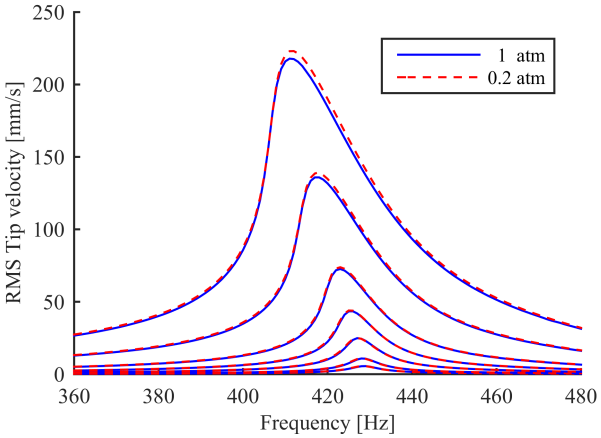

(b) Vacuum results

Figure 42: In-vacuo voltage actuation test setup. Clamped PZT bimorph cantilever beam is fixed to a rigid base placed on a vacuum chamber stand under a bell jar. Wires supplying power from the amplifier pass through a custom gasket. Inset photograph shows the cantilever, clamp, and base. Experimental in-air and in-vacuo voltage actuation test data using the large thickness PZT-5A cantilever (T226-A4-103X). In air tests were conducted at 1 atm and are shown by blue curves. In-vacuo tests were conducted at 0.2 atm and are shown by dashed red curves. Actuation voltage amplitudes range from 0.01 to 10 volts.

especially at the largest actuation voltage levels.

To investigate what the relative contributions internal dissipation and aerodynamic effects make to the overall nonlinear damping, a dynamic actuation experiment as described previously was conducted both in air and in vacuum. As shown in Figure 42a, the rigidly-fixtured cantilever bimorph sample was placed under a vacuum bell jar. As in Section 5.6, frequency sweep experiments are performed for various actuation voltages ranging from 0.01 to 10 volts. Figure 42b shows a comparison of the RMS tip velocity response behavior for the thickest PZT-5A sample (T226-A4-103X) both in air at atmospheric pressure as well as in a partial vacuum (0.2 atm absolute pressure). The experimental results show, however, that the peak response amplitude in the vacuum test at the highest voltage actuation level of 10 volts is only 2.4% higher than the peak response amplitude at atmospheric pressure. For comparison, a linear model would predict a response amplitude more than double that of both the in air and in-vacuo tests. For the piezoelectric cantilevers studied here and ones of similar geometries, it is therefore acceptable to consider nonlinear damping due to aerodynamic drag negligible. Doing so will lead to only slightly inflated estimates of internal

Table 11: Material and geometric parameters for unpoled PZT-5A cantilevers (APC International, Ltd.).

(a) Material parameters

Density	ρ_p	7600	kg
Elastic modulus	c_{11}	58.5	GPa

(b) Geometric parameters

Overhang length	l	35	mm
Width	b	3	mm
Thickness	$2h_p$	0.50	mm
		0.60	mm
		0.70	mm

nonlinear dissipation parameters.

5.9 Unpoled PZT Cantilever Behavior

In recent work on the nonlinear resonant behavior of PZT-based structures, there has been some debate on the role of nonlinear electromechanical coupling. Some ignore it and treat only linear electromechanical coupling, some find that it is non-negligible, and in some cases it is claimed that it is the key contributor to observed nonlinear behavior. As detailed in this chapter and Chapter 4, good evidence has been found of the notion that the main contributors to the observed nonlinear resonant behavior of geometrically linear PZT structures is nonlinear elasticity and dissipation. To further test this hypothesis, base excitation experiments similar to the ones previously described were conducted on a set of *unpoled* PZT-5A single layer cantilever beams. The samples were produced by a different manufacturer (APC International, Ltd.) than the poled bimorph cantilevers, and so the exact formulation of PZT-5A is different. Table 11 contains the given properties of the tested unpoled samples.

As the samples consist of a single PZT layer (i.e. the substrate layer thickness, $h_s = 0$), the thickness is reported as $2h_p$ to match the model given above. Along with setting all electrical and electromechanical parameters to zero, the model derived for poled piezoelectric bimorphs may be used. Additionally, the manufacturer provides typical values for the elastic parameters ($c_{11} = 63$ GPa and $c_{33} = 54$ GPa) for poled material. For modeling purposes, the elastic modulus for unpoled material is taken to be the mean of these two values. As done previously, three different sample thicknesses were tested for verification purposes.

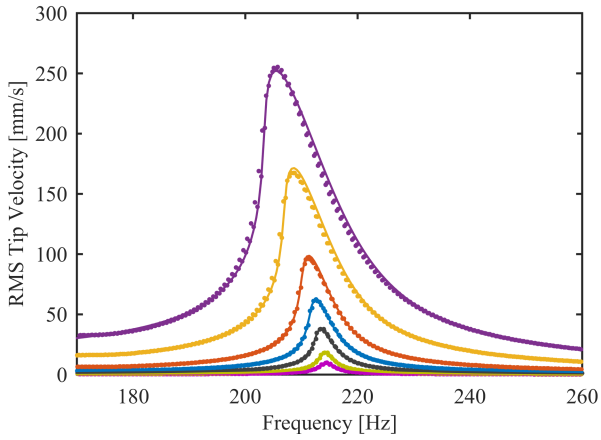

Figure 43: Representative base acceleration test data for the 0.60 mm thickness unpoled PZT-5A cantilever. Experimental data shown with markers and model predictions shown with curves. Base acceleration levels range from 0.01 to $1g$ RMS.

The experimental apparatus is also identical to that of the base excitation experiments of Section 5.5 with the absence of any voltage measurements. Representative experimental tip velocity response data and model predictions are shown in Figure 43 for the 0.60 mm thickness sample to base acceleration levels ranging from 0.01 to $1g$ RMS. This upper limit for the excitation level was chosen to be comparable to the tests of the poled PZT bimorphs and to keep the cantilever in safe operating conditions. Unlike previous tests, the maximum safe operating conditions were determined experimentally instead of from manufacturers recommendations. For each sample thickness, frequency sweep tests near resonance were conducted at progressively higher base acceleration amplitudes until the sample broke. For the 0.60 mm thick samples, catastrophic brittle fracture occurred during tests at $3g$ RMS with an RMS tip velocity of approximately 800 mm/s. A maximum base acceleration amplitude of $1g$ RMS therefore represents a safety factor against failure due to brittle fracture of approximately three.

As with the poled PZT bimorph samples, the simulated frequency response curves for the unpoled PZT-5A cantilevers match the experimental data extremely well, with proper fitting of nonlinear parameters summarized in Table 12. The extracted nonlinear elasticity and dissipation parameters agree quite well with those found for the poled PZT bimorph cantilevers, despite coming from different manufacturers. For the unpoled PZT-5A samples,

Table 12: Identified parameters for unpoled PZT-5A cantilevers.

	Thickness, $2h_p$			
Parameter	0.50 mm	0.60 mm	0.70 mm	Average
γ_1	0.016	0.009	0.009	0.011
c_{111}	-41 TPa	-40 TPa	-40 TPa	-40 TPa
γ_2	0.29	0.35	0.33	0.32

the quadratic elasticity coefficient, c_{111}, was found to be lower than that of the poled samples. The various second order elasticity coefficients may be affected by poling similarly to the linear coefficients.

5.10 Conclusions

An experimentally validated, nonlinear model has been used to extract the nonlinear elastic properties of soft piezoelectric material from experiments involving the resonant response of piezoelectric cantilever bimorphs. Samples made from PZT-5A and PZT-5H layers of three different thicknesses each were subjected to base acceleration and dynamic voltage actuation testing ranging from the linear regime to close to the failure limits of the device, where nonlinear behavior is strong. A single second order correction to the elastic modulus parameterized by a quadratic elasticity coefficient has been shown to well-approximate the nonlinear electroelastic behavior of a class of geometrically stuff piezoelectrically coupled beams. Values of the quadratic elasticity coefficent, c_{111} of between -60 and -65 TPa for PZT-5A and between -40 and -55 TPa for PZT-5H can be used as guidelines for the accurate modeling of these materials. Additionally, the hypothesis that observed nonlinear dissipation is due to internal mechanisms rather than aerodynamic drag was verified by conducting in-vacuo experiments. The success of the proposed model to predict behavior and extract parameters of structures made with both poled and unpoled piezoceramic supports findings that the dominant nonlinear resonant behavior is due to elastic and mechanically dissipative effects rather than due to nonlinearities in electromechanical coupling.

Chapter VI

COUPLED MATERIAL AND AC-DC CONVERSION NONLINEARITIES

6.1 Introduction

In this chapter, a lumped parameter model of the nonlinear resonant behavior of a vibration energy harvester connected to a bridge rectifier, filter capacitor, and load resistor is derived. The energy harvester design of interest is a piezoelectric bimorph cantilever with piezoelectric layers connected in series. The mechanical nonlinear behavior is studied in Chapters 4 and 5.

The problem is explored first to characterize mechanical nonlinearities by exploring the AC input (base excitation) and AC output (voltage across the load) problem in the presence of a resistive load. Linear model parameters are identified from experiments in the linear regime. Material and dissipative nonlinearities are identified from nonlinear tests at different excitation levels. Having characterized the mechanical nonlinearities, the AC input-DC output case is studied. For the multiphysics equations of the fully coupled nonlinear system, a harmonic balance solution is applied to analyze the mechanically and electrically nonlinear system dynamics at different excitation levels. Experimental validations are presented.

6.2 Model Derivation

The focus of this work is on the modeling and simulation of stiff piezoelectric bimorph cantilever beams used for energy harvesting purposes. As shown previously (Chapter 4), resonant behavior near a single resonant frequency can be accurately modeled as a single degree of freedom electromechanically coupled oscillator with nonlinearities in mechanical dissipation and stiffness. A full treatment of the derivation of a electromechanical model of the energy harvester can be found in Chapters 4 and 5.

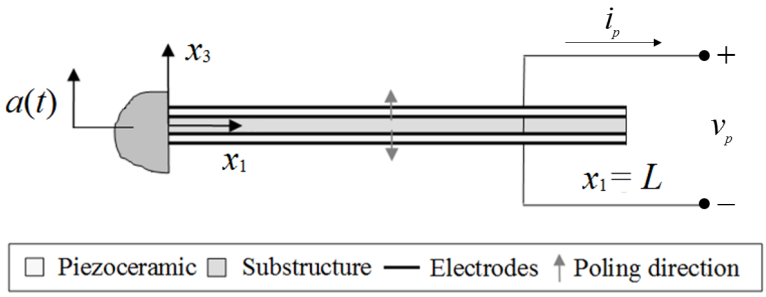

Figure 44: Diagram of piezoelectric bimorph cantilever vibration energy harvester.

6.2.1 Piezoelectric Bimorph Governing Equations

From previous work modeling the dynamics of a piezoelectric bimorph cantilever, the differential equations governing the mechanical and electrical behavior of the energy harvester excited near a resonance frequency are given by:

$$m\ddot{x} + b_1\dot{x} + b_2\dot{x}^2\,\mathrm{sgn}(\dot{x}) + k_1 x + k_2 x^2\,\mathrm{sgn}(x) - \theta v_p = -\bar{m}a(t), \tag{143}$$

$$C_p\dot{v}_p + i_p + \theta\dot{x} = 0, \tag{144}$$

where x is the relative transverse displacement of the beam tip with respect to the base, v_p is the electrode voltage, i_p is the electrical current flowing out of the energy harvester, and $a(t)$ is the prescribed base acceleration. The effective beam mass, m, first and second order dissipation coefficients, b_1 and b_2, first and second order stiffness coefficients, k_1 and k_2, electromechanical coupling parameter, θ, forcing mass, $\bar{m}$, and capacitance, C_p, are defined in the same way as in Chapters 4 and 5.

This model includes nonlinearities in the mechanical dissipative and restoring forces (due to b_2 and k_2), but assumes linear electromechanical coupling behavior. As was shown in Chapter 4, electromechanical coupling nonlinearities are less important than the dominant mechanical nonlinearities. To complete the model, a constitutive relationship between the electrode voltage, v_p, and the harvester output current, i_p, must be defined. As in previous sections, the harvester electrodes may be shunted across a load impedance, yielding a linear dynamic constitutive relationship. This allows for the mechanical nonlinearities to be identified and quantified separately from any circuit nonlinearities. For practical use, however, the alternating current produced by the piezoelectric cantilever must be converted to direct

current. This process cannot be implemented with linear circuit elements, and so will yield a nonlinear constitutive relationship. The following sections deal with modeling the energy harvester connected first to a simple load resistance to identify the mechanical dissipative and elastic nonlinearities, and secondly connected to a practical harvesting circuit using a full-wave diode bridge for rectification.

6.3 Harvester Connected to a Load Resistance

To study and quantify the mechanical dissipative and elastic nonlinearities contributing to the vibratory behavior of the energy harvester, the electrodes are shunted across a load resistance. This results in the simplest possible constitutive relationship between electrode voltage and current, namely the algebraic equation given by Ohm's law:

$$v_p = Ri_p. \tag{145}$$

Choosing the electrode voltage to be the electrical state variable and substituting into the above current balance equation:

$$m\ddot{x} + b_1\dot{x} + b_2\dot{x}^2\,\mathrm{sgn}(\dot{x}) + k_1x + k_2x^2\,\mathrm{sgn}(x) - \theta v_p = -\bar{m}a(t) \tag{146}$$

$$C_p\dot{v}_p + \frac{1}{R}v_p + \theta\dot{x} = 0. \tag{147}$$

At low response amplitudes, the dissipative and elastic nonlinearities of this model will disappear, and the steady state behavior of the system can be found using normal linear systems theory. Derivations of steady state solutions in the linear regime will be given first followed by preparation of the equations for solution by the method of harmonic balance.

6.3.1 Linear Solution

If response amplitudes are restricted to be small, second order terms in the governing equations can be neglected yielding the following linear model for a piezoelectric bimorph cantilever excited by transverse base acceleration with electrodes shunted across a load resistance:

$$m\ddot{x} + b_1\dot{x} + k_1x - \theta v_p = -\bar{m}a(t) \tag{148}$$

$$C_p\dot{v}_p + \frac{1}{R}v_p + \theta\dot{x} = 0. \tag{149}$$

To find the complex frequency response functions, which describe the amplitude gain and phase shift of the response signals to harmonic excitation, the solutions are assumed to be of the form,

$$x(t) = Xe^{j\Omega t} \tag{150}$$

$$v_p(t) = V_p e^{j\Omega t} \tag{151}$$

$$a(t) = Ae^{j\Omega t}. \tag{152}$$

Substituting the assumed solutions into the linear system and solving for the complex amplitude ratios yields the solutions for the relative displacement and voltage responses for the vibration harvester connected to a load resistance.

$$\frac{X}{A} = \frac{-\bar{m}(j\Omega RC_p + 1)}{(-\Omega^2 m + j\Omega b_1 + k_1)(j\Omega RC_p + 1) + j\Omega R\theta^2} \tag{153}$$

$$\frac{V_p}{A} = \frac{j\Omega \bar{m} R\theta}{(-\Omega^2 m + j\Omega b_1 + k_1)(j\Omega RC_p + 1) + j\Omega R\theta^2} \tag{154}$$

If dielectric losses are non-negligible and the dielectric loss tangent, $\tan\delta_e$, of the piezoelectric material is provided by the manufacturer, the capacitance, C_p, may be replaced by a complex capacitance, $\tilde{C}_p$, defined by:

$$\tilde{C}_p = C_p\left(1 - j\tan\delta_e\right). \tag{155}$$

Similarly, if the harvester electrodes are shunted across a more complicated linear circuit, the load resistance, R, need only be replaced by a general complex load impedance, $Z(\Omega)$. Additionally, the kinematic response signal measured in experiments is the cantilever tip velocity in the inertial frame rather than relative tip displacement. Modifying the frequency response functions to include dielectric losses and correspond to experimentally measured signals yields the following expressions, with $\dot{X}_I$ representing the complex velocity amplitude measured in the inertial frame.

$$\frac{\dot{X}_I}{A} = \frac{-j\Omega\bar{m}(j\Omega R\tilde{C}_p + 1)}{(-\Omega^2 m + j\Omega b_1 + k_1)(j\Omega R\tilde{C}_p + 1) + j\Omega R\theta^2} + \frac{1}{j\Omega} \tag{156}$$

$$\frac{V_p}{A} = \frac{j\Omega\bar{m}R\theta}{(-\Omega^2 m + j\Omega b_1 + k_1)(j\Omega R\tilde{C}_p + 1) + j\Omega R\theta^2} \tag{157}$$

By comparing these to experimentally generated frequency response functions, the quality of first principles predictions can be evaluated, and model parameters can be updated.

6.3.2 Nonlinear Mechanical, Linear Electrical Modeling

To study the steady state behavior of the governing equations for large response amplitudes, the second order dissipation and stiffness terms are retained, and the excitation due to the base acceleration is restricted to be periodic. As is commonly done, the case of pure harmonic excitation is examined for simplicity. Because the systems is nonlinear, superposition no longer holds, and therefore the governing equations must be real valued. To include dielectric loss, the imaginary portion of the current flowing through the capacitor due to the loss tangent is recognized to act like an additional parasitic resistance in parallel with the load resistance. The governing equations for the nonlinear behavior of a piezoelectric bimorph excited by a harmonic base acceleration with electrodes connected to a load resistance can therefore be expressed as:

$$m\ddot{x} + b_1\dot{x} + b_2\dot{x}^2\,\mathrm{sgn}(\dot{x}) + k_1 x + k_2 x^2\,\mathrm{sgn}(x) - \theta v_p = -\bar{m}A\cos(\Omega t) \tag{158}$$

$$C_p\dot{v}_p + \left(\Omega C_p \tan\delta_e + \frac{1}{R}\right) v_p + \theta\dot{x} = 0 \tag{159}$$

As there is no closed form solution to this system of nonlinear ordinary differential equations, approximate solutions are sought. Additionally, analytical approximate solutions are only possible when strong simplifying assumptions are made (i.e. the response consists of a single harmonic.) As shown in Chapter 2, these simplifying assumptions can lead to erroneous model predictions when applied to practical problems. It is therefore preferable to find approximate solutions numerically. Nonlinear ODEs can be simulated using numerical integrators, but the presence of transient responses can make numerical integrators slow to find steady state behavior, especially when the system is lightly damped. Numerical methods that find periodic steady state solutions directly are therefore preferable. To prepare the governing equations for numerical simulation of any kind, it is necessary to put the system in state space form and is advantageous to nondimensionalize it. To this end, the nondimensional state space system is defined as:

$$\mathbf{u}' = \mathbf{f}(\tau, \mathbf{u}), \tag{160}$$

where $\mathbf{u}$ is the nondimensional state vector, and $()'$ denotes the derivative with respect to nondimensional time, τ. The system is nondimensionalized by defining characteristic time, length, and voltage scales (T_c, L_c, and V_c) accordingly.

$$\begin{aligned} t &= T_c\tau \\ x &= L_c u_1 \\ \dot{x} &= \frac{L_c}{T_c}u_2 \\ \ddot{x} &= \frac{L_c}{T_c^2}u_2' \\ v_p &= V_c u_3 \\ \dot{v}_p &= \frac{V_c}{T_c}u_3' \end{aligned} \tag{161}$$

Substituting these into the governing equations yields:

$$\begin{aligned} m\frac{L_c}{T_c^2}u_2' + b_1\frac{L_c}{T_c}u_2 + b_2\left(\frac{L_c}{T_c}u_2\right)^2\operatorname{sgn}(u_2) + k_1L_cu_1 + k_2\left(L_cu_1\right)^2\operatorname{sgn}(u_1) \\ - \theta V_c u_3 = -\bar{m}A\cos(\Omega T_c\tau) \end{aligned} \tag{162}$$

$$C_p\frac{V_c}{T_c}u_3' + \left(\Omega C_p\tan\delta_e + \frac{1}{R}\right)V_cu_3 + \theta\frac{L_c}{T_c}u_2 = 0, \tag{163}$$

which can be rearranged into state space form to give:

$$\begin{aligned} f_1 = u_1' &= \ u_2 \\ f_2 = u_2' &= -\left(\frac{k_1T_c^2}{m}\right)u_1 - \left(\frac{k_2L_cT_c^2}{m}\right)u_1^2\operatorname{sgn}(u_1) - \left(\frac{b_1T_c}{m}\right)u_2 \\ &\quad - \left(\frac{b_2L_c}{m}\right)u_2^2\operatorname{sgn}(u_2) + \left(\frac{\theta V_cT_c^2}{mL_c}\right)u_3 - \left(\frac{\bar{m}AT_c^2}{mL_c}\right)\cos(\Omega T_c\tau) \\ f_3 = u_3' &= -\left(\frac{\theta L_c}{C_pV_c}\right)u_2 - \left(\Omega T_c\tan\delta_e + \frac{T_c}{RC_p}\right)u_3 \end{aligned} \tag{164}$$

For the method of harmonic the Jacobian matrix of the system is required, whose elements are defined by the expression:

$$J_{ij} = \frac{\partial f_i}{\partial u_j}. \tag{165}$$

6.4 Harvester Connected to a Rectification Circuit

For practical energy harvesting purposes, a stable DC output is required to power an electronic device. Since a vibration energy harvester naturally produces AC, the output current

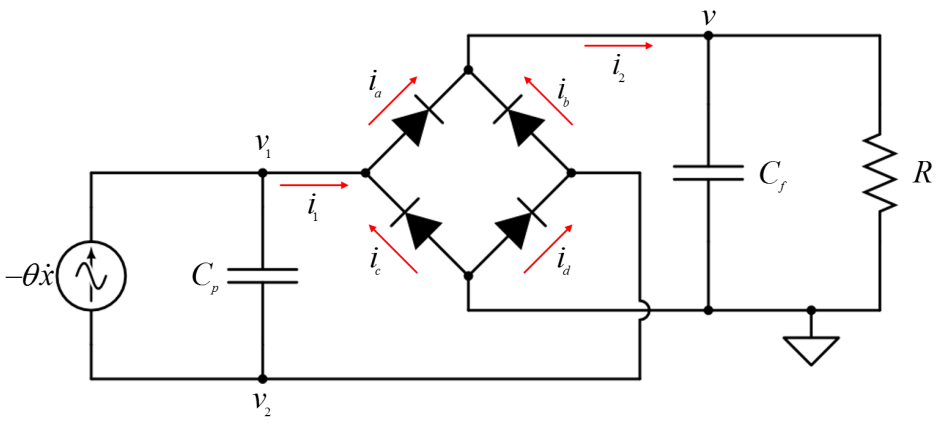

Figure 45: Circuit diagram of piezoelectric energy harvester connected to a bridge rectifier, filter capacitor, and load resistance. Currents and node voltages used for model derivations are labeled.

must be rectified and conditioned. The simplest passive way of accomplishing this is with a diode bridge and filter capacitor. A diagram of a piezoelectric energy harvester connected to such a circuit is shown in Figure 45.

On the left side of the bridge is the piezoelectric energy harvester modeled by a current source coupled to the structure motion and the capacitance of the piezoelectric material. On the right hand side of the diode bridge are the filter capacitor and a load resistance. Since for practical purposes the DC power is the quantity of interest, and the filter capacitor is properly large, any reactance of the load can be neglected. Node voltages and currents needed to derive the governing equations are labeled. By applying Kirchhoff's current law, the following expressions relating currents can be found.

$$i_1 = -\theta\dot{x} - C_p(\dot{v}_1 - \dot{v}_2) = i_a - i_c = i_d - i_b \tag{166}$$

$$i_2 = C_f\dot{v} + \frac{1}{R}v = i_a + i_b = i_c + i_d \tag{167}$$

To find the governing equations in terms of node voltages, a relationship between the voltage across a diode and the current flowing through it is required. For its combination of simplicity and smoothness, the Shockley diode model is used.

$$i_D = I_s\left[\exp\left(\frac{v_D}{nV_T}\right) - 1\right] \tag{168}$$

The Shockley diode model relates the voltage across the diode, v_D, to the current flow, i_D.

It is parameterized by the saturation current, I_s, and the product of the ideality factor and the thermal voltage, nV_T. The saturation current is the current that will flow backward through the diode when a large reverse voltage is applied and is on the order of 10^{-12} amps. A real diode has a reverse breakdown voltage at which large amounts of reverse current will flow. By using the Shockley model it is assumed that the diode bridge is properly chosen to avoid breakdown. The thermal voltage defined as $V_T = k_B T/q$, where k_B is Boltzmann's constant, T is the operating temperature, and q is the electron charge and is approximately 26 millivolts at room temperature. Using the Shockley model, the four diode currents can be expressed as:

$$\begin{aligned} i_a &= I_s \left[\exp\left(\frac{v_1 - v}{nV_T} \right) - 1 \right] \\ i_b &= I_s \left[\exp\left(\frac{v_2 - v}{nV_T} \right) - 1 \right] \\ i_c &= I_s \left[\exp\left(\frac{-v_1}{nV_T} \right) - 1 \right] \\ i_d &= I_s \left[\exp\left(\frac{-v_2}{nV_T} \right) - 1 \right] \end{aligned} \tag{169}$$

Since the Schockley model is an algebraic model for the current-voltage characteristic of a diode, it can be shown that the mean potential on the input terminals of the diode bridge must always equal the mean potential on the output terminals. This yields the relations:

$$\begin{aligned} v_p &= v_1 - v_2 \\ v &= v_1 + v_2 \\ v_1 &= \frac{v + v_p}{2} \\ v_2 &= \frac{v - v_p}{2}, \end{aligned} \tag{170}$$

which reduces the number of voltage that define the system from three to two, being the voltage across the electrodes of the piezoelectric cantilever, v_p as before, and the voltage across the load resistance, the negative terminal of which is grounded. Substituting the expressions for the diode currents and node voltages, v_1 and v_2, allows simplification of the current balance equations. The current balance equation involving the current flowing into

the diode bridge is given by:

$$C_p\dot{v}_p + \theta\dot{x} + 2I_s \sinh\left(\frac{v_p}{2nV_T}\right)\exp\left(\frac{-v}{2nV_T}\right) = 0 \tag{171}$$

Likewise the current balance equation involving current flowing out of the bridge is given by:

$$C_f\dot{v} + \frac{1}{R}v + 2I_s\left[1 - \cosh\left(\frac{v_p}{2nV_T}\right)\exp\left(\frac{-v}{2nV_T}\right)\right] = 0 \tag{172}$$

Combining these current balance equations with the differential equation governing the mechanical behavior above yields the a model describing the dynamics of a piezoelectric cantilever undergoing harmonic base acceleration excitation with electrodes connected to the input terminals of a diode bridge, the output terminals of which are connected to a filter capacitor and load resistor in parallel. As before, dielectric losses in the piezoelectric material are included.

$$m\ddot{x} + b_1\dot{x} + b_2\dot{x}^2\,\mathrm{sgn}(\dot{x}) + k_1x + k_2x^2\,\mathrm{sgn}(x) - \theta v_p = -\bar{m}A\cos(\Omega t) \tag{173}$$

$$C_p\dot{v}_p + \Omega C_p \tan\delta_e v_p + \theta\dot{x} + 2I_s \sinh\left(\frac{v_p}{2nV_T}\right)\exp\left(\frac{-v}{2nV_T}\right) = 0 \tag{174}$$

$$C_f\dot{v} + \frac{1}{R}v + 2I_s\left[1 - \cosh\left(\frac{v_p}{2nV_T}\right)\exp\left(\frac{-v}{2nV_T}\right)\right] = 0 \tag{175}$$

From these equations one can make qualitative descriptions of the system behavior. First, the equations are heavily biased in favor of positive values of the output voltage, v, due to the presence of the exponential functions. Secondly, the equation governing the evolution of the piezoelectric electrode voltage, v_p, is an odd function of v_p due to the hyperbolic sine function, while the equation governing the evolution of the output voltage, v, is an even function of v_p due to the hyperbolic cosine function. Both of these observations are consistent with an intuitive understanding of current rectification. As before, it is advantageous to nondimensionalize and cast the system in state space form. The same nondimensionalization and state representation as in Section 6.3.2 is used, with the addition of a fourth state representing the output voltage.

$$\begin{aligned} v &= V_c u_4 \\ \dot{v} &= \frac{V_c}{T_c}u_4' \end{aligned} \tag{176}$$

Substituting the nondimensional state definitions into the system yield the same result for the mechanical governing equation, but new expressions for the electrical governing equations:

$$C_p\frac{V_c}{T_c}u_3' + \Omega C_p \tan\delta_e V_c u_3 + \theta\frac{L_c}{T_c}u_2 + 2I_s \sinh\left(\frac{V_c u_3}{2nV_T}\right)\exp\left(\frac{-V_c u_4}{2nV_T}\right) = 0 \tag{177}$$

$$C_f\frac{V_c}{T_c}u_4' + \frac{1}{R}V_c u_4 + 2I_s\left[1-\cosh\left(\frac{V_c u_3}{2nV_T}\right)\exp\left(\frac{-V_c u_4}{2nV_T}\right)\right] = 0, \tag{178}$$

which can be arranged into state space form:

$$\begin{aligned}
f_1 = u_1' &= \ u_2 \\
f_2 = u_2' &= -\left(\frac{k_1 T_c^2}{m}\right)u_1 - \left(\frac{k_2 L_c T_c^2}{m}\right)u_1^2\,\mathrm{sgn}(u_1) - \left(\frac{b_1 T_c}{m}\right)u_2 \\
&\quad - \left(\frac{b_2 L_c}{m}\right)u_2^2\,\mathrm{sgn}(u_2) + \left(\frac{\theta V_c T_c^2}{mL_c}\right)u_3 - \left(\frac{\bar{m}AT_c^2}{mL_c}\right)\cos(\Omega T_c \tau) \\
f_3 = u_3' &= -\left(\frac{\theta L_c}{C_p V_c}\right)u_2 - (\Omega T_c \tan\delta_e)\,u_3 \\
&\quad - \left(\frac{2I_s T_c}{C_p V_c}\right)\sinh\left[\left(\frac{V_c}{2nV_T}\right)u_3\right]\exp\left[-\left(\frac{V_c}{2nV_T}\right)u_4\right] \\
f_4 = u_4' &= -\left(\frac{2I_s T_c}{C_f V_c}\right)\left\{1-\cosh\left[\left(\frac{V_c}{2nV_T}\right)u_3\right]\exp\left[-\left(\frac{V_c}{2nV_T}\right)u_4\right]\right\} - \left(\frac{T_c}{RC_f}\right)u_4
\end{aligned} \tag{179}$$

The Jacobian matrix is defined as previously.

6.5 Experimental Investigation

To verify the validity of the proposed model for the full nonlinear dynamics of a practically realized piezoelectric vibration harvester, a set of three types of experiments are conducted. First, the energy harvester is connected directly to a set of load resistances, ranging from near short circuit to near open circuit, and excited at low enough base acceleration levels to remain in the linear behavior regime (linear experiments). By comparing the predictions of the linear model to experimental frequency response functions, linear model parameters can be identified. Second, the energy harvester is excited by frequency sweeps at various constant base acceleration amplitudes while still connected to the same set of load resistors (AC–AC experiments). By comparing the predictions of the nonlinear mechanical model to experimental frequency response curves, the parameters governing the nonlinear mechanical dissipation and stiffness can be identified. Third, the energy harvester is connected

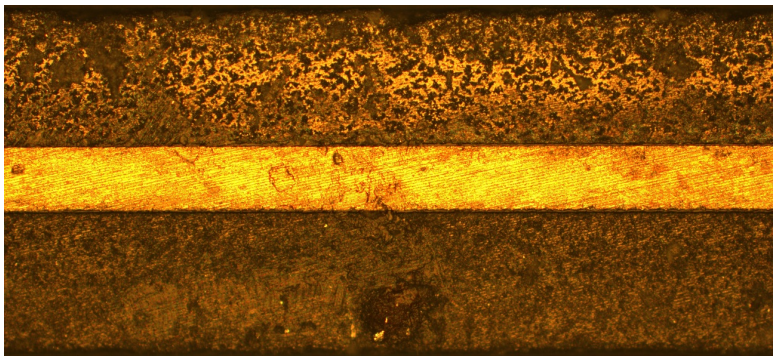

Figure 46: Magnified view of edge of cantilever. The brass substrate is the light colored central layer. The upper and lower layers are PZT-5A piezoceramic material.

to a bridge rectifier, filter capacitor, and load resistance to approximate practical energy harvesting operation (AC–DC experiments). Excitation for the AC–DC experiments is the same as for the AC–AC experiments. Load resistance values are the same for all three experiment types.

6.5.1 Experimental Setup

The piezoelectric energy harvester tested consists of a PZT-5A piezoelectric bimorph cantilever manufactured Piezo Systems, Inc. mounted in a custom fixture with conductive jaws electrically insulated from the rest of the clamp forming the two electrodes. The two piezoelectric layers are poled in opposite directions and are electrically connected in series. A microscope photograph showing the central brass substrate and upper and lower piezoelectric laminates is shown in Figure 46.

For base excitation experiments, the fixture is attached to the armature of a Brüel and Kjær Type 4810 mini shaker powered by an Hewlett Packard model 6826A power supply and amplifier. Frequency sweeps at constant base acceleration amplitude are conducted using an APS Dynamics, Inc. model VCS201 vibration control system using acceleration feedback. The base acceleration signal is measured using a Kistler A.G. Type 8636C5 piezoelectric accelerometer powered and conditioned by a Type 5134 power supply and coupler. Load resistance and filter capacitor values are varied using IET Labs, Inc. models RS-201W and CS-301L resistance and capacitance substitution boxes, respectively. Rectification is done using a Diodes Incorporated model KBP202G bridge rectifier. Tip velocity measurements

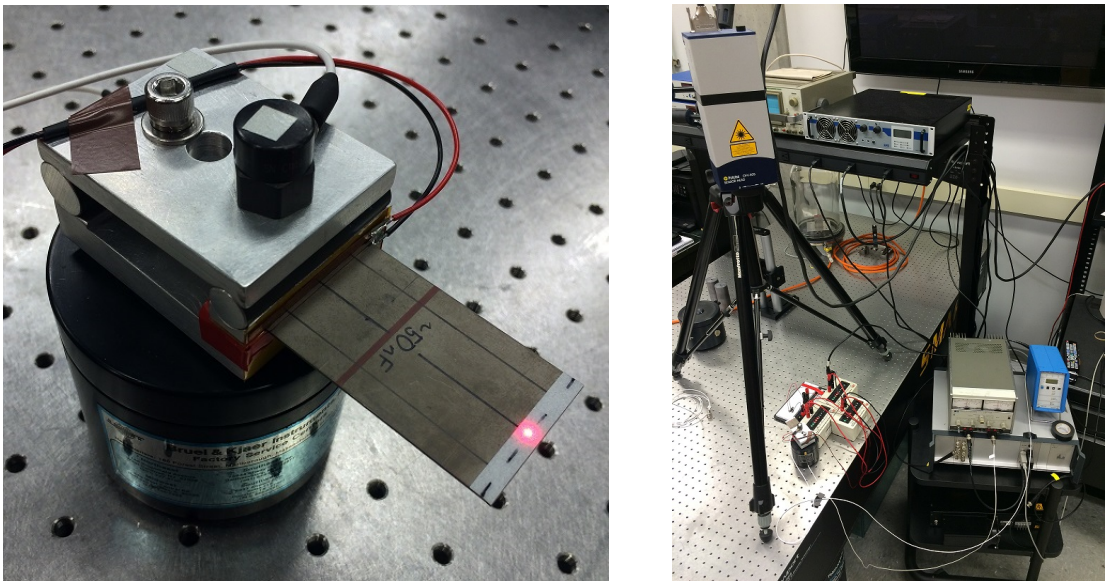

(a) (b)

Figure 47: Close up (a) and overview (b) photographs of the experimental setup. The piezoelectric bimorph cantilever is fixed in a custom clamp mounted to the shaker with an attached accelerometer. The upper and lower clamp jaws contact the nickel plating on the top and bottom surface of the cantilever forming the electrodes. Retroreflective tape is placed near the tip of the cantilever to facilitate laser vibrometer measurements. In the overview photograph, the laser vibrometer, vibration controller, power amplifier, accelerometer signal conditioner, resistance and capacitance substitution boxes, and breadboard for the rectification circuit are shown.

are made using a Polytec, Inc. model OFV-505 laser Doppler vibrometer and model OFV-5000 controller. Data is collected using National Instruments models 9215 and 9223 data acquisition units and SignalExpress software. For linear regime tests, the excitation signal sent to the amplifier is generated by an NI model 9263 analog output module. Photographs of the experimental setup are shown in Figure 47.

6.5.2 Linear Regime Experiments

Linear regime experiments generate measured frequency response functions relating the input base acceleration to the outputs of cantilever tip velocity measured in the inertial frame and the voltage across the load resistance. The set of load resistances consists of 13 resistance values ranging logarithmically from 1kΩ to 1MΩ. From the meausured voltage frequency response function, current and power frequency response functions can be calculated. The excitation for the linear regime experiments consists of a rectangular white noise

signal. Multiple averages are taken. The base acceleration level is kept low to ensure system behavior is linear, with an RMS value of the base acceleration noise signal of approximately $0.01g$.

Figure 48 shows a comparison between the measured experimental tip velocity and electrode voltage, calculated experimental current and power frequency response functions, and predictions from the linear models given above. Experimental data is shown by markers and model predictions by curves. Each color corresponds to a different resistance value, with black markers in the experimental velocity frequency response plot indicating true short circuit, with a peak near 115 Hz, and true open circuit conditions, with a peak near 120 Hz. First principles geometric and model parameters are either measured directly or taken from manufacturer estimates and updated to match observed behavior. Geometric and material properties of the bimorph needed for the linear models can be found in Table 13.

Model predictions match well with experimental data. It is notable that this energy harvester shows two separate maxima in the power generation frequency response function: one at a small load resistance value (near short circuit conditions with a lower frequency of the peak) and one at a large load resistance value (near open circuit with a higher frequency of the peak). This is characteristic of electromechanical resonant systems that have a large relative degree of electromechanical coupling. In the linear regime, the two power generation maxima are distinct, but will tend to coalesce for larger excitation levels as will be discussed further in Section 6.5.4. For a ideal piezoelectric material with no dielectric loss, the two peaks in power generation would be of the same magnitude. For this energy harvester, dielectric loss is significant, and so the peak power point near open circuit conditions, which experiences higher voltages, is lower in magnitude than the near short circuit peak power point.

6.5.3 Mechanically Nonlinear Regime Experiments

Mechanically nonlinear energy harvesting experiments consist of frequency sweep tests at constant acceleration levels of 0.1, 0.2, and $0.3g$ RMS. Tests at each acceleration level were

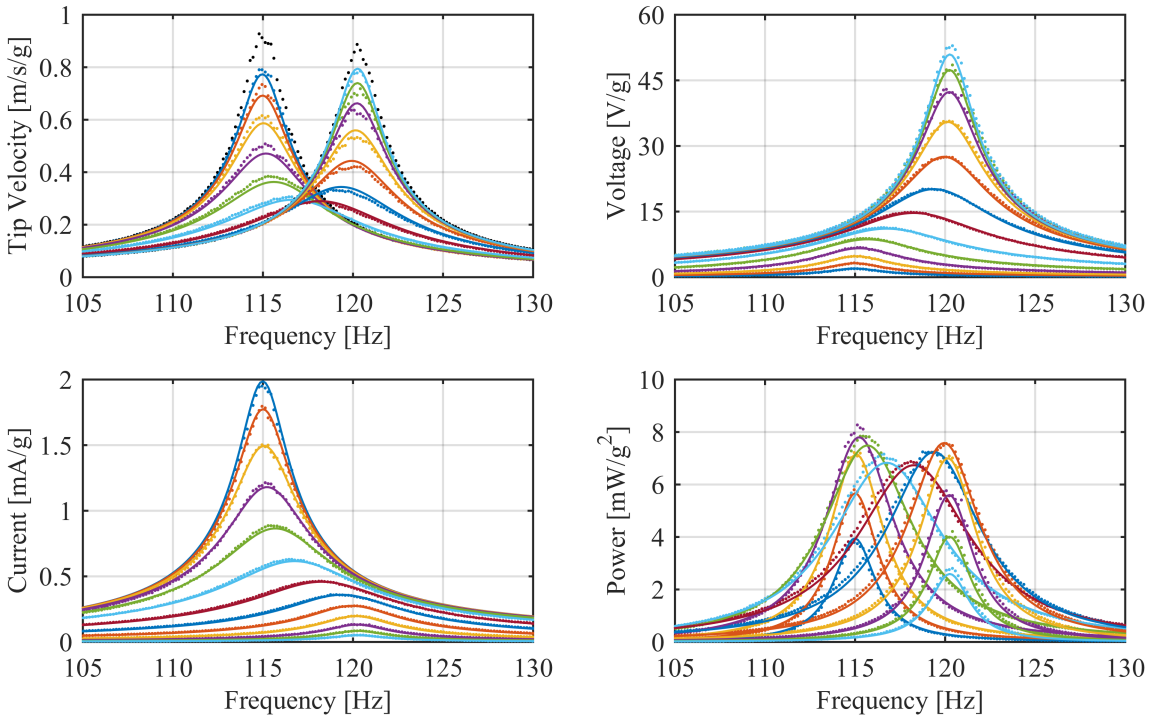

Figure 48: AC input–AC output test data and model in the linear response regime with various load resistance values. Experimental data shown with markers and model predictions shown with curves.

Table 13: Material and geometric parameters for the brass-reinforced PZT-5A bimorph cantilever (Piezo Systems, Inc. model number T226-A4-503X).

(a) Material parameters

PZT density	ρ_p	7800	kg
PZT elastic modulus	c_{11}	66	GPa
PZT loss factor	γ_1	0.021	
Coupling	e_{31}	-14.4	C/m^2
Permitivity	ϵ_{33}	14.2	nF/m
Brass density	ρ_s	8500	kg
Brass elastic modulus	c_s	100	GPa

(b) Geometric parameters

Overhang length	l	51.9	mm
Total length	l_e	63.7	mm
Width	b	31.8	mm
PZT thickness (each)	h_p	0.267	mm
Brass thickness	h_s	0.127	mm

Table 14: Identified second order mechanical stiffness and dissipation parameters.

Second order modulus	c_{111}	-83	TPa
Second order loss factor	γ_2	0.15	

repeated for the same 13 load resistance values, ranging from 1kΩ to 1MΩ, used in the linear regime experiments. The maximum base acceleration amplitude of $0.3g$ RMS is chosen to keep the cantilever tip deflection within the safe limits provided by the manufacturer. This choice of base acceleration level corresponds to a safety factor of approximately two for the maximum tip displacement. The frequency sweep rate for each test must be slow enough for the test to occur at quasi-steady state. Each data point in the experimental frequency response curves is the result of an average of approximately 100 cycles. Mechanically nonlinear regime experiments are first conducted for the AC–AC circuit configuration, which is the same as in the linear regime experiments, and then followed by the AC–DC circuit configuration with rectification. To allow direct comparisons of behavior with and without the electrical nonlinearities caused by rectification, the nonlinear mechanical and fully nonlinear tests cases are conducted with the same set of base acceleration amplitudes.

6.5.3.1 AC–AC circuit configuration

Plots of experimental data and model predictions are shown in Figures 49–51. RMS tip velocity, RMS voltage, RMS current, and average power are shown. Colors again correspond to the load resistance value and match those of the linear regime tests. Model predictions are generated using the model given above solved using a general numerical harmonic balance solver (Appendix B). By comparing the predictions of the nonlinear mechanical model to experimental frequency response curves, the parameters governing the nonlinear mechanical dissipation and stiffness can be identified. The parameters defining the nonlinear mechanical behavior are shown in Table 14.

Again there is good agreement between model predictions and experimental results. As the model is a relatively simple model including only nonlinearities in the mechanical dissipation and stiffness, it is most accurate for lower excitation amplitudes and loses some accuracy as the excitation amplitude increases. In these plots, the limits of the vertical axis

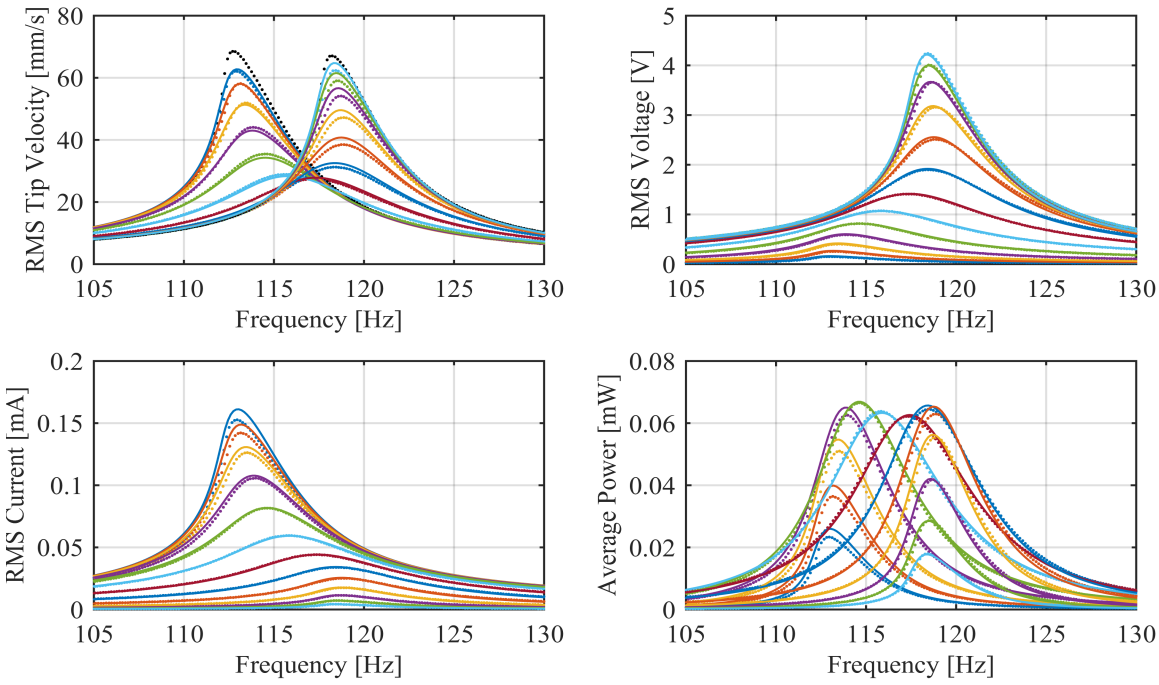

Figure 49: AC–AC test data and model at $0.1g$ RMS with various load resistance values. Experimental data shown with markers and model predictions shown with curves.

scale with the excitation amplitude. The effect of the nonlinear mechanical dissipation can be seen in the decrease in the response amplitude relative to the excitation amplitude with growing base acceleration level. The effect of the nonlinear stiffness can be seen in the shifts of the short circuit and open circuit resonant peaks. Short circuit and open circuit resonant peaks shift from approximately 115 and 120 Hz in the linear regime to 110 and 115 Hz at $0.3g$ RMS.

6.5.3.2 AC–DC circuit configuration

For the AC–DC experiments, the steady state output voltage depends on both the filter capacitance and the load resistance. As in the linear and AC–AC experiments, the mean power generation level and resonant frequency depends on the load resistance. Additionally, the amount of unwanted ripple in the load voltage and current depends on the time constant of the output, namely the product RC_f. The ripple factor is defined as:

$$RF = \frac{\sqrt{V_{RMS}^2 - V_{DC}^2}}{|V_{DC}|}.$$

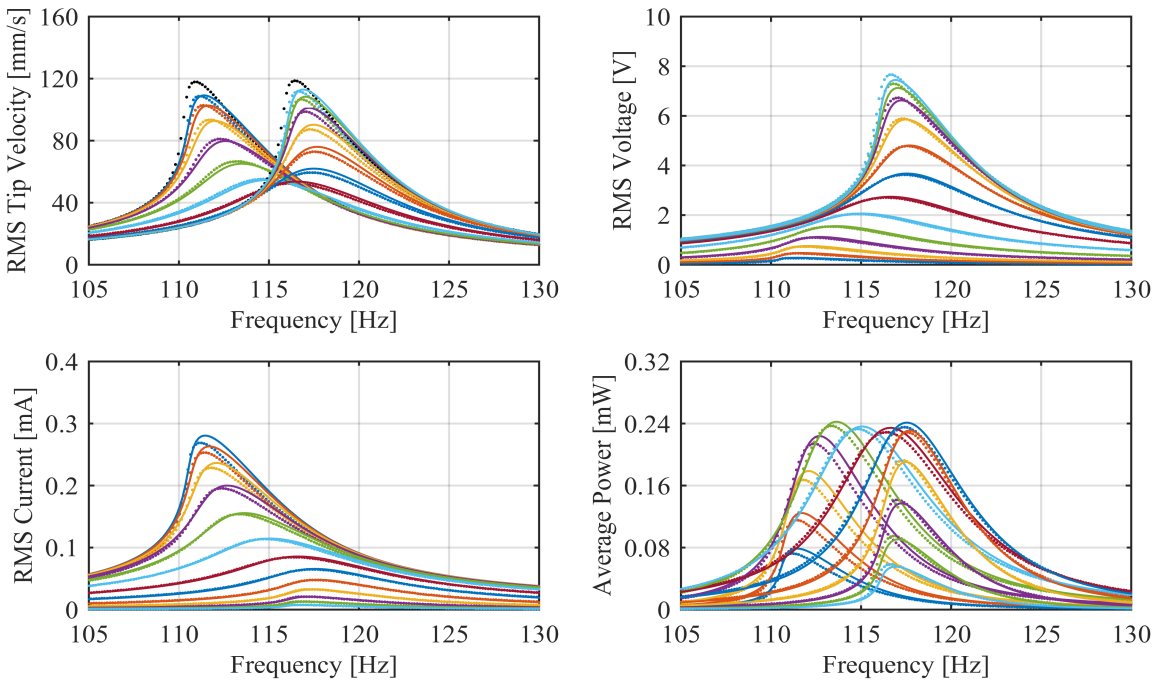

Figure 50: AC–AC test data and model at $0.2g$ RMS with various load resistance values. Experimental data shown with markers and model predictions shown with curves.

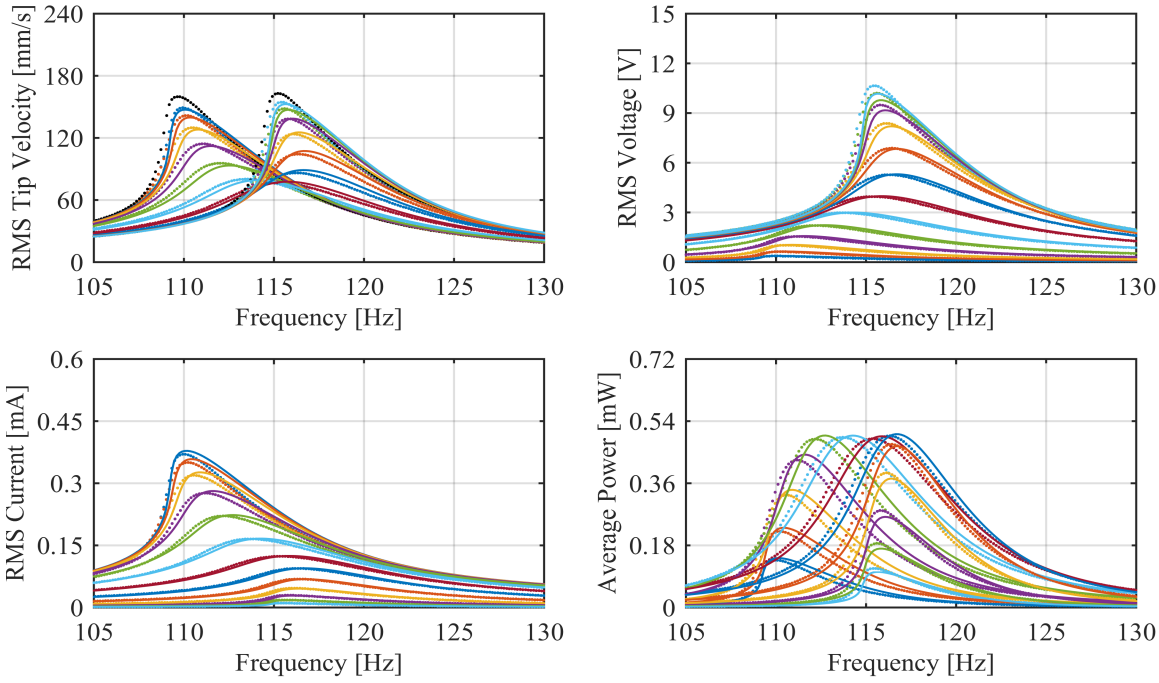

Figure 51: AC–AC test data and model at $0.3g$ RMS with various load resistance values. Experimental data shown with markers and model predictions shown with curves.

Table 15: Identified parameters for diodes in the bridge rectifier.

Saturation current	I_s	1	pA
Ideality factor	n	1	
Thermal voltage	V_T	26	mV

The larger the value of the time constant, RC_f, the smaller the amount of ripple. This is desirable, and so a practical energy harvester would have a value for RC_f significantly larger than the ripple period. Experimentally, frequency sweep tests are conducted at quasi-steady state, and so the frequency sweep rate of the must change inversely proportional to the output time constant. Therefore, to ensure that the single sweep rate also used in the AC–AC experiments will be slow enough for all tests without making them unnecessarily lengthy, filter capacitor values are chosen for each of the load resistance values to make the output time constant always 0.01 seconds, or approximately two times the period of the ripple current. This means that for load resistance values ranging from 1kΩ to 1MΩ, filter capacitor values vary from 10μF to 10nF.

Plots of experimental data and model predictions are shown in Figures 52–54. RMS tip velocity, DC output voltage, DC current, and average power are shown. Colors again correspond to the load resistance value and match those of the linear regime tests and AC–AC experiments. Model predictions are generated using the fully nonlinear model given above solved using a general numerical harmonic balance solver (Appendix B). By comparing the predictions of the fully nonlinear model to experimental frequency response curves, the parameters governing the rectification circuit can be identified. The parameters defining the rectification nonlinearity are shown in Table 15. The values used are typical values for silicon diodes and did not require any updating.

The fully nonlinear model agrees well with experimental results to predict trends and behavior of a practically realized piezoelectric vibration energy harvester. The most important qualitative differences between the AC–AC and AC–DC behavior of the energy harvester can be seen in the tip velocity and power generation frequency response curves. In the velocity response, the magnitude of the near short circuit resonance is greatly reduced compared to the near open circuit response. In the AC–AC experiments, the amplitudes of

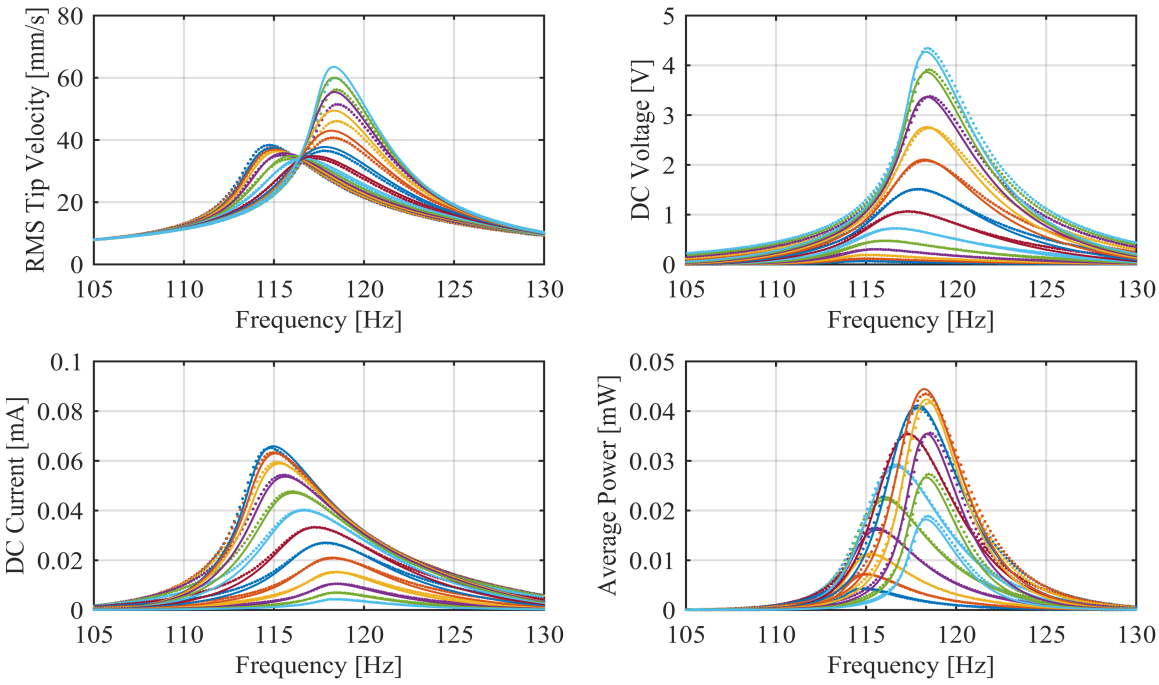

Figure 52: AC–DC test data and model at $0.1g$ RMS with various load resistance values. Experimental data shown with markers and model predictions shown with curves.

the velocity response are very similar between near short and near open circuit condtions. In the power generation response, the curves on the left side of the plot corresponding to near short circuit conditions are reduced in height compared to the curves on the right side corresponding to near open circuit conditions. As the base acceleration level increases, the discrepancy between the short and open circuit responses decreases. At $0.1g$ RMS, the near short circuit velocity response amplitude is approximately 64% that of the near open circuit response. This grows to 79% and 85% at 0.2 and $0.3g$ RMS, respectively. This effect is due to the non-ideal nature of the diode bridge rectifier. As the magnitude of the voltage across the diode bridge rises, the diodes act more like ideal switches. Therefore, the efficiency of the rectifier grows both with the base acceleration amplitude, which increases all response signals, as well as the load resistance, which increase steady state voltage levels. Interestingly, while the near short circuit peak power generation will be higher than the near open circuit power generation for a linear piezoelectric cantilever energy harvester due to dielectric losses, the near open circuit conditions will produce more power for a practical energy harvester with rectification at finite base acceleration levels.

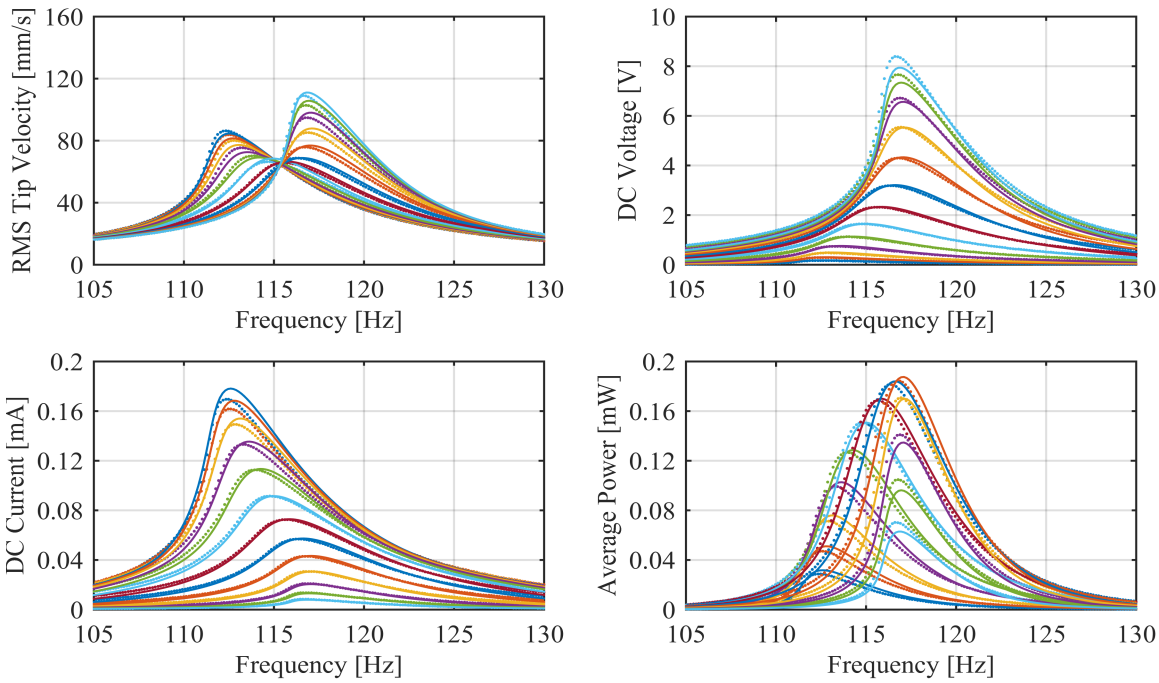

Figure 53: AC–DC output test data and model at $0.2g$ RMS with various load resistance values. Experimental data shown with markers and model predictions shown with curves.

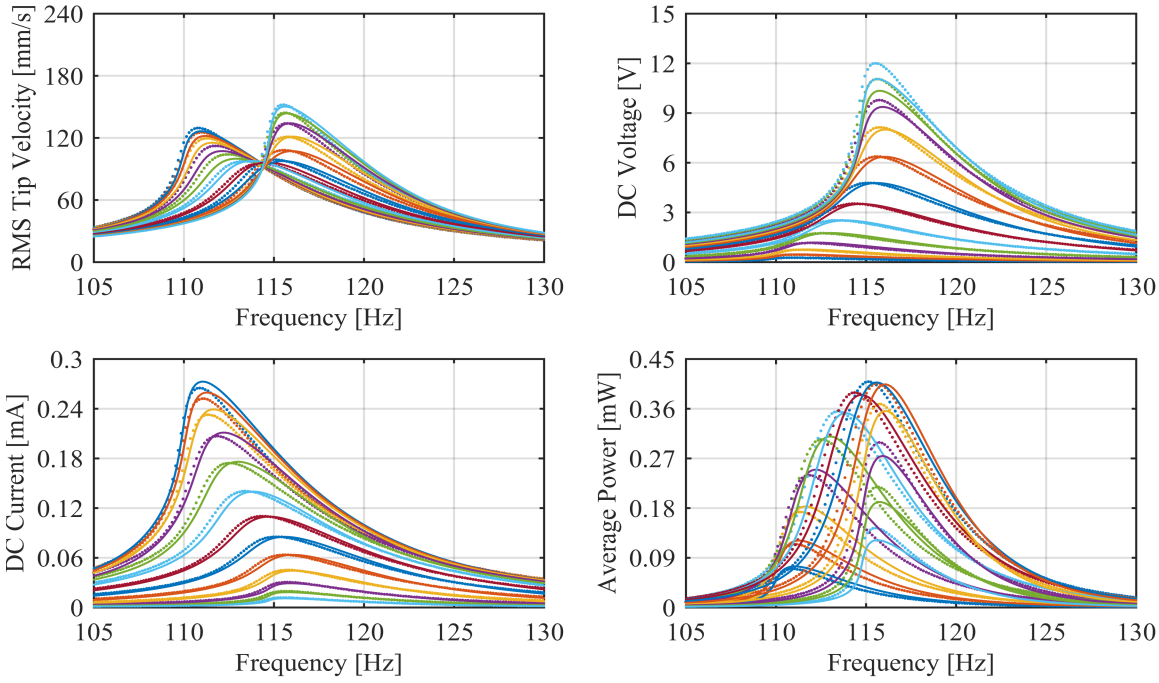

Figure 54: AC–DC output test data and model at $0.3g$ RMS with various load resistance values. Experimental data shown with markers and model predictions shown with curves.

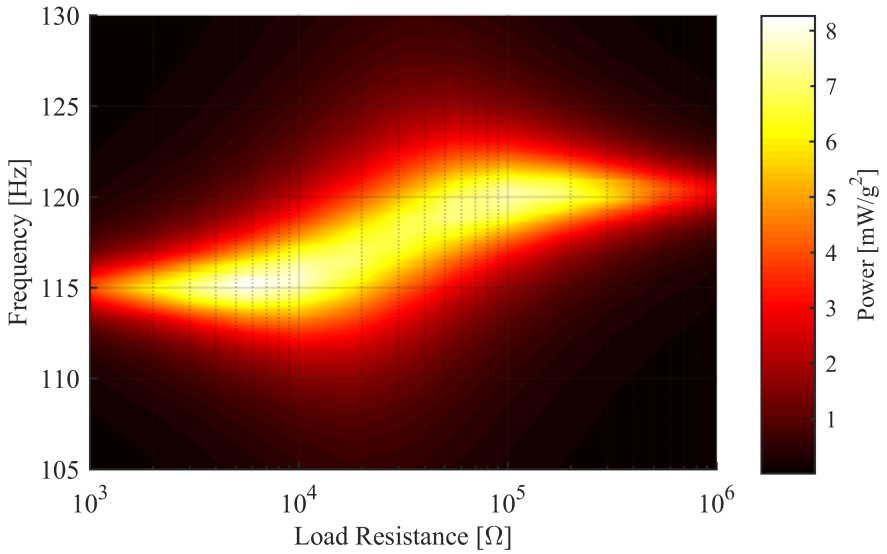

Figure 55: Heat map of experimental energy harvesting performance in the mechanically linear regime. Color corresponds to the time-averaged power output of the harvester normalized with respect to the base acceleration level squared.

6.5.4 Qualitative Performance Comparisons and Trends

To understand the effects of the mechanical (dissipation and stiffness) and electrical (rectification) nonlinearities and their interaction with each other, it is useful to compare energy harvesting performance. As a baseline for comparison, the linear regime AC–AC power generation performance can be used. Shown in Figure 55 is heat map plot of the experimental linear regime power generation performance of the energy harvester normalized by the square of the base acceleration level.

The horizontal and vertical axes correspond to the load resistance value and frequency of base excitation, respectively. Clearly visible are the two maxima of power generation near the short circuit and open circuit loading conditions. The presence of two well-separated peak power points is characteristic of systems with strong electromechanical coupling. In the linear regime, the energy harvester produces a maximum normalized time-averaged power of approximately 8.3 mW/g^2, and the color of the heat map corresponds to the power output relative to that level. For fair comparisons, the shading in the heat maps for AC–AC and AC–DC performance in the mechanically nonlinear regime are also normalized in this way.

Figure 56 shows an array of six heat maps for the time-averaged power generation. From top to bottom, the rows correspond to the three base acceleration levels of 0.1, 0.2, and $0.3g$ RMS, respectively. The two columns correspond to the two circuit configurations, with the AC–AC configuration on the left, and the AC–DC configuration on the right. All six heat maps are shaded relative to the 8.3 mW/g^2 maximum normalized mean power generation level of the linear regime performance shown in Figure 55.

The first apparent trend is that normalized power generation performance is lower in all six mechanically nonlinear regime tests than that of the linear regime, as shown by the darker shades. As was shown with earlier modeling, the dominant mechanical nonlinearities are in the dissipation and stiffness. Power generation performance decreases with increasing mechanical damping, and so the nonlinear mechanical dissipation reduces the normalized power generation performance as response amplitudes increase at higher excitation levels. The stiffness nonlinearity only effects the magnitude of power generation slightly. Its primary effect is to shift the location of peak power operating points, shifting them to lower frequencies and higher load resistance values.

Secondly, the power generation performance of the AC–DC configuration is noticeably lower than that of the AC–AC configuration. The AC–DC configuration retains the power generation losses due to the nonlinear mechanical dissipation and adds electrical dissipation in the bridge rectifier. An ideal bridge rectifier, as examined by Shu[85] and others, dissipates no power. It acts as a perfect conductor for positive bias voltages (no voltage drop), and a perfect insulator for negative bias voltages (no current flow). A real diode bridge does dissipate power, and so reduces the power supplied to the load. Therefore, the linear regime AC–AC power generation performance can be seen as a global upper limit and the mechanically nonlinear AC–AC performance as excitation level specfific upper bounds.

The first and second observed trends show that the nonlinear mechanical dissipation reduces relative power generation performance as excitation level increases, and the AC–DC circuit configuration will always have lower absolute performance than the AC–AC configuration due to electrical power dissipation in the diode bridge. However, unlike the AC–AC case, as the base excitation level increases, the normalized power generation performance of

the AC–DC configuration improves rather than declines. While losses in the diode bridge are unavoidable, and it never acts like the idealized one-way perfect conductor, the exponential nature of a diode's I–V characteristic means that as the amplitude of the voltage across the piezoelectric electrodes increases, the diode bridge acts more and more ideally. The contribution to the total loss of the diode bridge relative to mechanical dissipation therefore decreases with increasing excitation level. For certain choices of piezoelectric energy harvester and circuit components (e.g. the system studied here), the normalized power generation will increase with increasing excitation level as rectification becomes more ideal and then will decrease as nonlinear mechanical dissipation becomes dominant.

Finally, a fourth trend can be seen by examining the linear and mechanically nonlinear power generation performance of the AC–AC circuit configuration. As mentioned earlier, this energy harvester shows two distinct peak power points in the linear response regime, characteristic of a strongly electromechanically coupled system. At the lowest base acceleration level ($0.1g$ RMS) of the mechanically nonlinear tests, the two peak power points are still visible. However, as the base acceleration level grows to $0.3g$ RMS, the two peaks appear to merge and become a single global maximum. This effect is again due to the nonlinear mechanical dissipation. The two high amplitude responses near short circuit and open circuit conditions are preferentially attenuated compared to the lower amplitude response at between them. The dip in power generation performance between the near short circuit and near open circuit conditions therefore disappears as the excitation level increases due to the nonlinear mechanical dissipation.

6.5.5 Response Waveforms

One of the benefits of using the method of harmonic balance to solve the nonlinear lumped parameter models for a practical energy harvester, is that it allows the quick simulation of steady state behavior. From the performance curves and heat maps, the optimal power generation performance of the energy harvester in the practical AC–DC circuit configuration at $0.3g$ RMS occurs at approximately 115 Hz, with an optimal load resistance of around 56kΩ. Simulating these conditions with the method of harmonic balance takes much less

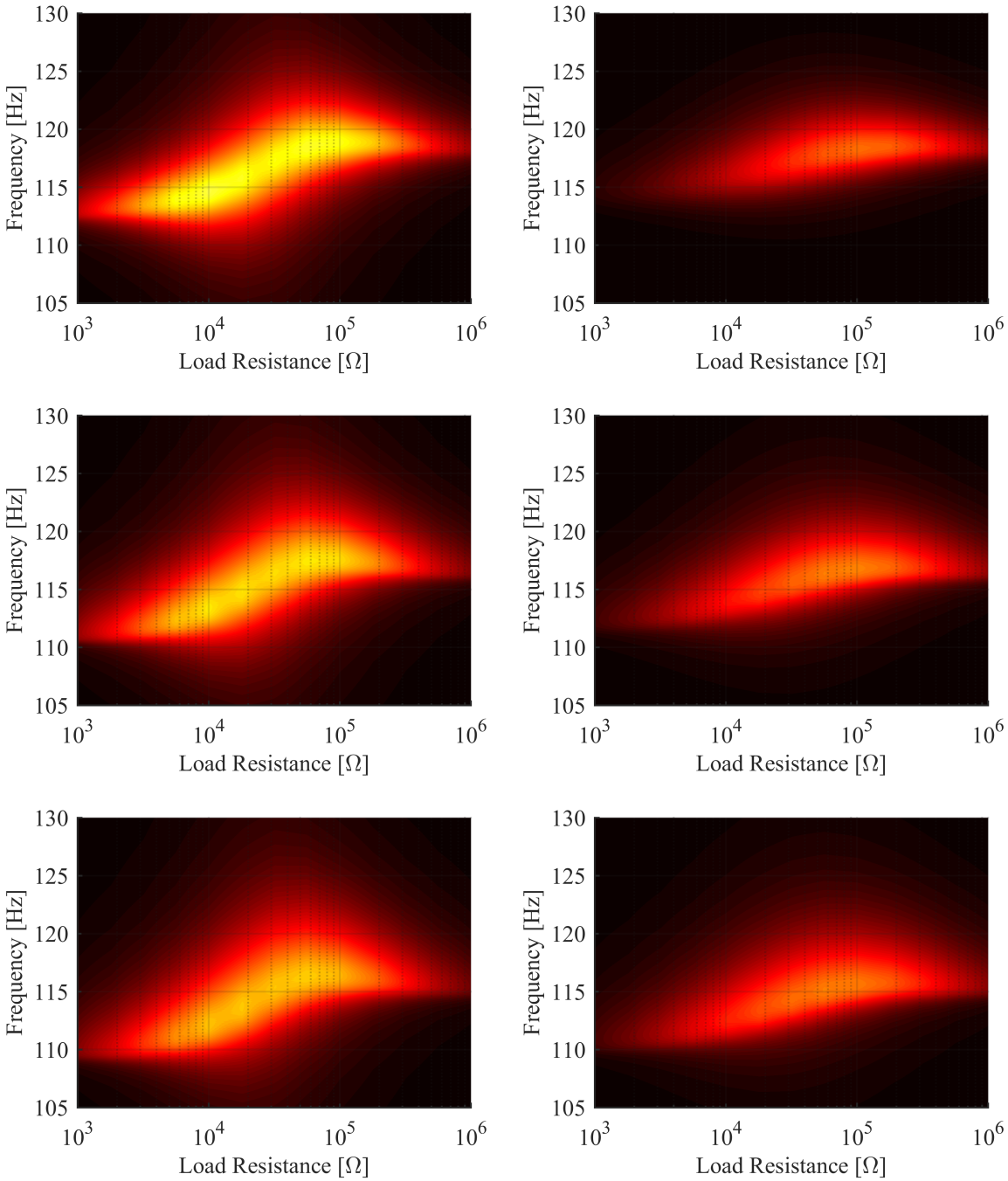

Figure 56: Heat maps of experimental energy harvesting performance in the mechanically nonlinear regime. From top to bottom, rows correspond to the three tested excitation levels of 0.1, 0.2, and 0.3g RMS, respectively. The left column corresponds to the AC–AC case, and the right column corresponds to the AC–DC case. Color corresponds to the time-averaged power output of the harvester normalized with respect to the base acceleration level squared. Color is scaled relative to that of the linear regime performance shown in Figure 55.

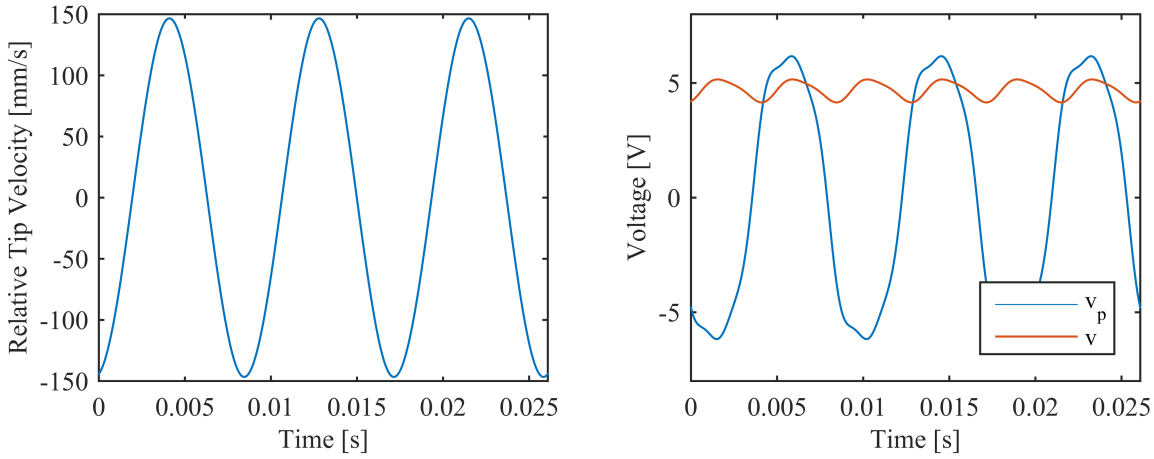

Figure 57: Representative simulated response waveforms at $0.3g$ RMS at near optimal load resistance of 56kΩ and peak power frequency of 115 Hz. Relative tip velocity is shown on the left, and the output voltage, v, and piezoelectric electrode voltage, v_p, are shown on the right in red and blue, respectively.

computation time than a time domain numerical simulation. Figure 57 shows the model predicted waveforms of the relative tip velocity, piezoelectric electrode voltage, and load voltage. These waveforms are produced from the harmonic balance solution including frequency components up to five times the excitation frequency. Notably, the velocity response appears quite sinusoidal, while the piezoelectric electrode voltage, v_p, clearly shows higher harmonic content. The load voltage, v, shows a noticeable amount of ripple. As discussed previously, a filter capacitance somewhat smaller than what would be used in practical energy harvesting circuit was used in this work for experimental reasons. However this example shows highlights the ability of a the method described here to find highly solutions without making assumptions like a constant output voltage.

6.6 Conclusions

In the existing literature of energy harvesting from dynamical systems, mechanical and electrical nonlinear effects have predominantly been explored in separate domains. Mechanically and electromechanically nonlinear frameworks have employed linear electrical circuitry to formulate AC input–AC output problems, while the existing efforts on nonlinear circuits have assumed linear mechanical behavior. However, even for the simplest case of a cantilever with piezoelectric laminates, nonlinearities in the mechanical domain are required

in modeling for accurate prediction of the structural response at relatively high excitation levels, and likewise a stable DC (direct current) signal must be obtained to charge a storage component in realistic energy harvesting applications. Therefore, a complete representation of vibration-based energy harvesting requires accounting for mechanical and dissipative nonlinearities as well as the nonlinear process of AC–DC conversion. In this chapter a multiphysics harmonic balance framework was presented that combines these mechanical and electrical nonlinear effects to predict the DC electrical output (DC voltage across the load) in terms of the AC mechanical input (base vibration). Focus was placed on a bimorph cantilever with piezoelectric laminates connected to a full-wave rectifier and a filter capacitor. The problem is explored first to characterize mechanical nonlinearities by exploring the AC input (base excitation) and AC output (voltage across the load) problem in the presence of a resistive load. Mechanical nonlinearities are identified for different excitation levels. A rectifier with filter capacitor is then introduced to the system. For the multiphysics equations of the fully coupled nonlinear system, a harmonic-balance solution was applied to analyze the mechanically and electrically nonlinear system dynamics at different excitation levels. A full set of experiments was conducted, showing trends and interactions of the mechancial dissipative and stiffness nonlinearities and the rectification nonlinearities. The experiments validated the proposed modeling method, and highlighted the need for simulating the full nonlinear dynamics of resonant piezoelectric energy harvesters.

Chapter VII

CONCLUSIONS, CONTRIBUTIONS, AND FUTURE WORK

7.1 Summary and Conclusions

7.1.1 Intentionally Designed Nonlinearities

Nonlinear frequency bandwidth enhancement in vibration energy harvesting can be achieved most effectively in the presence of strong nonlinearities and under high excitation levels. This constitutes a fundamental challenge in enabling nonlinear energy harvesters for low-intensity environments. Following study of the passive M-shaped oscillator, an M-shaped piezoelectric energy harvester configuration was developed, which can exhibit a nonlinear frequency response under very low vibration levels (below $0.1g$). This configuration was made from a continuous bent spring steel with piezoelectric laminates and a proof mass but no magnetic components. Properly locating the piezoelectric patches (to avoid substantial piezoelectric softening) in this design enables achieving the jump phenomenon in hardening at a few milli-g base acceleration levels.

Both primary and secondary (superharmonic) resonance excitations were explored at different vibration levels and load resistance values. The primary resonance excitation case that offers a 660% increase in the half-power bandwidth as compared to the linear system at a root-mean-square excitation level as low as $0.04g$. The secondary resonance behavior was investigated with a focus on 1:2 and 1:3 superharmonic resonances. Following the development of an empirical model, a multi-term harmonic balance framework was developed for a computationally effective yet high-fidelity analysis of this high-quality-factor system with cubic and quadratic nonlinearities. Experimental measurements and electromechanical model predictions resulted in very good match for both primary and secondary resonance cases explored in this work.

Overall, substantial nonlinear bandwidth is achieved for very low base acceleration levels under primary resonance excitation. The secondary resonance of interest in this work

was superharmonic resonance for nonlinear frequency-up conversion. It has been noted that the optimal electrical load of superharmonic response is close to that of the same harvester under primary resonance excitation. This is because the optimal load impedance depends on the dominant frequency content of the harvesters response, rather than the dominant frequency content of the excitation (no such distinction exists in linear harvesters or nonlinear ones under primary resonance excitation). Superharmonic resonance behavior may be exploited for energy harvesting purposes as it allows low frequency ambient vibrations to excite energy harvesting devices that might have higher natural frequencies due to size and mass constraints (e.g. MEMS energy harvesters), as a nonlinear frequency-up conversion mechanism.

In low-frequency superharmonic resonance experiments, an experimental imperfection of the electrodynamic shaker (which fails to produce pure harmonic signal for excitations roughly below 5 Hz) was pointed out and used as an opportunity to formulate and explore nonlinear response to multi-harmonic excitation in the secondary resonance regime. Multi-term harmonic balance solution resulted in very good match for the complex case of multi-harmonic excitation combined with secondary resonance behavior.

7.1.2 Inherent Electroelastic Material and Dissipative Nonlinearities

Nonlinearities of piezoelectric materials are manifested in various engineering applications such as sensing, actuation, as well as their combined applications for vibration damping and control, and most recently, energy harvesting from dynamical systems. Literature dealing with the dynamics of electroelastic structures made of piezoelectric materials has explored such nonlinearities in a disconnected way for the separate problems of mechanical and electrical excitation, such that nonlinear resonance trends have been assumed to be due to different additional terms in constitutive equations by different researchers. In this dissertation an experimentally validated, nonlinear, nonconservative model has been proposed to describe the energy harvesting, sensing, and dynamic actuation behavior of piezoelectric cantilevers for a wide (low-to-moderately nonlinear) range of mechanical and electrical excitation levels. A set of governing partial differential equations was derived using Hamilton's

principle. Those equations were spatially discretized for the fundamental bending mode, creating a lumped parameter model to be analyzed using the method of harmonic balance. The model showed excellent agreement to extensive experimental investigation of energy harvesting and dynamic actuation over the full range of structurally safe excitation levels of the brittle PZT-5A bimorph cantilever near resonance. The agreement of the model and experiment at all excitation levels is evidence that the dominant stiffness and electromechanical coupling nonlinearity apparent in certain piezoelectric structures is quadratic in nature. The backbone curves of both energy harvesting and actuation frequency responses are reported to be dominantly of first order for a broad range of mechanical and electrical excitation levels, in agreement with the experiments. While quadratic terms vanish during the analysis of a symmetric bimorph when examining polynomial electric enthalpy expansions in strain, an expansion form in strain amplitude retains those quadratic terms. Therefore, nonlinear effects associated with ferroelastic softening and dissipation should be given the priority in modeling of electroelastic nonlinearities in energy harvesting, sensing, and actuation for low-to-moderately nonlinear response forms with electric fields well below the coercive field.

Having studied a specific brass-reinforced PZT-5A bimorph, samples made from PZT-5A and PZT-5H layers of three different thicknesses each were subjected to base acceleration and dynamic voltage actuation testing ranging from the linear regime to close to the failure limits of the device, where nonlinear behavior is strong. A single second order correction to the elastic modulus parameterized by a quadratic elasticity coefficient has been shown to well-approximate the nonlinear electroelastic behavior of a class of geometrically stuff piezoelectrically coupled beams. Values of the quadratic elasticity coefficent, c_{111} of between -60 and -65 TPa for PZT-5A and between -40 and -55 TPa for PZT-5H can be used as guidelines for the accurate modeling of these materials. Additionally, the hypothesis that observed nonlinear dissipation is due to internal mechanisms rather than aerodynamic drag was verified by conducting in-vacuo experiments. The success of the proposed model to predict behavior and extract parameters of structures made with both poled and unpoled piezoceramic supports findings that the dominant nonlinear resonant behavior is due to elastic

and mechanically dissipative effects rather than due to nonlinearities in electromechanical coupling.

7.1.3 Electrical Circuit and Power Conditioning Nonlinearities

In the existing literature of energy harvesting from dynamical systems, mechanical and electrical nonlinear effects have predominantly been explored in separate domains. Mechanically and electromechanically nonlinear frameworks have employed linear electrical circuitry to formulate AC input–AC output problems, while the existing efforts on nonlinear circuits have assumed linear mechanical behavior. However, even for the simplest case of a cantilever with piezoelectric laminates, nonlinearities in the mechanical domain are required in modeling for accurate prediction of the structural response at relatively high excitation levels, and likewise a stable DC (direct current) signal must be obtained to charge a storage component in realistic energy harvesting applications. Therefore, a complete representation of vibration-based energy harvesting requires accounting for mechanical and dissipative nonlinearities as well as the nonlinear process of AC–DC conversion. In Chapter 6, a multiphysics harmonic balance framework that combines these mechanical and electrical nonlinear effects to predict the DC electrical output (DC voltage across the load) in terms of the AC mechanical input (base vibration) was presented. Focus was placed on a bimorph cantilever with piezoelectric laminates connected to a full-wave rectifier and a filter capacitor. The problem was explored first to characterize mechanical nonlinearities by exploring the AC input (base excitation) and AC output (voltage across the load) problem in the presence of a resistive load. Mechanical nonlinearities are identified for different excitation levels. A rectifier with filter capacitor was then introduced to the system. For the multiphysics equations of the fully coupled nonlinear system, a harmonic-balance solution was applied to analyze the mechanically and electrically nonlinear system dynamics at different excitation levels. A full set of experiments was conducted, showing trends and interactions of the mechanical dissipative and stiffness nonlinearities and the rectification nonlinearities. The experiments validated the proposed modeling method, and highlighted the need for simulating the full nonlinear dynamics of resonant piezoelectric energy harvesters.

7.2 Contributions

The following highlights from this dissertation summarize the major contributions:

- Development of a simple M-shaped bent beam structure (without complex magnetic components or magnetoelastic interactions) with fixed end conditions for nonlinear broadband vibration energy harvesting from very low and realistic base accelerations, and thereby demonstration of the jump phenomenon for base accelerations as low as a few milli-g (Chapter 2);

- Multi-term harmonic balance modeling of the M-shaped asymmetric oscillator and demonstration of the effect of higher harmonics on the (saddle-node) bifurcation point of the jump phenomenon in up-sweep of the frequency and on the power output (Chapter 2);

- Exploration of both primary and secondary resonances in the intentionally designed M-shaped piezoelectric energy harvester with quadratic and cubic nonlinearities with a detailed account of predominant (cubic vs. quadratic) nonlinear effects in the respective (primary vs. secondary) resonance neighborhoods (Chapter 3);

- Approximate analytical modeling of multi-harmonic excitation in the M-shaped nonlinear piezoelectric energy harvester and its experimental validation for the problem of 1:2 and 1:3 superharmonic resonance behavior (Chapter 3);

- A backbone curve-based, high-fidelity, dynamical systems approach and nonlinear non-conservative framework development for unified electroelastic modeling and identification of piezoelectric nonlinearities soft ceramic (e.g. PZT-5A and PZT-5H) bimorphs for a range of excitation levels in energy harvesting, sensing, and actuation well below the coercive field (Chapter 4);

- Rigorous validation of the aforementioned framework (Chapter 4) for a set of brass-reinforced stiff PZT-5A and PZT-5H bimorphs with different piezoelectric laminate thicknesses (Chapter 5);

- Unveiling the first-order nature of the backbone curve for stiff piezoelectric cantilevers (poled and unpoled PZT-5A and PZT-5H), concluding that two nonlinear parameters are sufficient (quadratic elastic softening and quadratic material dissipation) in modeling of piezoelectric softening in energy harvesting problem in the absence of other nonlinearities (e.g. geometric, inertial etc.) (Chapter 5)

- With this thoroughly validated quadratic dissipation and loss framework (Chapters 4-5), clarification of the order of manifestation of piezoelectric softening (with increased excitation intensity) to be prior to manifestation of any standard cubic nonlinearity (e.g. due to nonlinear curvature and inertial nonlinearities)

- High-fidelity modeling and experimental validation of piezoelectric energy harvesting with strong circuit nonlinearities due to AC-DC conversion in the presence of material and dissipative nonlinearities (Chapter 6);

- Establishment of a unified computationally efficient harmonic balance framework for geometrically, materially nonlinear non-conservative problems as well as systems involving circuit nonlinearities (Chapters 2-6) which can readily be implemented to other scenarios of multiple nonlinear effects;

- Accurate identification and consistent attribution of nonlinear quadratic dissipation effects in the problems of flexible configurations with large oscillations (e.g. velocity-squared fluid damping in the M-shaped configuration) and stiff piezoelectrics with small oscillations (e.g. displacement-squared solid damping in PZT-5A and PZT-5H in stiff bimorphs).

7.3 Suggested Future Work and Preliminary Results

7.3.1 Geometric Nonlinearities Caused by Large Deflections

In this dissertation, focus was placed on two types of systems: an M-shaped structure chosen for its strong nonlinear vibration behavior at low forcing amplitudes for resonant vibration energy harvesting bandwidth enhancement and geometrically linear piezoelectric bimorph cantilevers. The former design was primarily a proof of concept, and so the lumped

parameter model governing its dynamics was semi-empirical. The latter was intentionally chosen to be stiff, so as to have small vibration amplitudes and therefore no geometric nonlinearities. By eliminating geometric nonlinearities, material nonlinearities and intrinsic dissipative effects could be studied independently.

In some energy harvesting applications, ambient vibrations can be dominated by low frequency content. To target those lower frequencies with resonant energy harvesters, the compliance of the device must increase. As deflection amplitudes are greater with more compliant structures, the effect of geometric nonlinearity is increased. For compliant energy harvester designs, geometric, piezoelectric material, and circuit nonlinearities can be expected simultaneously. For compliant cantilever type designs, the governing dynamics can be derived from first principles and will result in a system of differential algebraic equations, if the full nonlinearity is retained. In the case of a geometrically nonlinear flexible cantilever, a proper inextensible cantilever beam theory with nonlinear curvature and inertial nonlinearities can be combined with piezoelectric material nonlinearities (Chapters 4) as well as circuit nonlinearities due to AC-DC conversion (Chapter 6) to obtain the complete framework. The method of harmonic balance (Appendices A and B) can be extended to solve such a system.

7.3.2 Material Nonlinearity of Hard Ceramic Piezoelectrics

In the modeling and parameter identification of piezoelectric material nonlinearities, the primary focus was placed on PZT-5A and PZT-5H, examples of soft and most popular piezoceramics. Soft ceramic piezoelectric materials are characterized by higher electromechanical coupling factors than hard ceramics at the expense of higher mechanical and dielectric losses. As shown in this dissertation, nonlinear internal dissipation in soft piezoceramics can be a dominant effect reducing energy harvesting performance. Hard ceramic piezoelectrics, like PZT-8, may be a better choice in some energy harvester designs, as their lower mechanical dissipation may overcome their lower levels of electromechanical coupling. Both hard and soft PZT exhibit a softening type nonlinearity, characterized by a resonant backbone curve that bends to lower frequencies at higher excitation amplitudes. Hardening stiffness

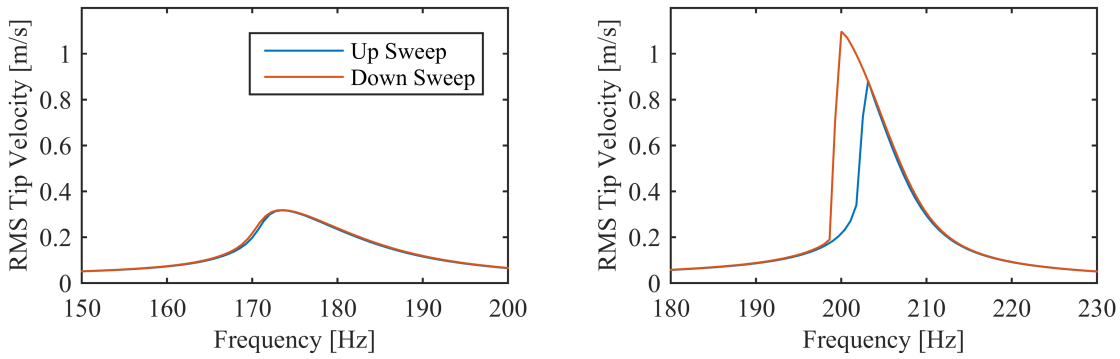

Figure 58: Comparison of unpoled soft PZT-5A (left) and unpoled hard PZT-8 (right). Samples are 35 mm long, 3 mm wide, 0.5 mm thick cantilever beams excited by base acceleration at $0.5g$ RMS. Hard PZT-8 exhibits much less mechanical dissipation and displays the jump phenomenon due to material softening stiffness nonlinearity, which can be exploited for bandwidth enhancement.

nonlinearities (as with the M-shaped oscillator) as well as softening stiffness nonlinearities can both produce the jump phenomenon, frequency response curve becomes multivalued at certain frequencies. Due to the high levels of nonlinear mechanical damping in PZT-5A and PZT-5H, the resonant peak is attenuated in amplitude and the jump phenomenon cannot occur. Higher quality factor hard ceramic PZT-8 can exhibit the jump phenomenon due to its softening nonlinearity. Figure 58 shows a preliminary test of an unpoled PZT-8 (right) cantilever with constant amplitude base acceleration excitation compared to a soft PZT-5A (left) cantilever of the same dimensions. As explained with regards the M-shaped oscillator and harvester, exploitation of the jump phenomenon can yield larger bandwidth in energy harvesting.

7.3.3 Internal Material and External Aerodynamic Damping Effects

Mechanical dissipation is caused by a variety of inherently nonlinear processes. Because dissipative effects are only important near resonances, and the study of vibrations has until recently been mostly concern with avoiding resonance behavior, linear viscous damping has been a widely used approximation due to its mathematical convenience. In more recent endeavors such as vibration energy harvesting and MEMS sensors, the goal is often to create structures that resonate by design. If these cases, high fidelity damping models are crucial. For in-air structural vibrations, other than joint (interface) effects and clamping

losses, there are two main causes of mechanical dissipation: internal material damping and external aerodynamic damping. Futhermore, both types tend to grow as quadratically with response amplitude, as shown in this dissertation by the quadratic material nonlinearity exhibited by soft ceramic piezoelectric materials. For this reason, it can be difficult to say with certainty what the cause of an observed nonlinear dissipative effect is. As demonstrated in this dissertation, electromechanical structures can be actuated in vacuum to remove any aerodynamic sources of dissipation so the relative contribution of internal damping can be observed. It was shown that for certain geometries of stiff piezoelectric cantilever, the dominant quadratic damping is internal. To extend this technique beyond situations of electrical excitation to base motion excitation common in experimental vibrations, the author designed and built a vacuum chamber electrodynamic shaker setup as a side project. Shown in Figure 59 are a photograph of the vacuum shaker setup and a comparison of nonlinear velocity response curves for the M-shaped energy harvester conducted at $0.05g$ RMS with shorted electrodes. As can be seen in the figure, reducing the air pressure and therefore the density of air around the vibrating structure, the already small amount of damping is further reduced, greatly increasing the response bandwidth and peak amplitude. (The artifacts in the frequency response curve are due to sub-optimal performance of the shaker controller, which will be discussed as another avenue of future work.) Since the air pressure inside the vacuum chamber can be varied from near full vacuum to atmospheric pressure, this setup provides a method for conducting structural vibrations experiments where the amount of damping is a controllable parameter.

7.3.4 Switching Circuit Nonlinearities

In this dissertation, analysis of effects caused by the inherently nonlinear process of rectification and power conditioning necessary for practical energy harvesting applications focused on the simplest case of a diode bridge rectifier, filter capacitor, and electrical load for standard AC-DC conversion in strongly coupled piezoelectric energy harvesters (in the presence of material and dissipative nonlinearities as well). A more advanced rectification and filtering circuit known as synchronous switched harvesting on inductor (SSHI) has been shown to

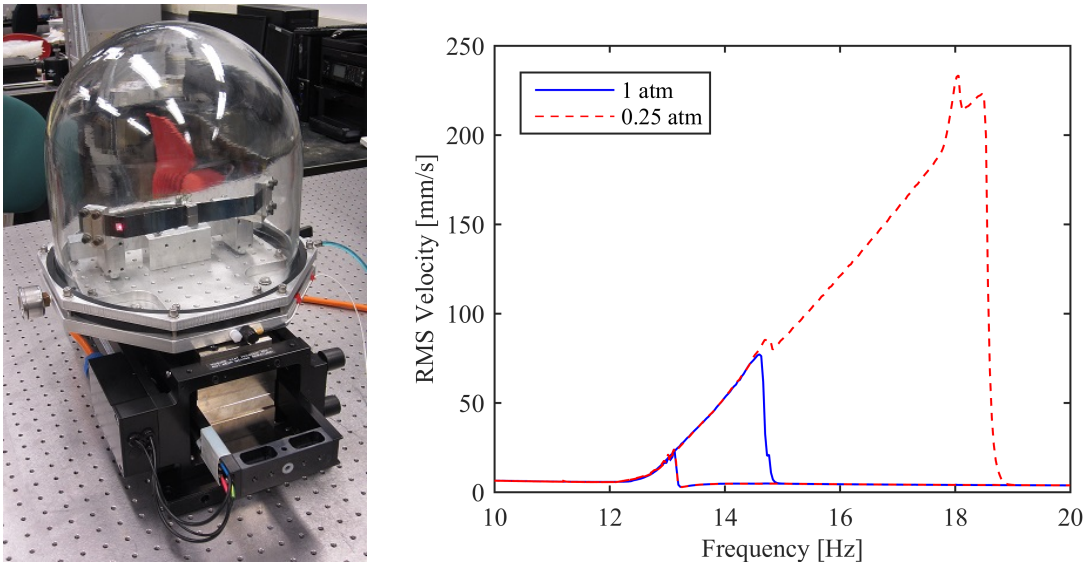

Figure 59: Photograph of vacuum shaker setup with the M-shaped oscillator (left) and comparison of the velocity response of the M-shaped oscillator at atmospheric (1 atm) and below atmospheric (0.25 atm) air pressure (right). Frequency sweeps conducted at $0.05g$ RMS.

increase the power conversion efficiency of weakly coupled piezoelectric energy harvesters. It adds a switched inductor in parallel with the piezoelectric transducer before rectification. If the switching conditions are consistent and known, and an adequate constitutive model for the transistor or other switching element can be obtained, the method of harmonic balance used in this dissertation can be readily applied. As with the circuit analyzed in this dissertation, such a harmonic balance solution based on physical models of nonlinear circuit elements will in fact be more accurate than idealized switching models that might be easier to implement in a circuit simulator and will certainly be substantially faster than time-domain numerical simulators especially for high-quality-factor systems.

7.3.5 Interface Tool Development for the Harmonic Balance Method

The method of harmonic balance has been used extensively in the work detailed in this dissertation. While originally devised as a means to analyze nonlinear circuitry[51, 15, 49], it can be applied to find periodic solutions of all types of nonlinear dynamical systems. As mentioned, this method has a number of advantages over other methods of finding approximate solutions of ordinary differential equations (ODEs), the method of multiple

times scales chief among them.

First, the harmonic balance method is rigorous and valid for both weakly and strongly nonlinear systems, and does not require the introduction of extra bookkeeping parameters (e.g. the method of multiple scales), which oftentimes have no well-defined process to select their values.

Second, the harmonic balance method is scalable in accuracy similar to the assumed modes or Galerkin process for spatially discretizing partial differential equations. With a proper general harmonic balance solver as presented in the appendices, the number of frequency components to include in the approximate solution can be chosen as simply as changing a parameter in a MATLAB script, whereas a solution found via the method of multiple scales would have to be rederived with additional algebraic toil if a higher order perturbation solution is deemed necessary.

Third, the method of multiple scales can be fast, especially when the produced system of algebraic equations can be solved with a fast numerical root-finding algorithm, such as with the Newton-Raphson method presented in this dissertation. Numerical simulation of ordinary differential equations has become a powerful and widespread tool for scientists and engineers, with the "odexx" solvers in MATLAB representing some of its most useful built-in functionality. For the fields of vibrations, controls, dynamics, electronics, and others, periodic solutions of governing ordinary differential equations are often sought. This means that typical time-marching numerical integration schemes waste computation time simulating transient effects before they decay leaving steady-state or limit cycle behavior. The benefit of a frequency domain simulation is especially pronounced for high quality factor systems, in which transient effects take many cycles to decay. Simulation of systems in the frequency domain directly, as with the method of harmonic balance, are precisely suited to these types of analyses, especially those involving forced motions of dissipative systems that are so common in engineering applications.

It would therefore be a huge benefit for more polished and robust general harmonic balance solvers than the one presented here to be included in all scientific and engineering

scripting packages like MATLAB. The method of harmonic balance presented in this dissertation, uses the Newton-Raphson method to find periodic orbits of ordinary differential equations. Depending on the application, different numerical root-finding methods may be better suited. Additionally, the method of harmonic balance may also be used to solve differential algebraic equations (DAEs), which govern dynamical systems with additional algebraic constraint equations, and delay differential equations (DDEs), in which the rate of change of the system can depend on time, the current state, as well as past states. In the same way the "odexx" MATLAB solvers greatly simplify time-domain simulations and give users a variety of options to fine-tune their performance, a family of harmonic balance solvers for various types of governing equations with options to tweak performance would greatly simplify frequency-domain simulations.

7.3.6 Robustness Enhancement of Shaker Controllers for Nonlinear Vibrations Experiments

This last suggested future work is rather regarding the measurement methodology using controlled electrodynamic shakers for nonlinear vibrating systems. As conducted numerous times in the work presented for this dissertation, a typical vibrations experiment uses mechanical excitation provided by an electrodynamic shaker to provide forcing to a structure, the motion of which is then measured. Since superposition holds for linear vibrations, the type of forcing can include broadband signals like noise, multiharmonic signals, or chirp signals. From measurements of the input and output, frequency response functions (FRFs) can be calculated. The resulting FRFs compactly contain a complete description of the system. Because FRFs are so useful in linear vibrations, the notion is extended to nonlinear vibrations. An input to the system is provided as harmonic signal at a specified amplitude. The system response will either be a periodic signal with a period an integer multiple of the period of the input signal or chaotic. For quasi-linear systems, the response will be a periodic signal with harmonic content with the same period as the input signal. In nonlinear controls terminology, these quasi-linear systems are modeled by "sine input describing functions" (SIDFs) and "higher order sine input describing functions" (HOSIDFs).

To conduct a practical nonlinear vibrations experiment, the frequency of the sinusoidal input is continuously varied over a range at a rate slow enough to yield quasi-steady-state conditions.

For a proper nonlinear vibrations experiment, the output of the electrodynamic shaker should be as close to the ideal constant amplitude sinusoid as possible. As demonstrated in this dissertation, a vibration controller can be used for this. The vibration controller generates a control voltage, which through a power amplifier powers the shaker. The vibration controller picks the control voltage to minimize the error between a measured kinematic variable on a structure to a reference signal. In the nonlinear energy harvesting experiments in this dissertation, the kinematic variable of interest is the acceleration of the harvester base. The base acceleration is measured with an accelerometer and the reference acceleration is a constant amplitude sinusoid with a slowly varying frequency. Oftentimes, the shaker is assumed to be a high mechanical impedance energy source, wherein reaction forces from the device under test (DUT) do not significantly affect its motion. In reality, the shaker is a non-ideal (finite impedance) source with motion coupled to the behavior of the DUT.

If the vibration controller is functioning well, it will adjust the control voltage based on the measured kinematic variable to cancel out the disturbance caused by the motion of the DUT. If the power amplifier, shaker, and DUT are behaving in a linear fashion (the power amplifier and shaker are very close to linear systems by design), the control voltage and the disturbance forcing on the shaker that the DUT creates will be sinusoidal at the same frequency as the reference signal. This means the controller need only adjust the magnitude and phase of the control voltage to cancel out the disturbance. For nonlinear vibrations experiments, the DUT acts in a nonlinear fashion, generating disturbance forces with higher harmonic content. A proper vibration controller would then produce a control voltage also containing harmonic content to cancel out those disturbances.

From extensive nonlinear vibrations experimentation done in this dissertation, it has become clear the state-of-the-art in vibration controllers, represented by a Spektra VCS 201 Vibration Control System, does not function in the desired way described above. On the vibration controller input, which accepts the measured acceleration signal, there is a low

pass filter. Common as they are, a low pass filter here hides the unwanted higher harmonic content from the controller logic. It then only seeks to minimize the error of the fundamental frequency of the measured acceleration with respect to the reference acceleration.

For instance, secondary resonance experiments can pose a challenge, as the response signal of interest is dominated by a harmonic of input signal. As shown in the superharmonic resonance investigations of the M-shaped energy harvester in Chapter 3, harmonic distortion in the system input generated by the controlled shaker can significantly complicate experiment, and potentially mask interesting behavior.

A more robust and high-fidelity vibration control unit would adjust harmonics in the control voltage to properly reject all harmonics in the disturbance forcing caused by the DUT, ensuring the controlled input signal for nonlinear vibration experiments is as sinusoidal as possible.

Appendix A

THEORY OF A NEWTON'S METHOD ENABLED HARMONIC BALANCE METHOD

A.1 Problem Statement

Given a D-dimensional system that is periodic in time with period T,

$$\dot{\mathbf{x}} = \mathbf{f}(t, \mathbf{x}) = \mathbf{f}(t + T, \mathbf{x}), \tag{180}$$

or in component form,

$$\dot{x}_i = f_i(t, \mathbf{x}) = f_i(t + T, \mathbf{x}), \tag{181}$$

with indices

$$i, j \in [1, 2, \ldots, D], \tag{182}$$

periodic solutions, $\mathbf{x}(t)$, are sought such that

$$\mathbf{x}(t) = \mathbf{x}(t + T). \tag{183}$$

A.2 Assumed Solution

A Fourier series solution is assumed,

$$\hat{\mathbf{x}}(t) = \mathbf{a} + \mathbf{A}\mathbf{c}(t) + \mathbf{B}\mathbf{s}(t), \tag{184}$$

where a is a constant vector, $\mathbf{A}$ and $\mathbf{B}$ are constant matrices, and $\mathbf{c}(t)$ and $\mathbf{s}(t)$ are vectors of cosines and sines of harmonics. In component form

$$\hat{x}_i(t) = a_i + \sum_{m=1}^{M} \left[A_{im} c_m(t) + B_{im} s_m(t) \right], \tag{185}$$

with indices,

$$m, n \in [1, 2, \ldots, M], \tag{186}$$

$$\begin{aligned} c_m(t) &= \cos\left(\frac{2\pi m t}{T}\right) \\ s_m(t) &= \sin\left(\frac{2\pi m t}{T}\right) \end{aligned} \tag{187}$$

Here, M, is the number of harmonics included in the truncated Fourier series solution. The derivative of $\mathbf{x}(t)$ can be written:

$$\dot{\hat{x}}_i = \sum_{m=1}^{M} \frac{2\pi m}{T} \left[-A_{im} s_m(t) + B_{im} c_m(t) \right]. \tag{188}$$

A.3 Residual

Substituting the assumed solution, $\hat{\mathbf{x}}(t)$, into the governing equations, $\mathbf{f}(t, \mathbf{x})$, yields the approximate system,

$$\hat{\mathbf{f}}(t) = \mathbf{f}(t, \hat{\mathbf{x}}(t)). \tag{189}$$

The error vector of the approximate governing equations is called the residual and defined as,

$$\mathbf{r}(t) = \hat{\mathbf{f}}(t) - \dot{\hat{\mathbf{x}}}(t). \tag{190}$$

Minimizing the residual function in the Galerkin method sense gives the equations:

$$\begin{aligned}
\mathbf{r^a}(\mathbf{a}, \mathbf{A}, \mathbf{B}) &= \frac{1}{T} \int_0^T \mathbf{r}(t) dt = \frac{1}{T} \int_0^T \left[\hat{\mathbf{f}}(t) - \dot{\hat{\mathbf{x}}}(t) \right] dt = \mathbf{0} \\
\mathbf{R^A}(\mathbf{a}, \mathbf{A}, \mathbf{B}) &= \frac{1}{T} \int_0^T \mathbf{r}(t) \mathbf{c}^\top(t) dt = \frac{1}{T} \int_0^T \left[\hat{\mathbf{f}}(t) - \dot{\hat{\mathbf{x}}}(t) \right] \mathbf{c}^\top(t) dt = \mathbf{0} \\
\mathbf{R^B}(\mathbf{a}, \mathbf{A}, \mathbf{B}) &= \frac{1}{T} \int_0^T \mathbf{r}(t) \mathbf{s}^\top(t) dt = \frac{1}{T} \int_0^T \left[\hat{\mathbf{f}}(t) - \dot{\hat{\mathbf{x}}}(t) \right] \mathbf{s}^\top(t) dt = \mathbf{0}.
\end{aligned} \tag{191}$$

These equations can written in component form as:

$$\begin{aligned}
r_i^{\mathbf{a}} &= \frac{1}{T} \int_0^T \left[\hat{f}_i(t) - \dot{\hat{x}}_i(t) \right] dt = 0 \\
R_{im}^{\mathbf{A}} &= \frac{1}{T} \int_0^T \left[\hat{f}_i(t) - \dot{\hat{x}}_i(t) \right] c_m(t) dt = 0 \\
R_{im}^{\mathbf{B}} &= \frac{1}{T} \int_0^T \left[\hat{f}_i(t) - \dot{\hat{x}}_i(t) \right] s_m(t) dt = 0,
\end{aligned} \tag{192}$$

which can be simplified to:

$$\begin{aligned}
r_i^{\mathbf{a}} &= \frac{1}{T} \int_0^T \hat{f}_i(t) dt = 0 \\
R_{im}^{\mathbf{A}} &= \frac{1}{T} \int_0^T \hat{f}_i(t) c_m(t) dt - \frac{\pi m}{T} B_{im} = 0 \\
R_{im}^{\mathbf{B}} &= \frac{1}{T} \int_0^T \hat{f}_i(t) s_m(t) dt + \frac{\pi m}{T} A_{im} = 0.
\end{aligned} \tag{193}$$

This is a system of $D(2M+1)$ unknowns that can be solved for the correct $\mathbf{a}$, $\mathbf{A}$, and $\mathbf{B}$.

A.4 Derivatives of the Residual

To use Newton's method to solve the above system of equations, the derivatives of the residual functions are needed. First the approximate gradient matrix is defined as, $\hat{\mathbf{G}}(t) = [\hat{G}_{ij}(t)]$. More precisely,

$$\hat{G}_{ij}(t) = \left.\frac{\partial f_i}{\partial x_j}\right|_{t,\hat{\mathbf{x}}(t)}. \tag{194}$$

The derivatives of the residual with respect to the unknown Fourier components can then be written in component form as:

$$\begin{aligned}
J_{ij}^{\mathbf{aa}} = \frac{\partial r_i^{\mathbf{a}}}{\partial a_j} &= \frac{1}{T}\int_0^T \hat{G}_{ij}(t)dt \\
J_{inj}^{\mathbf{aA}} = \frac{\partial r_i^{\mathbf{a}}}{\partial A_{jn}} &= \frac{1}{T}\int_0^T \hat{G}_{ij}(t)c_n(t)dt \\
J_{inj}^{\mathbf{aB}} = \frac{\partial r_i^{\mathbf{a}}}{\partial B_{jn}} &= \frac{1}{T}\int_0^T \hat{G}_{ij}(t)s_n(t)dt \\
J_{imj}^{\mathbf{Aa}} = \frac{\partial R_{im}^{\mathbf{A}}}{\partial a_j} &= \frac{1}{T}\int_0^T \hat{G}_{ij}(t)c_m(t)dt \\
J_{imnj}^{\mathbf{AA}} = \frac{\partial R_{im}^{\mathbf{A}}}{\partial A_{jn}} &= \frac{1}{T}\int_0^T \hat{G}_{ij}(t)c_m(t)c_n(t)dt \\
&= \frac{1}{2T}\int_0^T \hat{G}_{ij}(t)\left[c_\mu(t) + c_\nu(t)\right]dt \\
J_{imnj}^{\mathbf{AB}} = \frac{\partial R_{im}^{\mathbf{A}}}{\partial B_{jn}} &= \frac{1}{T}\int_0^T \hat{G}_{ij}(t)c_m(t)s_n(t)dt - \frac{\pi m}{T}\delta_{ij}\delta_{mn} \\
&= \frac{1}{2T}\int_0^T \hat{G}_{ij}(t)\left[s_\mu(t) - s_\nu(t)\right]dt - \frac{\pi m}{T}\delta_{ij}\delta_{mn} \\
J_{imj}^{\mathbf{Ba}} = \frac{\partial R_{im}^{\mathbf{B}}}{\partial a_j} &= \frac{1}{T}\int_0^T \hat{G}_{ij}(t)s_m(t)dt \\
J_{imnj}^{\mathbf{BA}} = \frac{\partial R_{im}^{\mathbf{B}}}{\partial A_{jn}} &= \frac{1}{T}\int_0^T \hat{G}_{ij}(t)s_m(t)c_n(t)dt + \frac{\pi m}{T}\delta_{ij}\delta_{mn} \\
&= \frac{1}{2T}\int_0^T \hat{G}_{ij}(t)\left[s_\mu(t) + s_\nu(t)\right]dt + \frac{\pi m}{T}\delta_{ij}\delta_{mn} \\
J_{imnj}^{\mathbf{BB}} = \frac{\partial R_{im}^{\mathbf{B}}}{\partial B_{jn}} &= \frac{1}{T}\int_0^T \hat{G}_{ij}(t)s_m(t)s_n(t)dt \\
&= \frac{1}{2T}\int_0^T \hat{G}_{ij}(t)\left[-c_\mu(t) + c_\nu(t)\right]dt.
\end{aligned} \tag{195}$$

Here the indices μ and ν are defined by:

$$\begin{aligned}\mu &= m + n \\ \nu &= m - n.\end{aligned} \tag{196}$$

To speed up computation, all of the numerical integrations above can be computed using fast Fourier transforms (FFTs).

A.5 Cast in Vector Form

To solve this problem in MATLAB, the unknowns should be reorganized as a single vector and the Jacobians as a single matrix, rather than a number of vectors, two, three, and four dimensional matrices. New indices, p and q, can be defined where:

$$p, q \in [1 \ldots D(2M+1)]. \tag{197}$$

These indices can be partitioned in the following way:

$$\begin{aligned}p &= \left\{ \begin{array}{ccc} p^{\mathbf{a}} & p^{\mathbf{A}} & p^{\mathbf{B}} \end{array} \right\} \\ q &= \left\{ \begin{array}{ccc} q^{\mathbf{a}} & q^{\mathbf{A}} & q^{\mathbf{B}} \end{array} \right\}.\end{aligned} \tag{198}$$

These indices are functions of i, j, m, and n, i.e.

$$\begin{aligned}p^{\mathbf{a}} &= i \\ p^{\mathbf{A}} &= i + Dm \\ p^{\mathbf{B}} &= i + D(M+m) \\ q^{\mathbf{a}} &= j \\ q^{\mathbf{A}} &= j + Dn \\ q^{\mathbf{B}} &= j + D(M+n)\end{aligned} \tag{199}$$

The vector of unknowns and the Jacobian matrix that we will use for Newton's method can then be defined as:

$$\mathbf{u} = [u_p] = \left[\begin{array}{ccccc} a_i & \vdots & A_{im} & \vdots & B_{im} \end{array} \right]^{\top} \tag{200}$$

$$\mathbf{v} = [v_p] = \begin{bmatrix} r_i^{\mathbf{a}} & \vdots & R_{im}^{\mathbf{A}} & \vdots & R_{im}^{\mathbf{B}} \end{bmatrix}^\top \tag{201}$$

$$\mathbf{W} = [W_{pq}] = \begin{bmatrix} J_{ij}^{\mathbf{aa}} & \vdots & J_{inj}^{\mathbf{aA}} & \vdots & J_{inj}^{\mathbf{aB}} \\ \cdots & & \cdots & & \cdots \\ J_{imj}^{\mathbf{Aa}} & \vdots & J_{imnj}^{\mathbf{AA}} & \vdots & J_{imnj}^{\mathbf{AB}} \\ \cdots & & \cdots & & \cdots \\ J_{imj}^{\mathbf{Ba}} & \vdots & J_{imnj}^{\mathbf{BA}} & \vdots & J_{imnj}^{\mathbf{BB}} \end{bmatrix}. \tag{202}$$

With these defined, one iteration of Newton's Method is completed by calculating $\Delta\mathbf{u}$, the change to the estimate of $\mathbf{u}$ as:

$$\Delta\mathbf{u} = -\mathbf{W}^{+}\mathbf{v}, \tag{203}$$

where $\mathbf{W}^{+}$ is the Moore-Penrose pseudoinverse of $\mathbf{W}$. This is preferred over Gaussian elimination for numerical stability as $\mathbf{W}$ can be ill-conditioned. If $\Delta\mathbf{u}$ is sufficiently small, no more iterations of Newton's method are necessary. The vector, $\mathbf{u}$ is updated,

$$\mathbf{u}' = \mathbf{u} + \Delta\mathbf{u}. \tag{204}$$

Then $\mathbf{u}'$ is "unpacked" to find the updated unknowns, $\mathbf{a}'$, $\mathbf{A}'$, and $\mathbf{B}'$, which are used to find the updated approximate periodic solution, $\hat{\mathbf{x}}'(t)$,

$$\hat{\mathbf{x}}'(t) = \mathbf{a}' + \mathbf{A}'\mathbf{c}(t) + \mathbf{B}'\mathbf{s}(t). \tag{205}$$

This process can be initialized with randomized components of $\mathbf{a}$, $\mathbf{A}$, and $\mathbf{B}$, or perhaps with the known solution to a similar system (e.g. a linear system or a simpler nonlinear system).

Appendix B

MATLAB IMPLEMENTATION OF A NEWTON'S METHOD ENABLED HARMONIC BALANCE METHOD

```
function [a,A,B,x0] = hbnewton(f,dfdx,T,n,a0,A0,B0,tol)

%f: function handle for dynamical system, f = f(t,x) = f(t+T,x)
%dfdx: function handle for gradient of f, [dfdx]_ij = dfi/dxj
%T: period of orbit desired, x(t) = x(t+T)
%n: Sampling Factor, n>2 to satisfy Nyquist criterion
%a0: initial constant vector
%A0: initial cosine coefficent matrix
%B0: initial sine coefficient matrix
%D is dimension of state space
%M is number of harmonics in truncated Fourier series
[D,M] = size(A0);

%initialize solution vectors/matrices
a = a0;
A = A0;
B = B0;

NFFT = 2^nextpow2(n*M);
dt = T/NFFT;
ts = 0:dt:(T-dt);
fs = zeros(D,NFFT);
gs = zeros(D,D,NFFT);

m = (1:M)'; %column vector of harmonic numbers m = [1...M]

%multi harmonic cosine and sine functions
c = @(t) cos(2*pi*m*t/T);
s = @(t) sin(2*pi*m*t/T);

%approximate solution function handle
x = @(a,A,B,t) a + A*c(t) + B*s(t);

%initialize Jacobians
Jaa = zeros(D,D);
JaA = zeros(D,M,D);
JaB = zeros(D,M,D);
JAa = zeros(D,M,D);
JAA = zeros(D,M,M,D);
JAB = zeros(D,M,M,D);
JBa = zeros(D,M,D);
JBA = zeros(D,M,M,D);
JBB = zeros(D,M,M,D);
```

```
MaxIter = 1000;
for kk=1:MaxIter
    if kk==MaxIter
        error('Maxiumum Newton method iterations reached. Convergence unlikely.')
    end

    %Time sampled system and Jacobian
    for mfft=1:NFFT
        fs(:,mfft) = f(ts(mfft),x(a,A,B,ts(mfft)));
        gs(:,:,mfft) = dfdx(ts(mfft),x(a,A,B,ts(mfft)));
    end
    F = fft(fs,NFFT,2)/NFFT;
    G = fft(gs,NFFT,3)/NFFT;

    %Residuals
    ra =  real(F(:,1));
    RA =  real(F(:,2:(M+1))) - B*diag(pi*m)/T;
    RB = -imag(F(:,2:(M+1))) + A*diag(pi*m)/T;

    %Jacobians
    Jaa(:,:) = real(G(:,:,1));
    for mm=1:M
        nn = mm;
        JAa(:,mm,:) =  real(G(:,:,mm+1));
        JBa(:,mm,:) = -imag(G(:,:,mm+1));
        JaA(:,nn,:) =  real(G(:,:,nn+1));
        JaB(:,nn,:) = -imag(G(:,:,nn+1));
    end

    for mm=1:M
        for nn=1:M
            mu = mm+nn;
            nu = mm-nn;
            if nu>0
                JAA(:,mm,nn,:) =  (real(G(:,:,mu+1))+real(G(:,:,nu+1)))/2;
                JAB(:,mm,nn,:) = (-imag(G(:,:,mu+1))+imag(G(:,:,nu+1)))/2 ...
                    - (pi*mm/T)*eye(D)*(mm==nn);
                JBA(:,mm,nn,:) = (-imag(G(:,:,mu+1))-imag(G(:,:,nu+1)))/2 ...
                    + (pi*mm/T)*eye(D)*(mm==nn);
                JBB(:,mm,nn,:) = (-real(G(:,:,mu+1))+real(G(:,:,nu+1)))/2;
            else
                JAA(:,mm,nn,:) =  (real(G(:,:,mu+1))+real(G(:,:,-nu+1)))/2;
                JAB(:,mm,nn,:) = (-imag(G(:,:,mu+1))-imag(G(:,:,-nu+1)))/2 ...
                    - (pi*mm/T)*eye(D)*(mm==nn);
                JBA(:,mm,nn,:) = (-imag(G(:,:,mu+1))+imag(G(:,:,-nu+1)))/2 ...
                    + (pi*mm/T)*eye(D)*(mm==nn);
                JBB(:,mm,nn,:) = (-real(G(:,:,mu+1))+real(G(:,:,-nu+1)))/2;
            end
        end
    end
```

```
%initialize Newton's method
u = zeros(D*(2*M+1),1); %vector of unknowns
v = zeros(D*(2*M+1),1); %vector of residuals
W = zeros(D*(2*M+1));   %Jacobian matrix

%Pack up unknowns and residuals
for ii = 1:D
    pa = ii;
    u(pa) = a(ii);
    v(pa) = ra(ii);
    for mm = 1:M
        pA = ii+D*mm;
        pB = ii+D*(M+mm);
        u(pA) = A(ii,mm);
        u(pB) = B(ii,mm);
        v(pA) = RA(ii,mm);
        v(pB) = RB(ii,mm);
    end
end

for ii=1:D
    pa = ii;
    for jj=1:D
        qa = jj;
        W(pa,qa) = Jaa(ii,jj);
    end
end

for mm=1:M
    for ii=1:D
        pA = ii+D*mm;
        pB = ii+D*(M+mm);
        for jj=1:D
            qa = jj;
            W(pA,qa) = JAa(ii,mm,jj);
            W(pB,qa) = JBa(ii,mm,jj);
        end
    end
end

for nn=1:M
    for jj=1:D
        qA = jj+D*nn;
        qB = jj+D*(M+nn);
        for ii=1:D
            pa = ii;
            W(pa,qA) = JaA(ii,nn,jj);
            W(pa,qB) = JaB(ii,nn,jj);
        end
    end
end
```

```
    for mm=1:M
        for ii=1:D
            pA = ii+D*mm;
            pB = ii+D*(M+mm);
            for nn=1:M
                for jj=1:D
                    qA = jj+D*nn;
                    qB = jj+D*(M+nn);
                    W(pA,qA) = JAA(ii,mm,nn,jj);
                    W(pA,qB) = JAB(ii,mm,nn,jj);
                    W(pB,qA) = JBA(ii,mm,nn,jj);
                    W(pB,qB) = JBB(ii,mm,nn,jj);
                end
            end
        end
    end

    %Newton method iteration
    du = -pinv(W)*v; %Pseudo-Inverse
   %du = -W\v;       %Gaussian Elimination
    uplus = u + du;

    %Unpack unknowns
    for ii = 1:D
        pa = ii;
        a(ii) = uplus(pa);
        for mm = 1:M
            pA = ii+D*mm;
            pB = ii+D*(M+mm);
            A(ii,mm) = uplus(pA);
            B(ii,mm) = uplus(pB);
        end
    end

    %calculate  error
    err = max(abs(du));
    if err<tol
        break
    end

end

%output initial condition
x0 = x(a,A,B,0);

end
```

REFERENCES

[1] Abdelkefi, A., Nayfeh, A. H., and Hajj, M. R., "Effects of nonlinear piezoelectric coupling on energy harvesters under direct excitation," *Nonlinear Dynamics*, vol. 67, no. 2, pp. 1221–1232, 2011.

[2] Abdelkefi, A., Nayfeh, A. H., and Hajj, M. R., "Global nonlinear distributed-parameter model of parametrically excited piezoelectric energy harvesters," *Nonlinear Dynamics*, vol. 67, no. 2, pp. 1147–1160, 2011.

[3] Adhikari, S., Friswell, M. I., and Inman, D. J., "Piezoelectric energy harvesting from broadband random vibrations," *Smart Materials & Structures*, vol. 18, no. 11, p. 115005, 2009. 508CQ Times Cited:81 Cited References Count:30.

[4] Adly, A., Davino, D., Giustiniani, A., and Visone, C., "Experimental tests of a magnetostrictive energy harvesting device toward its modeling," *Journal of Applied Physics*, vol. 107, no. 9, 2010.

[5] Albareda, A., Gonnard, P., Perrin, V., Briot, R., and Guyomar, D., "Characterization of the mechanical nonlinear behavior of piezoelectric ceramics," *IEEE Trans Ultrason Ferroelectr Freq Control*, vol. 47, no. 4, pp. 844–53, 2000.

[6] Ali, S. F., Adhikari, S., Friswell, M. I., and Narayanan, S., "The analysis of piezomagnetoelastic energy harvesters under broadband random excitations," *Journal of Applied Physics*, vol. 109, no. 7, p. 074904, 2011.

[7] Anton, S., Farinholt, K., and Erturk, A., "Piezoelectret foam–based vibration energy harvesting," *Journal of Intelligent Material Systems and Structures*, p. 1045389X14541501, 2014.

[8] Anton, S. R. and Sodano, H. A., "A review of power harvesting using piezoelectric materials (20032006)," *Smart Materials and Structures*, vol. 16, no. 3, p. R1, 2007.

[9] Arnold, D. P., "Review of microscale magnetic power generation," *IEEE Transactions on Magnetics*, vol. 43, no. 11, pp. 3940–3951, 2007.

[10] Arrieta, A. F., Hagedorn, P., Erturk, A., and Inman, D. J., "A piezoelectric bistable plate for nonlinear broadband energy harvesting," *Applied Physics Letters*, vol. 97, no. 10, p. 104102, 2010.

[11] Aureli, M., Prince, C., Porfiri, M., and Peterson, S. D., "Energy harvesting from base excitation of ionic polymer metal composites in fluid environments," *Smart Materials & Structures*, vol. 19, no. 1, p. 015003, 2010.

[12] Aurelle, N., Guyomar, D., Richard, C., Gonnard, P., and Eyraud, L., "Nonlinear behavior of an ultrasonic transducer," *Ultrasonics*, vol. 34, no. 2-5, pp. 187–191, 1996.

[13] Bandstra, J. P., "Comparison of equivalent viscous damping and nonlinear damping in discrete and continuous vibrating systems," *Journal of Vibration Acoustics Stress and Reliability in Design-Transactions of the ASME*, vol. 105, no. 3, pp. 382–392, 1983.

[14] Barton, D. A., Burrow, S. G., and Clare, L. R., "Energy harvesting from vibrations with a nonlinear oscillator," *Journal of Vibration and Acoustics*, vol. 132, no. 2, p. 021009, 2010.

[15] Bogoliubov, N. N. and Mitropolsky, Y. A., *Asymptotic methods in the theory of non-linear oscillations*, vol. 10. CRC Press, 1961.

[16] Burrow, S. G., Clare, L. R., Carrella, A., and Barton, D., "Vibration energy harvesters with non-linear compliance," *Active and Passive Smart Structures and Integrated Systems 2008*, vol. 6928, pp. 92807–92807, 2008.

[17] Burrow, S. G., Mitcheson, P. D., and Stark, B. H., *Power Conditioning Techniques for Energy Harvesting*, pp. 323–343. Springer, 2013.

[18] Cook-Chennault, K. A., Thambi, N., and Sastry, A. M., "Powering mems portable devicesa review of non-regenerative and regenerative power supply systems with special emphasis on piezoelectric energy harvesting systems," *Smart Materials and Structures*, vol. 17, no. 4, p. 043001, 2008.

[19] Cottone, F., Vocca, H., and Gammaitoni, L., "Nonlinear energy harvesting," *Phys Rev Lett*, vol. 102, no. 8, p. 080601, 2009.

[20] Crandall, S. H., *Dynamics of Mechanical and Electromechanical Systems*. New York: McGraw-Hill, 1968.

[21] Damjanovic, D., "Hysteresis in piezoelectric and ferroelectric materials," *The science of hysteresis*, vol. 3, pp. 337–465, 2005.

[22] Daqaq, M. F., "Response of uni-modal duffing-type harvesters to random forced excitations," *Journal of Sound and Vibration*, vol. 329, no. 18, pp. 3621–3631, 2010.

[23] Daqaq, M. F., "Transduction of a bistable inductive generator driven by white and exponentially correlated gaussian noise," *Journal of Sound and Vibration*, vol. 330, no. 11, pp. 2554–2564, 2011.

[24] Daqaq, M. F., Masana, R., Erturk, A., and Quinn, D. D., "On the role of nonlinearities in vibratory energy harvesting: A critical review and discussion," *Applied Mechanics Reviews*, vol. 66, no. 4, p. 040801, 2014.

[25] De Marqui Junior, C., Erturk, A., and Inman, D. J., "An electromechanical finite element model for piezoelectric energy harvester plates," *Journal of Sound and Vibration*, vol. 327, no. 1-2, pp. 9–25, 2009.

[26] Deng, Q., Kammoun, M., Erturk, A., and Sharma, P., "Nanoscale flexoelectric energy harvesting," *International Journal of Solids and Structures*, vol. 51, no. 18, pp. 3218–3225, 2014. Am8qc Times Cited:1 Cited References Count:70.

[27] Dutoit, N. E. and Wardle, B. L., "Experimental verification of models for microfabricated piezoelectric vibration energy harvesters," *AIAA Journal*, vol. 45, no. 5, pp. 1126–1137, 2007.

[28] Elvin, N. G. and Elvin, A. A., "A general equivalent circuit model for piezoelectric generators," *Journal of Intelligent Material Systems and Structures*, vol. 20, no. 1, pp. 3–9, 2009.

[29] Elvin, N. G. and Elvin, A. A., "An experimentally validated electromagnetic energy harvester," *Journal of Sound and Vibration*, vol. 330, no. 10, pp. 2314–2324, 2011.

[30] Elvin, N. and Erturk, A., *Advances in energy harvesting methods*. Springer, 2013.

[31] Erturk, A., Hoffmann, J., and Inman, D. J., "A piezomagnetoelastic structure for broadband vibration energy harvesting," *Applied Physics Letters*, vol. 94, no. 25, 2009.

[32] Erturk, A. and Inman, D. J., "An experimentally validated bimorph cantilever model for piezoelectric energy harvesting from base excitations," *Smart Materials & Structures*, vol. 18, no. 2, 2009.

[33] Erturk, A. and Inman, D. J., "Broadband piezoelectric power generation on high-energy orbits of the bistable duffing oscillator with electromechanical coupling," *Journal of Sound and Vibration*, vol. 330, no. 10, pp. 2339–2353, 2011.

[34] Erturk, A. and Inman, D. J., *Piezoelectric Energy Harvesting*. John Wiley & Sons, 2011.

[35] Gammaitoni, L., Neri, I., and Vocca, H., "Nonlinear oscillators for vibration energy harvesting," *Applied Physics Letters*, vol. 94, no. 16, 2009.

[36] Ghandchi Tehrani, M. and Elliott, S. J., "Extending the dynamic range of an energy harvester using nonlinear damping," *Journal of Sound and Vibration*, vol. 333, no. 3, pp. 623–629, 2014.

[37] Glynne-Jones, P., Tudor, M. J., Beeby, S. P., and White, N. M., "An electromagnetic, vibration-powered generator for intelligent sensor systems," *Sensors and Actuators a-Physical*, vol. 110, no. 1-3, pp. 344–349, 2004.

[38] Goldschmidtboeing, F., Eichhorn, C., Wischke, M., Kroener, M., and Woias, P., "The influence of ferroelastic hysteresis on mechanically excited pzt cantilever beams," in *Proceedings of the 11th International Workshop on Micro and Nanotechnology for Power Generation and Energy Conversion Applications*, pp. 114–117, 2011.

[39] Gottlieb, O. and Wolf, K., "Nonlinear dynamics of a cantilever beam actuated by piezoelectric layers in symmetric and assymetric configuration," *Technion-Isreael Institute of Technology, Technical Report ETR-2001-02*, 2001.

[40] Green, P. L., Worden, K., Atallah, K., and Sims, N. D., "The benefits of duffing-type nonlinearities and electrical optimisation of a mono-stable energy harvester under white gaussian excitations," *Journal of Sound and Vibration*, vol. 331, no. 20, pp. 4504–4517, 2012.

[41] Guckenheimer, J. and Holmes, P., *Nonlinear oscillations, dynamical systems, and bifurcations of vector fields*, vol. 42. New York Springer Verlag, 1983.

[42] Guyomar, D., Aurelle, N., and Eyraud, L., "Piezoelectric ceramics nonlinear behavior. application to langevin transducer," *Journal De Physique III*, vol. 7, no. 6, pp. 1197–1208, 1997.

[43] Guyomar, D., Badel, A., Lefeuvre, E., and Richard, C., "Toward energy harvesting using active materials and conversion improvement by nonlinear processing," *Ultrasonics, Ferroelectrics and Frequency Control, IEEE Transactions on*, vol. 52, no. 4, pp. 584–595, 2005.

[44] Harne, R. L. and Wang, K. W., "A review of the recent research on vibration energy harvesting via bistable systems," *Smart Materials and Structures*, vol. 22, no. 2, p. 023001, 2013.

[45] Hu, Y., Xue, H., Yang, J., and Jiang, Q., "Nonlinear behavior of a piezoelectric power harvester near resonance," *IEEE Trans Ultrason Ferroelectr Freq Control*, vol. 53, no. 7, pp. 1387–91, 2006.

[46] Kamlah, M., "Ferroelectric and ferroelastic piezoceramics modeling of electromechanical hysteresis phenomena," *Continuum Mechanics and Thermodynamics*, vol. 13, no. 4, pp. 219–268, 2001.

[47] Kong, N., Ha, D. S., Erturk, A., and Inman, D. J., "Resistive impedance matching circuit for piezoelectric energy harvesting," *Journal of Intelligent Material Systems and Structures*, vol. 21, no. 13, pp. 1293–1302, 2010.

[48] Kornbluh, R. D., Pelrine, R., Prahlad, H., Wong-Foy, A., McCoy, B., Kim, S., Eckerle, J., and Low, T., *From Boots to Buoys: Promises and Challenges of Dielectric Elastomer Energy Harvesting*, pp. 67–93. Springer, 2012.

[49] Krylov, N. M. and Bogoliubov, N. N., *Introduction to non-linear mechanics*. Princeton University Press, 1943.

[50] Kumar, P., Narayanan, S., Adhikari, S., and Friswell, M. I., "Fokker–planck equation analysis of randomly excited nonlinear energy harvester," *Journal of Sound and Vibration*, vol. 333, no. 7, pp. 2040–2053, 2014.

[51] Kundert, K. S. and Sangiovannivincentelli, A., "Simulation of nonlinear circuits in the frequency-domain," *IEEE Transactions on Computer-Aided Design of Integrated Circuits and Systems*, vol. 5, no. 4, pp. 521–535, 1986. E0818 Times Cited:172 Cited References Count:27.

[52] Le, C. P., Halvorsen, E., Sorasen, O., and Yeatman, E. M., "Microscale electrostatic energy harvester using internal impacts," *Journal of Intelligent Material Systems and Structures*, vol. 23, no. 13, pp. 1409–1421, 2012.

[53] Leadenham, S. and Erturk, A., "M-shaped asymmetric nonlinear oscillator for broadband vibration energy harvesting: Harmonic balance analysis and experimental validation," *Journal of Sound and Vibration*, vol. 333, no. 23, pp. 6209–6223, 2014. Ao9ks Times Cited:1 Cited References Count:67.

[54] Leadenham, S. and Erturk, A., "Unified nonlinear electroelastic dynamics of a bimorph piezoelectric cantilever for energy harvesting, sensing, and actuation," *Nonlinear Dynamics*, vol. 79, no. 3, pp. 1727–1743, 2015.

[55] Lesieutre, G. A., Ottman, G. K., and Hofmann, H. F., "Damping as a result of piezoelectric energy harvesting," *Journal of Sound and Vibration*, vol. 269, no. 3-5, pp. 991–1001, 2004. 764EU Times Cited:163 Cited References Count:11.

[56] Litak, G., Borowiec, M., Friswell, M. I., and Adhikari, S., "Energy harvesting in a magnetopiezoelastic system driven by random excitations with uniform and gaussian distributions," *Journal of Theoretical and Applied Mechanics*, vol. 49, no. 3, pp. 757–764, 2011.

[57] Litak, G., Friswell, M. I., and Adhikari, S., "Magnetopiezoelastic energy harvesting driven by random excitations," *Applied Physics Letters*, vol. 96, no. 21, p. 214103, 2010.

[58] Litak, G., Friswell, M. I., Kwuimy, C. A. K., Adhikari, S., and Borowiec, M., "Energy harvesting by two magnetopiezoelastic oscillators with mistuning," *Theoretical and Applied Mechanics Letters*, vol. 2, no. 4, p. 043009, 2012.

[59] Mahmoodi, S. N., Jalili, N., and Daqaq, M. F., "Modeling, nonlinear dynamics, and identification of a piezoelectrically actuated microcantilever sensor," *Ieee-Asme Transactions on Mechatronics*, vol. 13, no. 1, pp. 58–65, 2008.

[60] Mann, B. P. and Owens, B. A., "Investigations of a nonlinear energy harvester with a bistable potential well," *Journal of Sound and Vibration*, vol. 329, no. 9, pp. 1215–1226, 2010.

[61] Mann, B. P. and Sims, N. D., "Energy harvesting from the nonlinear oscillations of magnetic levitation," *Journal of Sound and Vibration*, vol. 319, no. 1-2, pp. 515–530, 2009.

[62] Masana, R. and Daqaq, M. F., "Relative performance of a vibratory energy harvester in mono- and bi-stable potentials," *Journal of Sound and Vibration*, vol. 330, no. 24, pp. 6036–6052, 2011.

[63] Maugin, G. A., *Nonlinear electromechanical effects and applications*, vol. 1. World Scientific, 1985.

[64] McInnes, C. R., Gorman, D. G., and Cartmell, M. P., "Enhanced vibrational energy harvesting using nonlinear stochastic resonance," *Journal of Sound and Vibration*, vol. 318, no. 4-5, pp. 655–662, 2008.

[65] Meirovitch, L., *Fundamentals of vibrations*. Waveland Press, 2010.

[66] Mitcheson, P. D., Miao, P., Stark, B. H., Yeatman, E. M., Holmes, A. S., and Green, T. C., "Mems electrostatic micropower generator for low frequency operation," *Sensors and Actuators a-Physical*, vol. 115, no. 2-3, pp. 523–529, 2004.

[67] Moon, F. C. and Holmes, P. J., "A magnetoelastic strange attractor," *Journal of Sound and Vibration*, vol. 65, no. 2, pp. 275–296, 1979.

[68] Morison, J. R., Obrien, M. P., Johnson, J. W., and Schaaf, S. A., "The force exerted by surface waves on piles," *Transactions of the American Institute of Mining and Metallurgical Engineers*, vol. 189, no. 05, pp. 149–154, 1950. Xr344 Times Cited:189 Cited References Count:0.

[69] Moss, S. D., Payne, O. R., Hart, G. A., and Ung, C., "Scaling and power density metrics of electromagnetic vibration energy harvesting devices," *Smart Materials and Structures*, vol. 24, no. 2, p. 023001, 2015. Az8ww Times Cited:0 Cited References Count:80.

[70] Nayfeh, A. H. and Balachandran, B., *Applied nonlinear dynamics: analytical, computational and experimental methods*. John Wiley & Sons, 2008.

[71] Nayfeh, A. H. and Mook, D. T., *Nonlinear oscillations*. John Wiley & Sons, 2008.

[72] Nayfeh, A. H., *Perturbation methods*. John Wiley & Sons, 2008.

[73] Nguyen, D. S., Halvorsen, E., Jensen, G. U., and Vogl, A., "Fabrication and characterization of a wideband mems energy harvester utilizing nonlinear springs," *Journal of Micromechanics and Microengineering*, vol. 20, no. 12, 2010.

[74] Nguyen, S. D., Halvorsen, E., and Paprotny, I., "Bistable springs for wideband microelectromechanical energy harvesters," *Applied Physics Letters*, vol. 102, no. 2, 2013.

[75] Ottman, G. K., Hofmann, H. F., Bhatt, A. C., and Lesieutre, G. A., "Adaptive piezoelectric energy harvesting circuit for wireless remote power supply," *Ieee Transactions on Power Electronics*, vol. 17, no. 5, pp. 669–676, 2002.

[76] Pellegrini, S. P., Tolou, N., Schenk, M., and Herder, J. L., "Bistable vibration energy harvesters: A review," *Journal of Intelligent Material Systems and Structures*, vol. 24, no. 11, pp. 1303–1312, 2013.

[77] Priya, S., "Advances in energy harvesting using low profile piezoelectric transducers," *Journal of Electroceramics*, vol. 19, no. 1, pp. 167–184, 2007.

[78] Priya, S., Viehland, D., Carazo, A. V., Ryu, J., and Uchino, K., "High-power resonant measurements of piezoelectric materials: Importance of elastic nonlinearities," *Journal of Applied Physics*, vol. 90, no. 3, pp. 1469–1479, 2001.

[79] Ramlan, R., Brennan, M. J., Mace, B. R., and Kovacic, I., "Potential benefits of a non-linear stiffness in an energy harvesting device," *Nonlinear Dynamics*, vol. 59, no. 4, pp. 545–558, 2010.

[80] Renno, J. M., Daqaq, M. F., and Inman, D. J., "On the optimal energy harvesting from a vibration source," *Journal of Sound and Vibration*, vol. 320, no. 1-2, pp. 386–405, 2009.

[81] Roundy, S. and Wright, P. K., "A piezoelectric vibration based generator for wireless electronics," *Smart Materials & Structures*, vol. 13, no. 5, pp. 1131–1142, 2004.

[82] Roundy, S., Wright, P. K., and Rabaey, J., "A study of low level vibrations as a power source for wireless sensor nodes," *Computer Communications*, vol. 26, no. 11, pp. 1131–1144, 2003.

[83] Roundy, S., Wright, P. K., and Rabaey, J. M., *Energy scavenging for wireless sensor networks*. Springer, 2003.

[84] Rupp, C. J., Dunn, M. L., and Maute, K., "Analysis of piezoelectric energy harvesting systems with non-linear circuits using the harmonic balance method," *Journal of Intelligent Material Systems and Structures*, vol. 21, no. 14, pp. 1383–1396, 2010. 690LF Times Cited:7 Cited References Count:23.

[85] Shu, Y. C. and Lien, I. C., "Analysis of power output for piezoelectric energy harvesting systems," *Smart Materials & Structures*, vol. 15, no. 6, pp. 1499–1512, 2006.

[86] Smith, R. C., Seelecke, S., Dapino, M., and Ounaies, Z., "A unified framework for modeling hysteresis in ferroic materials," *Journal of the Mechanics and Physics of Solids*, vol. 54, no. 1, pp. 46–85, 2006.

[87] Sneller, A. J., Cette, P., and Mann, B. P., "Experimental investigation of a post-buckled piezoelectric beam with an attached central mass used to harvest energy," *Proceedings of the Institution of Mechanical Engineers Part I-Journal of Systems and Control Engineering*, vol. 225, no. I4, pp. 497–509, 2011.

[88] Sodano, H. A., Inman, D. J., and Park, G., "A review of power harvesting from vibration using piezoelectric materials," *Shock and Vibration Digest*, vol. 36, no. 3, pp. 197–206, 2004.

[89] Stanton, S. C., Erturk, A., Mann, B. P., Dowell, E. H., and Inman, D. J., "Nonlinear nonconservative behavior and modeling of piezoelectric energy harvesters including proof mass effects," *Journal of Intelligent Material Systems and Structures*, vol. 23, no. 2, pp. 183–199, 2012.

[90] Stanton, S. C., Erturk, A., Mann, B. P., and Inman, D. J., "Nonlinear piezoelectricity in electroelastic energy harvesters: Modeling and experimental identification," *Journal of Applied Physics*, vol. 108, no. 7, p. 074903, 2010.

[91] Stanton, S. C., Erturk, A., Mann, B. P., and Inman, D. J., "Resonant manifestation of intrinsic nonlinearity within electroelastic micropower generators," *Applied Physics Letters*, vol. 97, no. 25, 2010.

[92] Stanton, S. C., McGehee, C. C., and Mann, B. P., "Reversible hysteresis for broadband magnetopiezoelastic energy harvesting," *Applied Physics Letters*, vol. 95, no. 17, pp. 174103–174103–3, 2009.

[93] Stanton, S. C., McGehee, C. C., and Mann, B. P., "Nonlinear dynamics for broadband energy harvesting: Investigation of a bistable piezoelectric inertial generator," *Physica D-Nonlinear Phenomena*, vol. 239, no. 10, pp. 640–653, 2010.

[94] Stanton, S. C., Owens, B. A. M., and Mann, B. P., "Harmonic balance analysis of the bistable piezoelectric inertial generator," *Journal of Sound and Vibration*, vol. 331, no. 15, pp. 3617–3627, 2012.

[95] Stephen, N. G., "On energy harvesting from ambient vibration," *Journal of Sound and Vibration*, vol. 293, no. 1-2, pp. 409–425, 2006.

[96] Tang, D. M., Zhao, M. H., and Dowell, E. H., "Inextensible beam and plate theory: Computational analysis and comparison with experiment," *Journal of Applied Mechanics-Transactions of the Asme*, vol. 81, no. 6, p. 061009, 2014. Ak1uf Times Cited:1 Cited References Count:10.

[97] Tang, L. H., Yang, Y. W., and Soh, C. K., "Toward broadband vibration-based energy harvesting," *Journal of Intelligent Material Systems and Structures*, vol. 21, no. 18, pp. 1867–1897, 2010.

[98] Thomson, W., *Theory of vibration with applications*. CRC Press, 1996.

[99] Tiersten, H. F., "Electroelastic equations for electroded thin plates subject to large driving voltages," *Journal of Applied Physics*, vol. 74, no. 5, pp. 3389–3393, 1993.

[100] Tvedt, L. G. W., Nguyen, D. S., and Halvorsen, E., "Nonlinear behavior of an electrostatic energy harvester under wide- and narrowband excitation," *Journal of Microelectromechanical Systems*, vol. 19, no. 2, pp. 305–316, 2010.

[101] Twiefel, J. and Westermann, H., "Survey on broadband techniques for vibration energy harvesting," *Journal of Intelligent Material Systems and Structures*, vol. 24, no. 11, pp. 1291–1302, 2013.

[102] Usher, T. and Sim, A., "Nonlinear dynamics of piezoelectric high displacement actuators in cantilever mode," *Journal of Applied Physics*, vol. 98, no. 6, p. 064102, 2005.

[103] Virgin, L. N., *Vibration of axially loaded structures*, vol. 393. Cambridge University Press New York, 2007.

[104] Von Wagner, U. and Hagedorn, P., "Piezo-beam systems subjected to weak electric field: Experiments and modelling of non-linearities," *Journal of Sound and Vibration*, vol. 256, no. 5, pp. 861–872, 2002.

[105] Wang, L. and Yuan, F. G., "Vibration energy harvesting by magnetostrictive material," *Smart Materials and Structures*, vol. 17, no. 4, 2008.

[106] Wang, Q. M., Zhang, Q. M., Xu, B. M., Liu, R. B., and Cross, L. E., "Nonlinear piezoelectric behavior of ceramic bending mode actuators under strong electric fields," *Journal of Applied Physics*, vol. 86, no. 6, pp. 3352–3360, 1999.

[107] Wolf, K. and Gottlieb, O., "Nonlinear dynamics of a cantilever beam actuated by piezoelectric layers in symmetric and assymetric configuration," *Technion-Isreael Institute of Technology, Technical Report ETR-2001-02*, 2001.

[108] Zhao, S. and Erturk, A., "On the stochastic excitation of monostable and bistable electroelastic power generators: Relative advantages and tradeoffs in a physical system," *Applied Physics Letters*, vol. 102, no. 10, p. 103902, 2013.